

A TIME-RESOLVED X-RAY SCATTERING STUDY
OF THE ORDERING KINETICS IN Cu_3Au

By

ROBERT FRANCIS SHANNON, JR.

A DISSERTATION PRESENTED
TO THE GRADUATE SCHOOL OF THE UNIVERSITY OF FLORIDA
IN PARTIAL FULFILLMENT OF THE REQUIREMENTS
FOR THE DEGREE OF DOCTOR OF PHILOSOPHY

UNIVERSITY OF FLORIDA

1990

ACKNOWLEDGMENTS

Stephen E. Nagler's, patience and understanding, as well as guidance, have been instrumental in my progress as a graduate student. Without him this work could not have been done.

I thank Curtis R. Harkless who spent many a late night watching the experiment so that I could get some sleep. He also was very helpful in the tuning and operation of the temperature control system. I could list many ways in which Curt contributed to this work, but most of all I found discussions with him to be of the most use.

Our engineer Ward Ruby, who is overqualified for his position, lent technical expertise that was of course very valuable, but his sense of humor and good nature was probably even more helpful by keeping my spirits up.

Marsha E. Singh spent two years as a post doc in our lab. Although she was working on a different project, she found time to help with the convolution fitting routines, and discussed problems that I encountered.

Thanks go to Gary Venn and Lee Smith for their knowledge with computers, Gary for writing the scan program used to control the diffractometer and Lee for configuring and linking our computer system.

Also, I would like to thank P. H. Holloway and J. K. Truman for their help in preparing the sputtered films, R. M. Nicklow for the bulk sample, as well as P. Flynn and J. Dura for the M.B.E. films.

I thank my family, Bob and Kay my parents, and Kathy and Kevin, my siblings. Their support, both moral and financial, cannot be overlooked. Bob and Kathy, having both received a PhD., Kay presently working on one, and Kevin having received an MD, all understand life as a graduate student. Their advice comes from knowledge and experience and has been helpful.

Finally, I wish to thank the U.S. D.O.E. for their support of this research.

TABLE OF CONTENTS

ACKNOWLEDGMENTS	ii
LIST OF FIGURES	vi
LIST OF TABLES	ix
ABSTRACT	x
CHAPTERS	
1 BACKGROUND	1
Introduction	1
Previous Work	5
2 THE GROWTH OF ORDER	10
3 X-RAY DIFFRACTION BY Cu_3Au	20
Basic X-ray Scattering	20
Diffraction with Cu_3Au and its	
Relation to the Order Parameter	25
Anisotropy in Cu_3Au	29
The Effect of Type 1 Walls on Scattering	34
4 EXPERIMENTS	37
The Bulk Single Crystal	37
Experimental Details	37
Analysis of the Bulk Data	45
Results from the Bulk Data	54
The Sputtered Films and the Effect	
of Stoichiometry	83
Experimental Details	83
Analysis for the Data on the	
Sputtered Films	85
Results from the Sputtered Films	87
The M.B.E. Films	93
Experimental Details	93
Analysis on the M.B.E. Film Data	97
Results from the M.B.E. Films	98
Scaling and System Dimension	107
A Brief Look at the Early Time	119

5	CONCLUSIONS	127
	Current Results	127
	Future Directions	129
APPENDIXES		
	THE EFFECT OF TYPE 1 WALLS ON SCATTERING	130
	FUNCTIONAL DEFINITIONS USED IN FITTING	136
	HOW TO CALIBRATE THE BRAUN PSD	138
	SPECTROMETER ALIGNMENT	140
	DETECTOR DEAD TIME CORRECTION	143
	REFERENCES	144
	BIOGRAPHICAL SKETCH	151

LIST OF FIGURES

<u>Figure</u>	<u>page</u>
1. Schematic of (fcc) structure for ordered Cu_3Au	3
2. Coexistence and classical spinodal curves for a first order transition in a typical binary alloy.	11
3. Ordering and coarsening after a quench;	13
4. Difference in path length for scattering	23
5. Domains of different phase separated by a type-1 wall	30
6. Domains of different phase separated by a type-2 wall	31
7. Domains of 3 phases separated by curved walls	33
8. Anisotropic scattering disks profiles	35
9. First version of the heating element/sample mount	38
10. Lay out of equipment: a) Radial b) Transverse	43
11. Ge [1,1,1] or radial instrumental resolution	47
12. Ge [1,1,1] or transverse instrumental resolution	48
13. Mosaic spread at the [0,1,0]	50
14. Effective radial resolution	52
15. Effective transverse resolution	53
16. Change in line shape after a quench	55
17. Raw data on the [0,1,0] bulk superlattice peak.	68
18. Data shown in fig. 17 scaled by amplitude and width.	69
19. Intensity vs. time.	71
20. Bulk Cu_3Au sample history	73

21.	Scaled intensity vs. scaled time.	74
22.	Amplitude vs. time	75
23.	$\text{Log}_{10}(\text{amplitude})$ vs. $\text{Log}_{10}(\text{time})$ for the bulk	77
24.	Integrated intensity, amplitude, and background	78
25.	$\text{Log}_1(\text{Length})$ vs. $\text{Log}_{10}(\text{time})$. $L \propto 2\pi/\Gamma$	80
26.	Typical $[1,-1,0]$ profiles from sputtered film B	88
27.	$\text{Log}_{10}L$ ($2\pi/\sigma$ in Å) vs. $\text{Log}(\text{time})$	89
28.	L vs. $\text{Log}_{10}(t)$	91
29.	$\text{Log}_{10}(L)$ vs. $\text{Log}_{10}[\text{Log}_{10}(t)]$	92
30.	New heating element/sample mount	96
31.	$L=2\pi/\Gamma$ vs. time for the 4500Å M.B.E. film	100
32.	$\text{Log}_{10}[L]$ vs. $\text{Log}_{10}[\text{time}]$ for the 4500Å M.B.E. film	101
33.	$L=2\pi/\Gamma$ vs. $\text{Log}_{10}[\text{time}]$	102
34.	Size of a domain $L=2\pi/\Gamma$ vs. time for the 710Å	104
35.	$\text{Log}_{10}[L]$ vs. $\text{Log}_{10}[\text{time}]$ for the 710Å M.B.E. film	105
36.	$L=2\pi/\Gamma$ vs. $\text{Log}_{10}[\text{time}]$ for the 710Å M.B.E. film	106
37.	$L=2\pi/\Gamma$ vs. time for the 260Å M.B.E. film	108
38.	$\text{Log}_{10}[L]$ vs. $\text{Log}_{10}[\text{time}]$ for the 260Å M.B.E. film	109
39.	$L=2\pi/\Gamma$ vs. $\text{Log}_{10}[\text{time}]$ for the 260Å M.B.E. film	110
40.	3D scaling plot for 710Å M.B.E. film	112
41.	2D scaling plot for 710Å M.B.E. film	113

42.	3D scaling plot for 260Å M.B.E. film	114
43.	2D scaling plot for 260Å M.B.E. film	115
44.	Raw scans of the 260Å M.B.E. film	116
45.	Weak scaling and incorrect scaling in the 710Å film	117
46.	Weak scaling and incorrect scaling in the 260Å film	118
47.	Early time scans of the [0,1,0] of Cu ₃ Au.	120
48.	Amplitude of the [0,1,0] of bulk Cu ₃ Au vs. time.	121
49.	Log ₁₀ [width] vs. Log ₁₀ [time]	122
50.	Integrated intensity vs. time	124
51.	Radial scan showing the satellites	125

LIST OF TABLES

<u>Table</u>		<u>page</u>
1.	Chi-squared values for selected scans as a function of time after quench on the bulk Cu_3Au sample. Arrangement is by decreasing temperature and direction in reciprocal space	58
2.	Exponents for power law growth from the bulk data	81
3.	Quenches and fitted exponents for the sputtered films	87
4.	M.B.E. film resolution corrections	98

Abstract of Dissertation Presented
to the Graduate School of the University of Florida
in Partial Fulfillment of the Requirements
for the Degree of Doctor of Philosophy

TIME-RESOLVED X-RAY SCATTERING STUDY OF ORDERING KINETICS
IN Cu_3Au

by

Robert Francis Shannon, Jr

August 1990

Chairman: Stephen E. Nagler
Major Department: Physics

Time-resolved x-ray scattering has been used to study ordering kinetics in single crystal bulk Cu_3Au , as well as in sputtered and molecular beam epitaxy grown films. After annealing at high temperatures the sample is rapidly quenched to fixed temperatures below the order-disorder transition temperature. The development of order is monitored in real time using scattering techniques.

The bulk sample clearly showed three regimes: nucleation, ordering, and coarsening. The anisotropic superlattice peaks that reflect the domains structure are investigated in connection with the ordering kinetics. The line shape of the scattering function exhibits a crossover from gaussian to lorentzian-squared as the system goes from the ordering regime to the coarsening regime. Coarsening in Cu_3Au is consistent with curvature driven growth.

Domain coarsening in stoichiometric sputtered films is also consistent with curvature driven growth. However, coarsening in copper rich films proceeds much

more slowly. The results suggest the extra copper affects the ordering kinetics in the same way diffusive impurities would, resulting in a logarithmic like time dependence.

The M.B.E. films show a slowing of the growth at late times. The 4500Å film starts out with curvature driven growth but then continuously slows down as the domains grow. The 710Å film shows an interesting temperature dependence for the growth, in such a way that at temperatures close to the transition, the domain growth almost freezes at late times. The dominate factor is probably strain, all of the trends for slower growth are consistent with greater strain. The dimensionality in the M.B.E. film systems is considered. The scaling in the 4500Å and 710Å films is clearly three dimensional. However, the dimension of the scaling in the 260Å film is unclear.

CHAPTER 1 BACKGROUND

Introduction

The kinetics of phase transitions in systems that exhibit ordering after a quench from above a critical ordering temperature T_c has received much recent interest.^(1–6) One focus of this interest has been on whether universality classes for the kinetics of these systems exist as they do for ordinary static critical phenomena⁽⁶⁾. Conservation laws are known to greatly affect the growth kinetics. However, the effects of symmetry, structure and sharpness of domain walls, order of the degeneracy of the ground state, impurities, and stoichiometry are not well understood. Examples of kinetic behavior can be found in many systems including magnetic materials, copolymers, and alloys.

This dissertation focuses on a careful study of the ordering kinetics in the alloy Cu_3Au . Cu_3Au is a prototypical system with a first order transition, and a nontrivial asymmetry. The elements Cu and Au have considerably different atomic numbers (Z), making x-ray measurements of superlattice peaks easier. Moreover, the equilibrium properties of Cu_3Au are well studied.⁽⁷⁾ Two important properties of Cu_3Au are its four-fold degenerate ground state and the existence of two types of domain walls that separate the four ordered phases. These two differences make Cu_3Au a good choice for furthering our understanding of the non-equilibrium kinetics of first order phase transitions. The non-equilibrium kinetics are less well understood, particularly in the context of the ideas of modern statistical mechanics.

Interesting effects in the non-equilibrium kinetics are introduced by the existence of different domain wall structures and a corresponding anisotropy of the correlations.

Alloys like Cu_3Au exhibit a change in their atomic arrangement as a function of temperature. Such alloys have markedly different equilibrium properties as a function of temperature. However, the present interest is focused on the approach to equilibrium.

The crystalline form of Cu_3Au is face centered cubic (fcc), and below the critical temperature T_c ($T_c \approx 390^\circ\text{C}$) has an equilibrium state where the Au atoms preferentially reside at cube corner sites and the Cu at face center sites, (see figure-1). Above T_c the atoms are randomly distributed, but short range order still persists. The transition from the ordered state to the disordered state is first order, and like so many things in nature the change from order to disorder takes place much faster than the change back to order.

The experiments discussed here are all concerned with the change from disordered to ordered states. In a typical experiment the sample is held at a temperature well above T_c in order to insure that the sample is in a disordered state, from which the temperature is rapidly lowered to a point below T_c and held there for several days. X-ray scattering scans are collected as a function of time. The peak grows with time, becoming narrower and more intense. Moreover, the shape of this x-ray peak is important. Many theories predict this shape and hence, a careful investigation is important to understanding the underlying physics. Surprisingly, there has been little experimental work in this direction. Unfortunately, it is usually difficult to obtain the exact shape due to effects from instrumental resolution, finite size, strain, and mosaic spread.

Experiments have been performed on a bulk single crystal, sputtered films, including one Cu rich film, M.B.E. (molecular beam epitaxy) grown films from 260

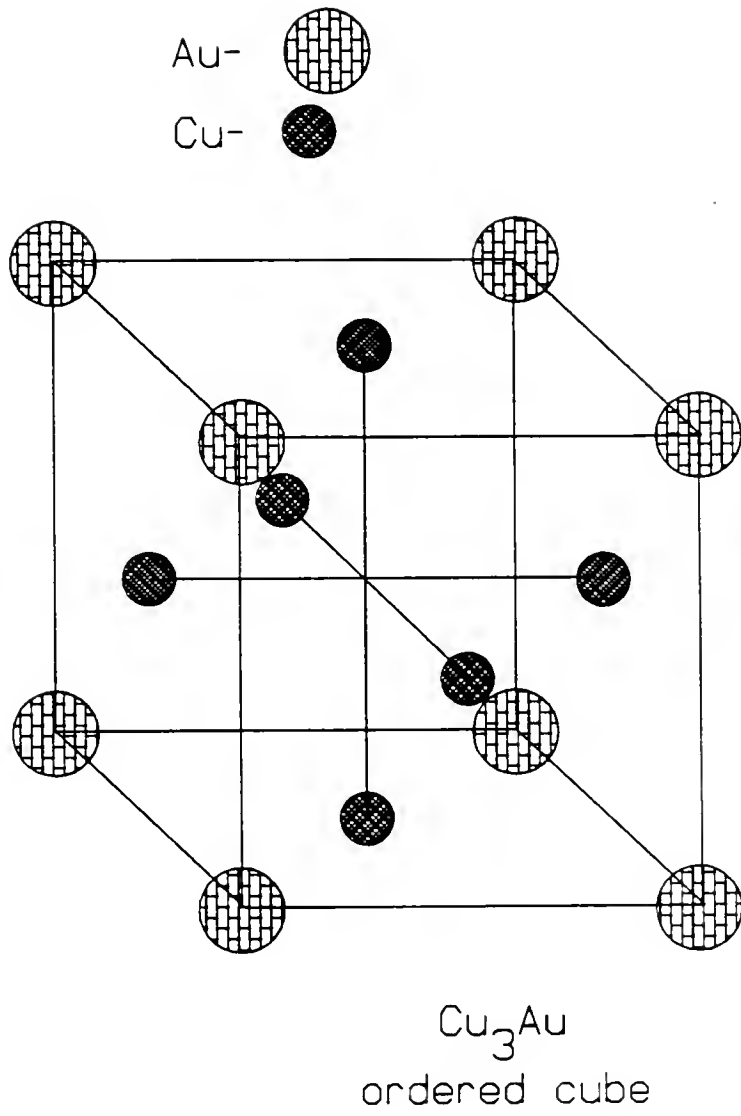


FIG. 1. Schematic of (FCC) structure for ordered Cu_3Au .
 of a domain increases. Larger domains grow at the
 expense of their smaller neighbors.

to 4500 angstroms thick. For each sample the experiment was repeated for a series of temperatures.

From the experiments on the bulk single crystal it is evident that three distinct mechanisms are involved, nucleation, ordering, and coarsening as defined below. Nucleation, as the name suggests, refers to a delay between the quench and the start of the development of long range order. Although in several quenches a nucleation period is observed, the time resolution in these experiments was such that this regime was not well characterized. Others using a different experimental set up and a more powerful x-ray source have probed this aspect of the transition in more detail.⁽⁸⁾ Nucleation refers to a delay between the quench and the start of the development of long range order. Ordering (or growth) is the process by which the disordered state condenses onto the various nucleated droplets of the ordered phase. One of our results is that the ordering process can be characterized by a change in the functional form of the scattering associated with the structure factor. The movement of domain boundaries that separate the different ground states is known as coarsening. This name refers to the fact that as time progresses the average size of the domains grow as the larger domains convert their smaller neighbors to the same phase.

Another sample is an off-stoichiometric sputtered film of Cu_3Au . It is interesting that an off-stoichiometric sample exhibits a different type of growth than its stoichiometric counterpart. Moreover, the off-stoichiometric film is probably in a different class altogether. The extra Cu in the sputtered film acts as a diffusive impurity. However, the stoichiometric sputtered films (all over 7000 angstroms) exhibited curvature driven domain coarsening, where the size of an ordered domain is proportional to the square root of time. The differences in the time dependence usually involve a lowering of the power of the time dependence

from $1/2$ (square root) to a value less than $1/2$. However, the growth in the off-stoichiometric film is also consistent with a logarithmic time dependence.

The last samples are single crystal films grown by molecular beam epitaxy (M.B.E.), which are reviewed in a contexts similar to the off-stoichiometric sputtered film. Both the off-stoichiometric sputtered film and the M.B.E. films display a slower type of time dependence for growth. However, the cause of this change from the bulk behavior at critical composition arises from slightly different causes. Consequently, similarities exist, but so do differences.

Previous Work

The earliest studies of the order disorder transition in Cu_3Au date at least as far back as the early 1900's.⁽⁹⁾ However, the interest then was how the level of order affects bulk properties. The present interest is in the ordering itself and the non-equilibrium properties associated with it. At the time of the earlier work the intensity of available x-ray sources did not permit the in-situ type of measurement made in this work. The early experiments measured only bulk effects like resistance as a function of temperature, time, or order. The only x-ray work that could be done was static measurements. An extensive review of order-disorder transitions in binary alloys prior to the late 1930s can be found in an article by F. C. Nix and W. Shockely.⁽¹⁰⁾ Two experimental papers both from 1936 are worth noting, one by Sykes and Evans⁽¹¹⁾ and the second by Sykes and Jones.⁽¹²⁾ These two works describe the electrical resistance, specific heat, and the crystal structure as related to the order-disorder transition. A later paper by Jones and Sykes⁽¹³⁾ along with their earlier work are the earliest references relating the width of the superlattice peak to domain size.

Bragg and Williams^(14–16) in 1934 and 35 put forth the first equilibrium theory from which the qualitative behavior of bulk properties such as the specific heat, the level of long range order, and resistance could be derived. Formally this theory is analogous to the Weiss theory for ferromagnetism.⁽⁴⁾ This theory worked only below the transition temperature T_c . The Bragg–Williams theory is a static mean field approximation that does not consider fluctuations. The Bragg–Williams theory considers the long range interactions between atoms and therefore, does not explain short–range order and only qualitatively describes the equilibrium properties near T_c . The theory of Bethe⁽¹⁷⁾ considers nearest neighbors. As in the Bragg–Williams case the energy just below T_c is the same as just above T_c . However, in Bethe’s theory additional energy is required to destroy short range order above T_c . This gives rise to an anomaly in the specific heat in agreement with experiment. Due to the complicated nearest neighbor configuration and asymmetry in composition found in A_3B systems like Cu_3Au , many of Bethe’s assumptions regarding the structure do not apply to our case. Fortunately Peierls⁽¹⁸⁾ has applied Bethe’s theory to this case. A more formal approach to the theory of order–disorder kinetics appears in an article from 1956 by G. Vineyard⁽¹⁹⁾. His theory starts with a set of multi particle distribution functions and equations of motion. The simplest approximation for these equations yield the Bragg–Williams result. The Bethe–Peierls approximation can also be derived from this theory if only nearest neighbor interactions are considered.

In the 70s interest in the kinetics of Cu_3Au was renewed by the development of theories that considered the movement of domain walls^(1,20–22) as well as the availability of more intense x–ray sources. Allen and Cahn⁽²⁰⁾ derived the time dependence of the size of an ordered domain. Their theory is often referred to as curvature driven (or controlled) growth because the driving force goes as the

curvature of the wall. The final result is that the size of an ordered domain $L(t)$ is proportional to $t^{1/2}$ (the square root of time). Earlier theories⁽¹⁾ predicted that the velocity of the wall would go as the product of the mean curvature and the interface free energy. Therefore, the earlier versions predicted critical slowing down of the wall as T_c is approached from below. In the Cahn–Allen case the diffusional dissipation of free energy of a domain wall exactly equals the available driving force. Hence, the velocity of a domain wall is not a function of the driving force,⁽²⁰⁾ and the power law that describes the time dependence is not a function of temperature. The temperature dependence is only in a proportionality term that precedes the power law time dependence. This renewed interest is actually part of a growing interest in universality classes and non–equilibrium phenomena which occur in such transitions.

The kinetics of transitions have been of great interest in the past decade. Theoretical,^(1,2,23–39) experimental,^(40–57) and computer simulation^(3,39,58–76) studies on first order phase transitions abound. A variety of systems,⁽³⁰⁾ binary alloys, binary fluids, magnetic materials, block copolymers, glasses, ferroelectric crystals, and others can be used to study this phenomenon. The problem is often discussed in terms of an Ising model,⁽⁷⁸⁾ partly because the order parameter is often simply the magnetization, an easily measured quantity, and partly because Ising like systems are easily classified. Ferromagnets with spin exchange (Kawasaki)⁽³⁾ dynamics are systems with a conserved order parameter (COP), ferromagnets with spin flip (Glauber)⁽⁷⁹⁾ dynamics have a non–conserved order parameter (NCOP), and antiferromagnets with spin exchange dynamics⁽²⁸⁾ have a NCOP (sub lattice magnetization) even though the net magnetization is conserved. The reason being easily classified is so important is that the nature of universality classes⁽³⁰⁾ for growth is not fully understood.

Binary alloys are also useful systems for kinetic studies for similar reasons. One obvious division in classes is whether the order parameter is conserved or non-conserved. A recent computer simulation⁽⁶⁰⁾ on a three-dimensional binary alloy model (of the AB type) with a NCOP shows qualitatively different ordering kinetics than the equivalent spinodal decomposition found in binary alloys with a COP. This simulation possesses a characteristic length that increases as $t^{1/2}$, and a corresponding scaling of the structure factor of L^d , where d is the dimension.

Phase separation is an example of a process with a COP that has been extensively studied experimentally^(10,29,47,50). Phase separation exhibits diffusion controlled growth⁽³¹⁾ where $L(t)$ is proportional to $t^{1/3}$ as compared to the NCOP process of curvature controlled growth^(18,19) where $L(t)$ is proportional to $t^{1/2}$. There are also systems that exhibit interface controlled growth⁽⁴⁾ where $L(t)$ is proportional to time. Hence, the power of the time dependence seems to be an important difference between classes⁽²⁹⁾. Another class may be found in systems with impurities⁽⁸⁰⁻⁸⁴⁾ where $L(t)$ is proportional to $\ln(t)^m$. It has been suggested this class can be further divided by the value of the power m ⁽³⁰⁾, possibly indicating whether the impurities are quenched⁽⁸⁰⁻⁸³⁾ or diffusive^(84,85). This type of growth might also be found for critical quenches (close to T_c) involving spinodal decomposition⁽³⁸⁾.

One purpose of this work is to distinguish different universality classes, specifically the effect of dimensionality, composition, the order of the ground state degeneracy, and the nature of the scaling form for the structure factor^(1,2,23-29,39). There is evidence⁽⁸⁶⁾ that the mechanism of domain growth will change for thin films. Also, there was some question as to whether the order of the degeneracy lowers the power of the time dependence^(56,73,74,77,87-89). Another reason to look at Cu_3Au is that it has two types of domain walls^(21,90,91).

The first of these walls conserves the nearest neighbor configuration and due to the energies involved⁽⁸⁹⁾ is easily formed compared to the second. A comparison of the growth of these two very different walls should provide further insight into the study of order disorder kinetics.⁽⁹²⁾ Moreover, less work has been done on systems involving a NCOP^(7,43,93,94) than COP. After a thermal quench both types of systems exhibit three distinct regimes;^(8,94,95) nucleation, ordering, and coarsening. The functional form of the structure factor can be derived from most applicable theories,^(8,35,39,94,96) however, instrumental resolution, finite size, and strain often have sizable contributions to the shape of the scattering, making it difficult to discern the exact shape of the structure factor experimentally. Determining this shape is another purpose of this work.

The rest of this dissertation is arranged as follows: Chapter 2 discusses the theories of domain coarsening and nonequilibrium scaling. The first part of chapter 3 is on basic x-ray diffraction and how the level of order is related to the diffraction pattern. A description of the different types of domain walls in Cu_3Au can be found at the end of chapter 3. The experimental analysis and results are discussed in chapter 4. Conclusions are presented in chapter 5.

CHAPTER 2 THE GROWTH OF ORDER

Cu_3Au is a prototypical system for order–disorder transitions⁽⁹⁰⁾. The transition is driven by minimizing the free energy

$$F=U-TS. \quad (2.1)$$

At low temperatures the free energy is dominated by the internal energy, U , causing the minimum in free energy to correspond to the ordered state. However, at high temperature the minimum for the free energy corresponds to a disordered state because it is dominated by the entropy term, $(-TS)$. The critical temperature is a function of the concentration of the different atoms. Figure 2 is a generic phase diagram for alloy systems with order disorder transitions. Below the solid coexistence curve the equilibrium state corresponds to order and above to disorder. The dashed curve in figure 2 represents the classical spinodal curve separating regions of metastability and instability of the disordered state after a thermal quench to below T_c . For phase separation these two curves meet at the critical composition. However, for the process of superlattice formation,⁽⁸⁾ this is not the case, producing an extended nucleation period even for the stoichiometric composition.

For instantaneous quenches to temperatures just below T_c the short–range order fluctuations associated with temperatures above T_c are metastable. This metastable state then decays during a finite incubation time towards a new equilibrium value⁽⁸⁾. During the incubation time the fluctuations are such that the

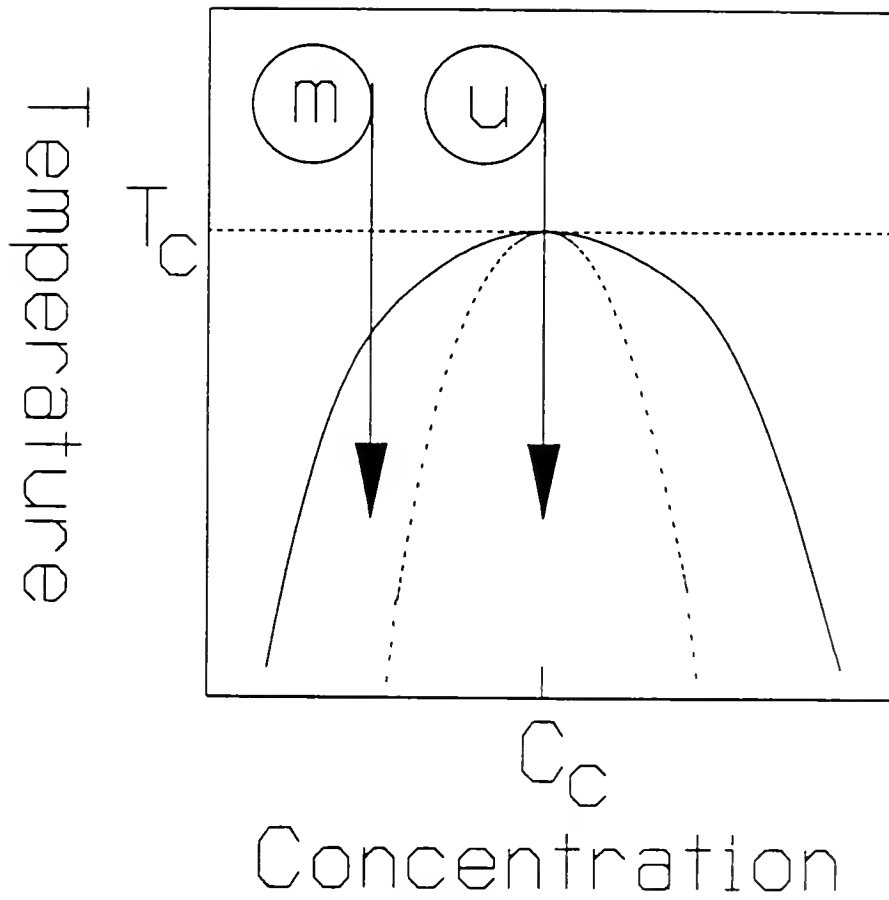


FIG. 2. Coexistence curve (solid) and classical spinodal curve (dashed) for a first order transition in a typical binary alloy. Points M and U label regions as metastable or unstable.

critical size for the stability of an ordered droplet is not realized. The nucleation stage starts when the fluctuations have relaxed sufficiently to allow a stable ordered droplet to form. As quenches become deeper the fluctuations associated with the disordered state become unstable and nucleated ordering changes to continuous (or spinodal) ordering. There is some indication that this change occurs well below the classical spinodal temperature.⁽⁸⁾ In fact there is no abrupt change as nucleated ordering changes to spinodal. After nucleation droplets of the ordered phase grow in a matrix of the disordered phase (see fig 3a). The individual droplets may be in any of the p allowed ground states. Eventually the domain boundaries meet, and the system is composed of domains in different ground states separated by domain walls (see fig. 3b,c). The coarsening process then begins as the larger domains grow at the expense of their smaller neighbors.

In the coarsening regime the system can be characterized by $L(t)$, the average size of an ordered domain at time t . During coarsening it is expected that the system will be self-similar under a rescaling of both space and time. The growth of the domains is characterized by the time dependence of $L(t)$. If all the excess energy is at the domain walls the velocity of the wall is proportional to its curvature, as discussed below. This leads to an equation of motion;

$$\frac{dr}{dt} \propto K \equiv \frac{1}{r} \quad (2.2)$$

Separating variables gives

$$r \, dr \propto dt \quad (2.3)$$

Integration shows

$$\frac{1}{2}r^2 \propto t \quad (2.4)$$

which implies

$$L(t) \propto t^{1/2} \quad (2.5)$$

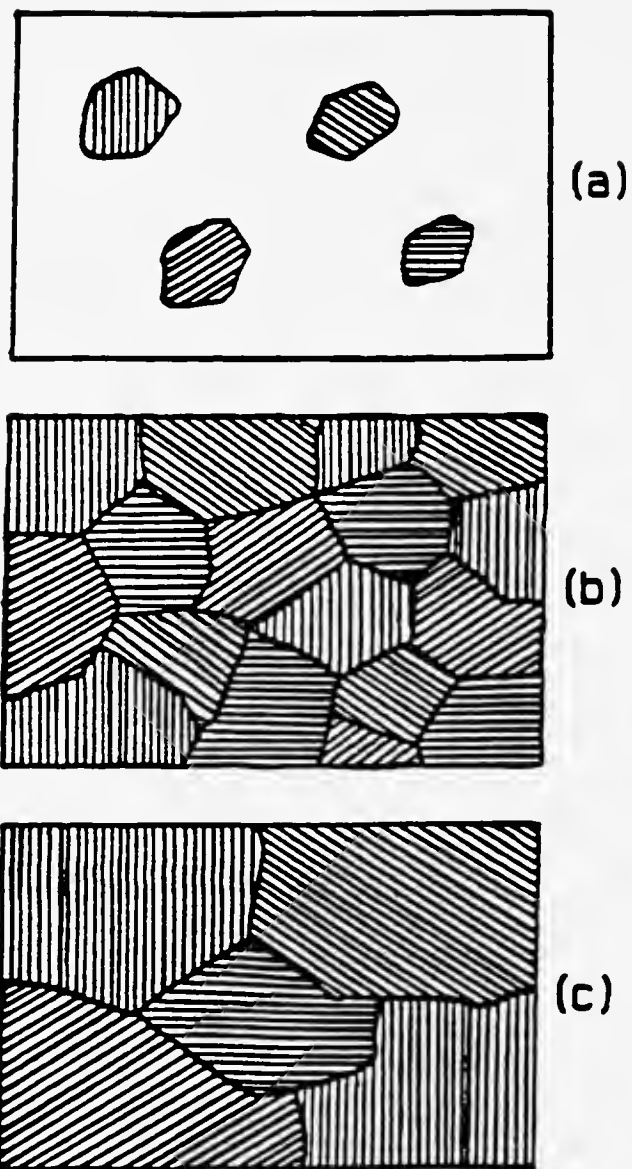


FIG. 3 Ordering and coarsening after a quench.

a) Ordering shortly after the on set of critical nucleation.

b) Early stages of domain coarsening. c) Late stages of domain coarsening.

This is Cahn–Allen (C–A) curvature driven growth. For a NCOP system with $p=2$ and no random impurities the C–A result has been found to be correct.^(20,22)

Another growth mechanism is that of Lifshitz and Slyozov, where the rate of change in the volume of a domain is constant. This type of growth is expected in systems with a COP that exhibit phase separation.

$$\frac{dV}{dt} = \text{constant} \quad (2.6)$$

To convert 2.6 to a velocity is a simple matter. The volume is proportional to r^3 so,

$$dV \propto r^2 dr. \quad (2.7)$$

Substitution into 2.6 shows,

$$\frac{dr}{dt} \propto 1/r^2. \quad (2.8)$$

The velocity of a domain wall is proportional to the inverse of the area of the wall.

Integration as done above leads to,

$$L(t) \propto t^{1/3} \quad (2.9)$$

a slower power law.

An even slower power law of $t^{1/4}$ has been recently proposed.⁽⁹⁷⁾ When this new class was first proposed it was explained by the failure of the assumptions made in the C–A theory and hence, rightfully came under attack. It is only recently that the correct reasons for this classes existence have been revealed. The $t^{1/4}$ class is associated with the case of zero curvature in the Cahn–Allen theory. This new class exhibits competition between sharp and broad domain walls. It has also been found that this class displays a cross over from $t^{1/4}$ to $t^{1/2}$ as the temperature is increased.

A fourth type of time dependence may be found in systems with energy barriers to the growth which depend on the characteristic length L ,⁽³⁰⁾

$$E(L) = L^{1/m}/A \quad (2.10)$$

where A is weakly temperature dependent. If the time necessary to over come such

a barrier is of the form,

$$t = \tau \exp(E(L)/T) \quad (2.11)$$

then inverting, and substituting for $E(L)$ gives,

$$L(t) = AT [\ln(t/\tau)]^m \quad (2.12)$$

a logarithmic dependence on time, where m is a constant, that depends on the type of barrier, and τ is a rate constant.

Obtaining the time dependence from the velocity of a domain wall (anti-phase domain boundary) as done above is simple. It is considerably more difficult to show that the velocity either goes as the curvature, or as the inverse of the surface area. The velocity in general is proportional to the thermodynamic driving force⁽¹⁻⁴⁾ and associated constant of proportionality is called the mobility. One way to consider thermodynamic nonequilibrium is through a mean field approach. Mean field theories to nonequilibrium dynamics of metastable states are an alternative to cluster dynamic theories, and are of practical importance in determining the thermodynamic driving forces involved in domain coarsening.⁽¹⁻⁴⁾ Attention is focused on a small set of semi-macroscopic variables that define an order parameter like the ones discussed at the end of chapter three. These variables are considered to have slow dynamic evolution as compared to the microscopic degrees of freedom, that are averaged, or enter only as random forces. The slowness is important because the derivatives with respect to time are frequently approximated as zero.

The typical attack is to use a Ginzburg-Landau Hamiltonian⁽¹⁾ where the free energy density has a double well structure below some critical temperature. The double well corresponds to the two different phases ordered or disordered. In the COP process of phase separation the order parameter is the local concentration of one species of atoms, where for the NCOP process of superlattice formation the

order parameter is the occupation of a species of atoms on a superlattice. This difference results in very different behavior. For the COP process the structure factor or scattering not only grows in amplitude as the width decreases, but the position moves from high to low q , as phase separation increases. Moreover, because the order parameter is conserved the integrated intensity must be a constant. For the NCOP case intensity at a superlattice peak is a function of the order parameter as shown earlier.

The Cahn–Allen result starts by assuming the free energy per unit volume of a homogeneous phase f_0 is a function of the order parameter Ψ . The important quantity is Δf_0 , the difference between a state of arbitrary order and an ordered state. The equation of motion is then,

$$\frac{\partial \Psi}{\partial t} = -a \frac{\partial \Delta f}{\partial \Psi} + M \nabla^2 \Psi \quad (2.13)$$

where a is a positive kinetic coefficient and $M \equiv 2a\kappa$ is a diffusion coefficient (m^2/s). Rewriting 2.13 to correspond to a direction \hat{g} normal to a surface of constant Ψ gives,

$$\frac{\partial \Psi}{\partial t} = -a \frac{\partial \Delta f}{\partial \Psi} - M \left[\frac{\partial^2 \Psi}{\partial g^2} - (K_1 + K_2) \Psi \frac{\partial \Psi}{\partial g} \right] \quad (2.14)$$

where $(K_1 + K_2)$ is the mean curvature which is equal to the negative of the divergence of a unit vector normal to the surface. In the original paper by Cahn and Allen \hat{g} was defined such that for a spherical domain \hat{g} was directed towards the interior. Although many reverse this convention it will be followed here. Now consider a gently curved domain wall. A domain wall is a surface of constant Ψ . The velocity of the wall is just $\partial g / \partial t$ of a constant Ψ surface.

$$V = \left[\frac{\partial g}{\partial t} \right]_{\Psi} = - \left[\frac{\partial \Psi}{\partial t} \right]_g / \left[\frac{\partial \Psi}{\partial g} \right]_t \quad (2.15)$$

but from 2.13 for this surface,

$$\left[\frac{\partial \Psi}{\partial t} \right]_g = -M(K_1 + K_2) \left[\frac{\partial \Psi}{\partial g} \right]_t \quad (2.16)$$

therefore, from 2.14 and 2.15,

$$V = M(K_1 + K_2). \quad (2.17)$$

As previously discussed this result leads to the time dependence given in equation 2.5. Also this result was derived in the contexts of a second order transition which is being applied to the late time development of a first order transition.

The degree of order and microscopic structure of a system can be characterized by the order parameter correlation function. The fourier transform of the correlation function, $S(Q)$, is called the structure factor. As discussed in chapter 3, $S(Q)$ is directly measured in x-ray experiments. In a nonequilibrium situation, such as that following a quench into a metastable or unstable state, the structure factor may be generalized and written as $S(Q,t)$, where t is the time after a quench.

Self similarity of the ordering system under a rescaling of space and time for a COP process is exhibited by the scaling form of the structure factor.

$$S(Q,t) = [q_{\max}(t)]^{-d} \tilde{S}_e[q/q_{\max}(t)] \quad (2.18)$$

For a NCOP system,

$$S(Q,t) = [\sigma(t)]^{-d} \tilde{S}_e[(q)/\sigma(t)] \quad (2.19)$$

where $q=Q-G$, G is the ordering wave vector, d is the spatial dimensionality, and $\hat{e}=q/q$. In the COP case q_{\max} is a function of time and in the NCOP case it is a constant. Although the two types of scaling are different they can be made to look similar. In the COP case the scattering arises from the domains forming an imperfect lattice. Hence, the position $[q_{\max}(t) \propto 1/L(t)]$ is a function of the distance between domains, which on average is the size of the domains. In contrast the length scale in the NOCP case is inversely proportional to the peak width, $\sigma(t)$. Substitution of $L(t)$ into 2.18 and 2.19 gives the identical result.

$$S(Q,t) = [L(t)]^d \tilde{S}_e[qL(t)] \quad (2.20)$$

Scattering is defined by the structure factor, therefore, this type of scaling implies that the functional form of the scattering remains constant. If scaling is valid, only the amplitude and width change for the NCOP system. Equations 2.18–2.20 also describes how the dimensionality of a system can be detected. In general the scaling function \bar{S} is anisotropic, reflecting the structure of both the domains and their walls.⁽²⁷⁾

A recent proposal⁽³⁰⁾ divides growth kinetics into four classes characterized by different low temperature behaviors. For class 1 systems the temperature is not important, such as a simple Ising ferromagnet with Glauber dynamics. Class 1 systems obey power law domain growth at all temperatures. Cu_3Au probably belongs to class two. Class two differs from class one only in that members have local defects that cause freezing of the domain growth at absolute zero. Such local defects are expected to have activation energies that are independent of domain size L . Classes three and four, on the other hand, have defects with $L(t)$ dependent activation energies, leading to logarithmic growth which is discussed in connection to equation 2.12. Type Three and four systems are differentiated by the power m of the logarithmic growth. Class three has $m=1$, and is likely to contain the random field Ising model. Class four has $m \neq 1$, and may include dilute ferromagnets and spin glasses.

The integrated intensity is independent of the existence of anti-phase domains.⁽⁹⁰⁾ Experimentally, however, if the domains are very small, it is possible to lose some intensity in the tails of the reflection. The width of a superlattice peak is of course greatly affected by the existence of domains. Broadening from the finite size of domains, in the Cu_3Au case, has a dependence on (h,k,l) ⁽⁹⁰⁾ as will be shown in the next chapter. An effective size can be defined but it is purely formal since there are corrections.

$$L_{\text{eff}} = 2\pi/\sigma \tag{2.21}$$

where σ is the width in units of inverse distance.

CHAPTER 3 X-RAY DIFFRACTION BY Cu_3Au

Basic X-ray Scattering

The diffraction of x-rays depends on the crystal structure and the wavelength. X-rays are scattered by the electric field created by the electrons. Hence, the diffraction of x-ray photons contains information concerning electron density.

The position of the diffraction peak can be easily derived by considering the difference in path length of two beams reflected off two parallel crystalline planes a distance d apart.⁽⁹⁸⁾ If the difference in path length is a multiple of the wavelength of the radiation used, then constructive interference forms a peak. This logic leads to Bragg's Law,

$$2d\sin(\theta)=n\lambda \quad (3.1)$$

where θ is measured from the plane, and n is an integer. Bragg's Law is valid, if $\lambda \leq 2d$, which is why x-rays are used to probe crystals. Bragg's Law considers the periodicity of the lattice. However, it does not consider the structure or material that make up the lattice. Consequently, Bragg's Law does not contain any information about the intensity of the diffraction.

Before considering the electron density, which truly defines the diffraction, it is convenient to define a reciprocal lattice. Given three primitive lattice vectors $(\mathbf{a}_1, \mathbf{a}_2, \mathbf{a}_3)$, the primitive reciprocal lattice vectors are defined as;

$$b_1 = 2\pi \cdot \frac{a_2 \times a_3}{a_1 \cdot a_2 \times a_3}; \quad b_2 = 2\pi \cdot \frac{a_3 \times a_1}{a_1 \cdot a_2 \times a_3}; \quad b_3 = 2\pi \cdot \frac{a_1 \times a_2}{a_1 \cdot a_2 \times a_3}. \quad (3.2)$$

The primitive reciprocal lattice vectors are constructed so that each is orthogonal to two of the three crystal primitive lattice vectors. Thus,

$$b_i \cdot a_j = 2\pi \delta_{ij} \quad (3.3)$$

where δ_{ij} is the Kronecker delta function. The factor of 2π is omitted by crystallographers but are used for convenience in physics. The reciprocal lattice is the set of points defined by the reciprocal lattice vector,

$$G = v_1 b_1 + v_2 b_2 + v_3 b_3 \quad (3.4)$$

where v_i is an integer. All crystal structures have two interdependent lattices, the crystal lattice and the reciprocal lattice. For example, the crystal lattice for Cu_3Au is face centered cubic (fcc), it is a simple mathematical exercise to show that the reciprocal lattice associated with an fcc crystal lattice is a body centered cubic (bcc) lattice.^(90,98)

The properties of a crystal are invariant under a transformation between equivalent lattice sites. The electron number density $n(\mathbf{r})$ must, therefore, be periodic in \mathbf{r} with periods $\mathbf{a}_1, \mathbf{a}_2, \mathbf{a}_3$ in the directions of the crystal axes.⁽⁹⁸⁾ This is expressed mathematically as,

$$n(\mathbf{r} + \mathbf{T}) = n(\mathbf{r}) \quad (3.5)$$

where \mathbf{T} is the crystal lattice vector,

$$\mathbf{T} = n_1 \mathbf{a}_1 + n_2 \mathbf{a}_2 + n_3 \mathbf{a}_3 \quad (3.6)$$

where n_i is an integer.

Applying fourier analysis to the periodic function $n(\mathbf{r})$ is equivalent to finding a set of vectors \mathbf{J} such that $n(\mathbf{r})$ is invariant under translations of the crystal lattice vector;

$$n(\mathbf{r}) = \sum_{\mathbf{J}} n_{\mathbf{J}} \cdot \exp(i\mathbf{J} \cdot \mathbf{r}) = n(\mathbf{r} + \mathbf{T}). \quad (3.7)$$

By Bloch's theorem G exactly satisfies the condition expressed in 3.7 for \mathbf{J} .

The fourier coefficients $n_{\mathbf{G}}$ determine the intensity of the scattered radiation, and that the Bragg condition is equivalent to the difference between the incident and scattered wave vectors being \mathbf{G} . As seen in figure 4 the difference in phase factor between the incident (\mathbf{k}) and scattered (\mathbf{k}') wave vectors is $\exp[i(\mathbf{k}-\mathbf{k}')\cdot\mathbf{r}]$. The scattering amplitude is an integral over space of the electron concentration times this phase factor;

$$F = \int dV n(\mathbf{r}) \exp[i(\mathbf{k}-\mathbf{k}')\cdot\mathbf{r}]. \quad (3.8)$$

Repeatedly using the invariance of $n(\mathbf{r})$ by translations \mathbf{T} , the scattering amplitude F can be written as,

$$F = \sum_{\mathbf{G}} \int dV n_{\mathbf{G}} \exp[i(\mathbf{G}-\Delta\mathbf{k})\cdot\mathbf{r}] \quad (3.9)$$

where $\mathbf{k}+\Delta\mathbf{k} = \mathbf{k}'$. For ($\mathbf{G} = \Delta\mathbf{k}$) F is a maximum and $F = V \sum_{\mathbf{G}} n_{\mathbf{G}}$ showing that the scattering amplitude is a function of the fourier coefficients $n_{\mathbf{G}}$. The width of a peak for a one dimensional lattice goes as the inverse of the number of atoms,⁽⁹⁴⁾

$$\sigma = 2\pi/M \quad (3.10)$$

where M is the number of atoms.

It is convenient to rewrite 3.9 at $\mathbf{G}=\Delta\mathbf{k}$ as the integral over one cell multiplied by the number of cells. The scattering amplitude for one cell is known as the structure factor $F_{\mathbf{G}}$.⁽⁹⁸⁾

$$F_{\mathbf{G}} = \int_{\text{cell}} dV n(\mathbf{r}) \exp(-i\mathbf{G}\cdot\mathbf{r}) \quad (3.11)$$

The electron concentration function can also be written as the superposition of electron concentrations n_j of each atom of a cell.⁽⁹⁷⁾

$$n(\mathbf{r}) = \sum_{j=1}^s n_j(\mathbf{r}-\mathbf{r}_j) \quad (3.12)$$

where s is the number of atoms in a cell. The scattering amplitude then becomes,

$$F_{\mathbf{G}} = \sum_j \int dV n_j(\mathbf{r}-\mathbf{r}_j) \exp(-i\mathbf{G}\cdot\mathbf{r}) \quad (3.13a)$$

$$= \sum_j \exp(-i\mathbf{G}\cdot\mathbf{r}_j) \int dV n_j(\rho) \exp(-i\mathbf{G}\cdot\rho) \quad (3.13b)$$

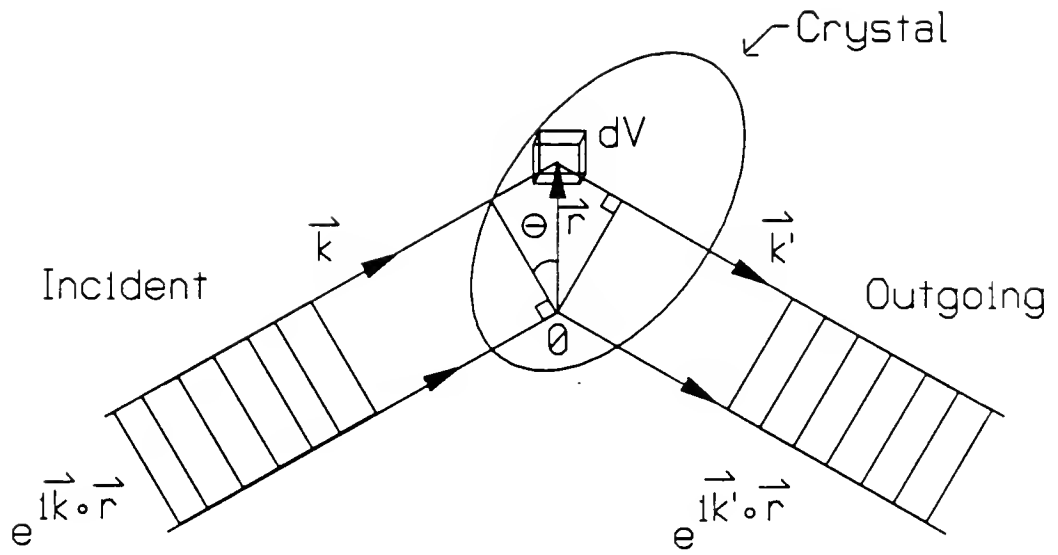


FIG. 4. Difference in path length between two wave vectors scattered from points 0 and \vec{r} . The total difference in phase angle is $(\vec{k} - \vec{k}') \cdot \vec{r}$. The corresponding difference in phase between wave vectors scattered from dV at \vec{r} and 0 is $\exp[i(\vec{k} - \vec{k}') \cdot \vec{r}]$.

where $\mathbf{s} = \mathbf{r} - \mathbf{r}_j$. Defining the atomic form factor f_j ,

$$f_j = \int dV n_j(\mathbf{s}) \exp(-i\mathbf{G} \cdot \mathbf{s}) \quad (3.14)$$

it is apparent that f_j contains the same information as n_j and the structure factor becomes,

$$F_G = \sum_j f_j \exp(-i\mathbf{G} \cdot \mathbf{r}_j). \quad (3.15)$$

The scattering amplitude is usually written in terms of the integers v_1, v_2, v_3 , replaced by h, k, l and \mathbf{r}_j in units of the crystal lattice $\{\mathbf{r}_j = x_j \mathbf{a}_1 + y_j \mathbf{a}_2 + z_j \mathbf{a}_3\}$,

$$F_G = \sum_j f_j \exp[-2\pi i(hx_j + ky_j + lz_j)]. \quad (3.16)$$

The intensity is proportional to $F^* F$, where F^* denotes the complex conjugate of F . Therefore, F_G does not need to be real, and hence, is not directly observable. In addition, F_G is defined in terms of a cell or basis, where there is freedom in the choice of a cell.

The scattered intensity is more naturally described in terms of a correlation function. The time independent pair correlation function is defined in real space as,

$$G(\mathbf{r}) = \frac{1}{N} \int \langle \hat{\rho}(\mathbf{r}' - \mathbf{r}) \hat{\rho}(\mathbf{r}') \rangle d^3 \mathbf{r}' \quad (3.17)$$

where $\hat{\rho}(\mathbf{r}')$ is the charge density at position \mathbf{r}' , and $\langle \rangle$ represent a thermodynamic average. $G(\mathbf{r})$ is an equilibrium quantity. The fourier transform of $G(\mathbf{r})$ is commonly called the structure factor, $S(\mathbf{Q})$.

$$S(\mathbf{Q}) = \frac{1}{\sqrt{2\pi}} \int \exp(i\mathbf{Q} \cdot \mathbf{r}) G(\mathbf{r}) d^3 \mathbf{r} \quad (3.18)$$

If the system of interest is in a non-equilibrium state the structure factor becomes a function of both position and time, $S(\mathbf{Q}, t)$.

Some confusion may arise between structure factor $S(\mathbf{Q}, t)$ and the time dependent equilibrium structure factor normally written $S(\mathbf{Q}, t)$ which refers to fluctuations about equilibrium as opposed to the approach to equilibrium. Here $S(\mathbf{Q}, t)$ is a non-equilibrium $S(\mathbf{Q})$ at a time t , the time is added to emphasize the fact that we are measuring a non-equilibrium function. Another confusion in

definitions comes from the scattering amplitude \mathbf{F} historically being called a structure factor. In older text books on x-ray scattering \mathbf{F} is commonly called a structure factor. Although $\mathbf{F}^* \mathbf{F}$ and $\mathbf{S}(\mathbf{Q})$ are interchangeable, physicists generally use \mathbf{S} . The newer theories use \mathbf{S} and the older theories often use \mathbf{F} . Since 1954, following a paper published by Leon Van Hove, physicists have preferred to use $\mathbf{S}(\mathbf{Q})$. In Van Hove's paper equation 3.18 is derived in the Born approximation.⁽⁹⁹⁾ In the above discussion and throughout this work $\mathbf{S}(\mathbf{Q},t)$ is a non-equilibrium quantity, and \mathbf{F} will be call the scattering amplitude.

Diffraction with Cu_3Au and its Relation to the Order Parameter

For an fcc lattice the usual choice of a basis is one corner atom at $[0,0,0]$, and three face centers at $[0, \frac{1}{2}, \frac{1}{2}]$, $[\frac{1}{2}, 0, \frac{1}{2}]$, and $[\frac{1}{2}, \frac{1}{2}, 0]$. For this choice,

$$\mathbf{F}(h,k,l) = f_{\text{atom}} \{1 + \exp[-\pi i(k+l)] + \exp[-\pi i(h+l)] + \exp[-\pi i(h+k)]\}. \quad (3.19)$$

If the indices (h,k,l) are unmixed (all even or all odd) $\mathbf{F}_G = 4f_{\text{atom}}$. If the indices are mixed (2 even 1 odd, or 1 even 2 odd) two of the exponents will be odd multiples of $-\pi i$ and one even, so \mathbf{F}_G will vanish.

The above assumes that only one type of atom makes up the crystal. This is not the case for Cu_3Au . The values of f_{Au} and f_{Cu} can be found in the international tables for x-ray crystallography Vol. 3.⁽¹⁰⁰⁾ Since a real sample of Cu_3Au is never fully ordered, a partially ordered sample should be considered. The following discussion is a long-range order theory only, and is equivalent to the Bragg-Williams theory.⁽⁴⁾ Starting with the fraction of Cu and Au atoms located at corner and face center sites a definition of long range order $[L]$ can be introduced.⁽⁹⁰⁾ This long range order variable L is not the same as a long range order parameter used in statistical mechanics even though it was originally named

as such. Here long range order L is defined in terms of the occupancy of lattice sites.

$$\begin{aligned} r_c &= \text{fraction of Au atoms on a cube corner} \\ w_c &= \text{fraction of Cu atoms on a cube corner} \\ r_f &= \text{fraction of Cu atoms on a face center} \\ w_f &= \text{fraction of Au atoms on a face center} \end{aligned}$$

where r stands for right type of atom, w for wrong type, c for corner, and f for face center. Of these four variables three are dependent, hence, a few results are immediately obvious,

$$r_c + w_c = 1; \quad r_f + w_f = 1 \quad (3.20)$$

$$\frac{1}{4}r_c + \frac{3}{4}w_f = x_{\text{Au}} \quad \begin{array}{l} \text{the fraction of} \\ \text{gold atoms} \end{array} \quad (3.21)$$

$$\frac{3}{4}r_f + \frac{1}{4}w_c = x_{\text{Cu}} \quad \begin{array}{l} \text{the fraction of} \\ \text{copper atoms} \end{array} \quad (3.22)$$

where the fractions $\frac{1}{4}$ and $\frac{3}{4}$ refer to the concentration of corner and face center sites respectively. Long range order can now be defined,

$$L = r_c + r_f - 1 = r_c - w_f = r_f - w_c \quad (3.23)$$

The order variable defined this way is one, if the sample is fully ordered, and zero, if the sample is fully disordered. Using 3.19 or 3.20 the last dependent variable can be eliminated,

$$L = (r_c - x_{\text{Cu}}) / \frac{3}{4} = (r_f - x_{\text{Au}}) / \frac{1}{4}. \quad (3.24)$$

The scattering amplitude for crystalline Cu_3Au is a function of the occupation of sites and the atomic form factors for Cu and Au as defined in equation 3.19.

Therefore, the relation between the scattering amplitude and the order variable is easily derived.⁽⁹⁰⁾ Dividing the sum in 3.18 up into sums over cube corners and face centers gives,

$$\begin{aligned} F = & \sum_{\text{corners}} (r_c f_{\text{Au}} + w_c f_{\text{Cu}}) \exp[2\pi i(hx_c + ky_c + lz_c)] \\ & + \sum_{\text{faces}} (r_f f_{\text{Cu}} + w_f f_{\text{Au}}) \exp[2\pi i(hx_f + ky_f + lz_f)]. \quad (3.25) \end{aligned}$$

The only corner is at [0,0,0]. Substituting the corner position for [h,k,l] as well as the face center positions as done to get 3.16 it is found that for unmixed (h,k,l),

$$F = (r_c f_{Au} + w_c f_{Cu}) + 3(r_f f_{Cu} + w_f f_{Au}) \quad (3.26a)$$

$$= (r_c + 3w_f) f_{Au} + (w_c + 3r_f) f_{Cu} \quad (3.26b)$$

$$= 4\left(\frac{1}{4}r_c + \frac{3}{4}w_f\right) f_{Au} + 4\left(\frac{1}{4}w_c + \frac{3}{4}r_f\right) f_{Cu} \quad (3.26c)$$

$$= 4(x_{Au} f_{Au} + x_{Cu} f_{Cu}) \quad (3.26d)$$

and for mixed (h,k,l),

$$F = (r_c f_{Au} + w_c f_{Cu}) - (r_f f_{Cu} + w_f f_{Au}) \quad (3.27a)$$

$$= (r_c - w_f) f_{Au} - (r_f - w_c) f_{Cu} \quad (3.27b)$$

$$= L(f_{Au} - f_{Cu}) \quad (3.27c)$$

where f_N is the atomic form factor for N, and x_N is the atomic fraction of atom N. For stoichiometric Cu_3Au , $x_{Au} = 1/4$, and $x_{Cu} = 3/4$. The unmixed indices or fundamental peaks are just those for an fcc crystal with an amplitude corresponding to scattering from an average atom $[(3f_{Cu} + f_{Au})/4]$ for stoichiometric Cu_3Au . The scattered intensity is the structure factor multiplied by its complex conjugate. Therefore, the intensity of a mixed indices or superlattice reflection is proportional to the square of the difference between the atomic form factors for Cu and Au, multiplied by the square of the order variable. Hence, from a comparison of the intensity of a superlattice peak relative to a fundamental, the long range order variable (L) can be theoretically determined.

In real applications there are several effects which can produce sizable errors.⁽⁹⁰⁾ Extinction effects from different grains can reduce the intensities of fundamentals, hence, high-order peaks should be used in the calculation.

Nevertheless, the intensity of a superlattice reflection is proportional to the square of the long range order variable.

In the modern theories a proper order parameter must be used. Often the systems investigated are equivalent to Ising models, and therefore, have a one component order parameter. For the COP process of phase separation the order parameter is the local concentration of one of the two types of atoms. This is equivalent to an Ising model with Kawasaki (spin exchange) dynamics with the order parameter defined as the total magnetization. For order-disorder transitions the analogous Ising model also uses Kawasaki dynamics only now the order parameter is the magnetization on a sub-lattice, which is not conserved. Cu_3Au can be described by a three component order parameter.^(92,101) In a detailed theory of Lai⁽⁹²⁾ the three component order parameter is defined in terms of the occupation of sites on one of four interpenetrating simple cubic sublattices described by Ising like occupation numbers s_i ,

$$s_i = \begin{cases} +1 & \text{if occupied by Cu} \\ -1 & \text{if occupied by Au} \end{cases} \quad (3.28)$$

where $i = 1, 2, 3$, and 4 corresponding to the four equivalent ways of defining a cube corner in the FCC lattice or equivalently the four cubic sublattices. On the basis of symmetry Lai constructs the order parameter according to the Landau Lifshitz rules,

$$\Psi_1(\mathbf{R}) = \frac{\Psi}{2} [\bar{s}_1(\mathbf{R}) - \bar{s}_2(\mathbf{R}) - \bar{s}_3(\mathbf{R}) + \bar{s}_4(\mathbf{R})] \quad (3.29a)$$

$$\Psi_2(\mathbf{R}) = \frac{\Psi}{2} [\bar{s}_1(\mathbf{R}) - \bar{s}_2(\mathbf{R}) + \bar{s}_3(\mathbf{R}) - \bar{s}_4(\mathbf{R})] \quad (3.29b)$$

$$\Psi_3(\mathbf{R}) = \frac{\Psi}{2} [\bar{s}_1(\mathbf{R}) + \bar{s}_2(\mathbf{R}) - \bar{s}_3(\mathbf{R}) - \bar{s}_4(\mathbf{R})]. \quad (3.29c)$$

Using conservation of atoms a conserved concentration Ψ can be written,

$$\Psi = \frac{\Psi}{2} [\bar{s}_1(\mathbf{R}) + \bar{s}_2(\mathbf{R}) + \bar{s}_3(\mathbf{R}) + \bar{s}_4(\mathbf{R}) - 2]. \quad (3.30)$$

From here an equation of motion is found using a Ginzburg-Landau potential. The square modulus of the order parameter used in modern theories is proportional to the intensity of a superlattice peak.

When, as is the case for binary alloys, the order parameter is proportional to the charge density (atomic concentration), the charge density correlation function is directly proportional to the order parameter correlation function. Therefore, the structure factor measured in the scattering experiment is linearly proportional to the order parameter correlation function which is normally modeled theoretically.

Anisotropy in Cu_3Au

The solid Cu_3Au solution forms a fcc crystal and below $T_c \approx 390^\circ\text{C}$ orders in the L1_2 structure (Au on the corners, Cu on the face centers as in figure 1) with a ground-state degeneracy of $p=4$. The four different phases correspond to redefining the cube corners as one of its three nearest face centers, and of course the original phase one started with. Mathematically one shifts the position of the ordered state by 0, $(a_1+a_2)/2$, $(a_1+a_3)/2$ or $(a_2+a_3)/2$. The presence of domain walls leads to anisotropic line shapes in superlattice peaks as discussed below.

Two types of domain walls exist in Cu_3Au . Type-1 walls⁽²¹⁾ are easily formed due to their low energy. These walls can be formed by displacing the atoms on one side of a plane perpendicular to the a_3 axis by $(a_1+a_2)/2$ as in figure 5. Type-1 walls can also be formed by any cyclic permutation of (a_1, a_2, a_3) in the above method. A Type-2 wall can be formed by displacing the atoms on one side of a plane perpendicular to a_3 by $(a_1+a_3)/2$, as in figure 6. The important difference between type-1 and type-2 walls is that type-1 walls conserve the nearest neighbor configuration where type-2 walls do not. The type-2 wall in figure 3 has gold atoms as nearest neighbors, one could form a slightly different type-2 wall say type-2b by redefining all the Au atoms to be Cu atoms and all the in plane Cu atoms to be Au. Type-2b walls have Cu atoms as nearest neighbors in the wall

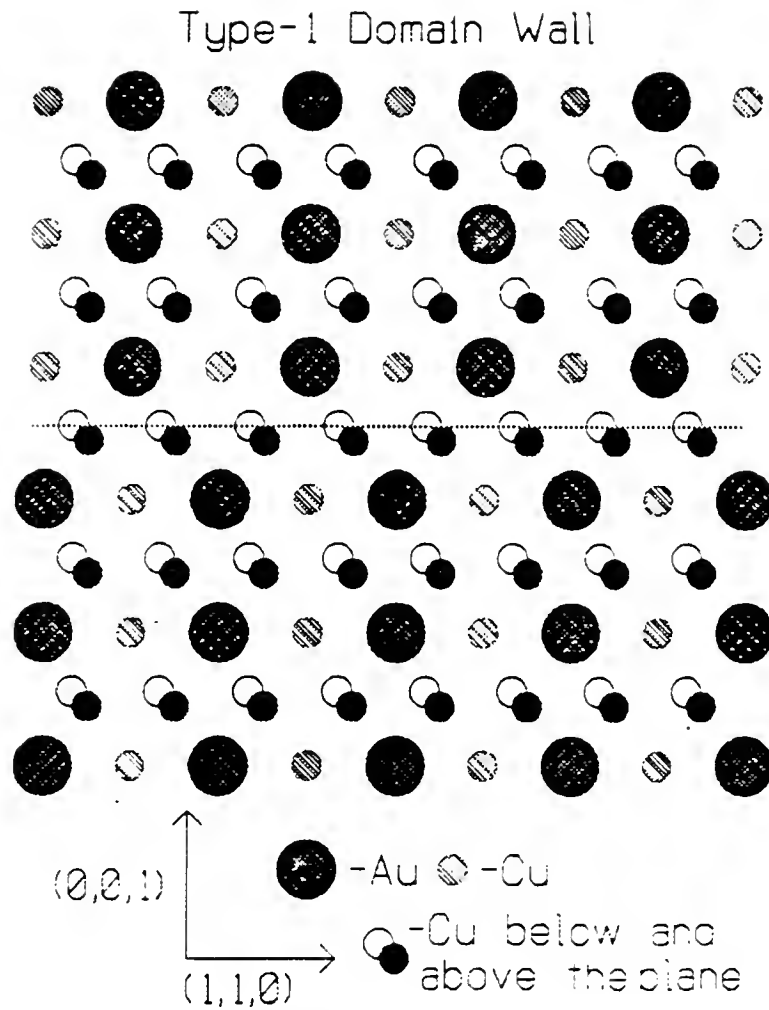


FIG. 5. Domains of different phase separated by a type-1 domain wall as described in the text. The line marks the position of the wall.

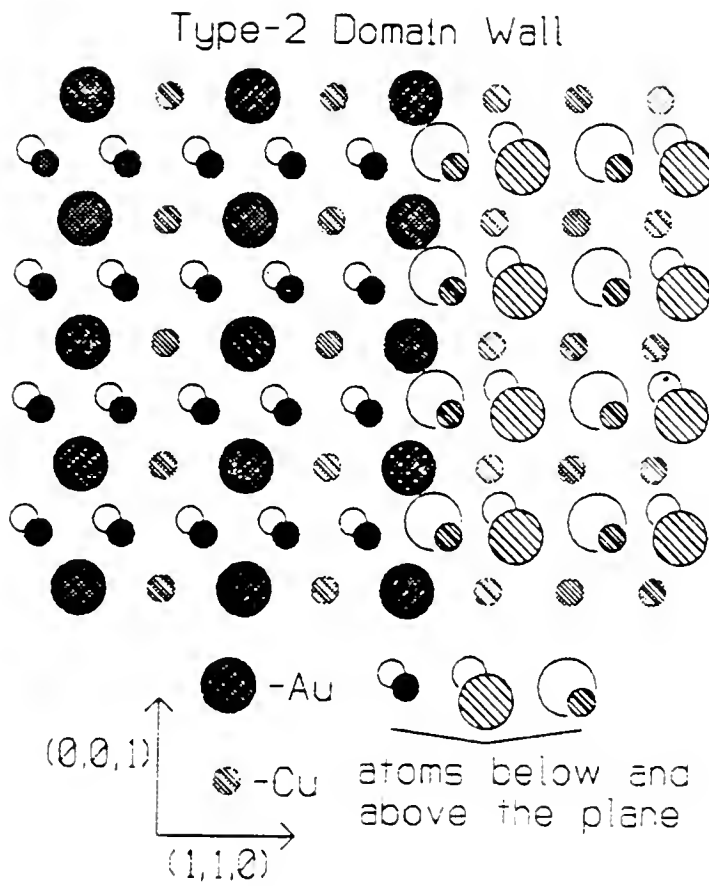


FIG. 6. Domains of different phase separated by a type-2 domain wall as described in the text.

instead of Au atoms as in type-2a walls. Moreover, if one looks in a direction perpendicular to a type-2 wall one finds planes of all Cu alternating with planes of half Au and half Cu, the difference between type-2a and type-2b walls is just which of the two types of planes is repeated to create the wall. In order to move a type-2 wall there must be some diffusion of atoms due to the off stoichiometry of the wall. On the other hand a type-1 wall can be moved by shifting the wall up or down by $(a_1+a_2)/2$, hence, it is often called a half-diagonal glide domain wall. This difference posed the question of whether the two types of walls grow at the same rate or not. If the two walls do not grow at the same rate then scaling would not be valid.

One way to measure the anisotropic profile is to look in both the radial and transverse directions during coarsening. This corresponds to observing the motion of both types of walls. At the $[1,0,0]$, the radial direction probes type 1 walls and the transverse type 2. At the $[1,-1,0]$, the situation is almost reversed, the radial direction probes type 2 walls and a specific transverse direction probes type-1. So another way to consider both types of walls is to observe the $[1,0,0]$ and the $[1,-1,0]$ in the radial (or transverse) direction. In this study the validity of scaling during coarsening in an anisotropic system is established. The fact that both walls behave in the same way suggest it is the same mechanism driving the growth in all directions. In figures 5 and 6 straight domain walls have been shown, however, the growth is curvature driven suggesting that a curved wall should be considered. A curved wall is shown in figure 7, in it one can find elements for all types of walls. Although it is possible to envision this wall growing with different velocities in different directions, that has been found not to be the case.

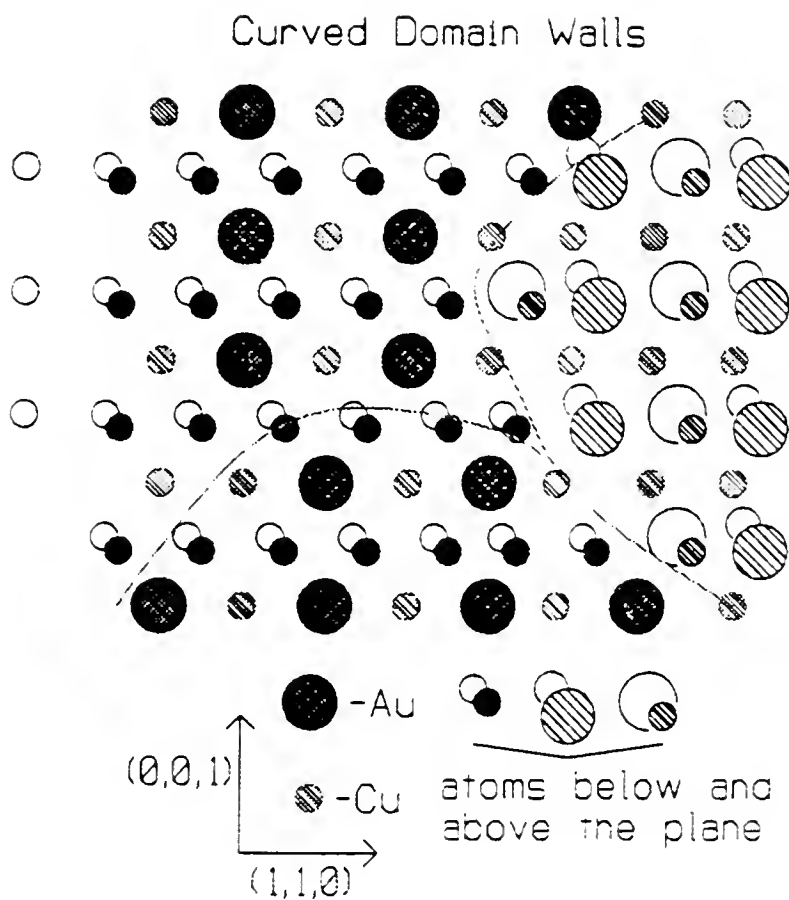


FIG. 7. Domains of three different phases separated by curved domain walls constructed from a combination of both type-1 and type-2 walls.

The Effect of Type 1 Walls on Scattering.

The width of a superlattice peak is of course greatly affected by the existence of domain walls. In the following consideration of the scattering a number of assumptions are made: 1. type 2 walls are not present, 2. the half diagonal glide domain boundaries perpendicular to each of the axes are completely independent from each other, and 3. the intensity drops off sharply away from the peak (a small q approximation). For convenience the convention that all superlattice peaks be written such that h and l have the same parity has been adopted. The shape of the peak, as shown in appendix A, can then be written as (in reduced units),

$$I(h_1 h_2 h_3) = F^2 \frac{N_1 a}{a^2 + (\pi h_1)^2} \frac{\sin^2(\pi N_2 h_2)}{(\pi h_2)^2} \frac{N_3 a}{a^2 + (\pi h_3)^2} \quad (3.31)$$

where h_1 , h_2 , and h_3 represent the departure of the diffraction vector from the $[h, k, l]$ peak position [ie., $q = (2\pi/a) \cdot (h_1, h_2, h_3)$, $Q = G + Q$, $G = (2\pi/a) \cdot (h, k, l)$], and a is the probability of crossing an anti-phase domain boundary in a distance a . The intensity for a superlattice peak as given above is roughly a thin disk lying in the $h_1 h_3$ plane with a thickness determined by the crystal dimension $N_2 a_2$. type 2 walls would, of course thicken the disk. Figure 8 shows the orientations of theses disks for one plane of reciprocal space. Also this equation shows that the radius of the disk increases with the probability a of anti-phase boundaries.

Normally, the condition $I(h_1 h_2 h_3)$ equal to $(1/2)I(h_1 h_2 h_3)$ would be used to define the width of the peak in terms of L . However, the approximation of $h_1 h_2 h_3$ being small lead to problems. Therefore, one starts with a more general equation for the width.⁽⁹⁰⁾

$$\text{FWHM} \propto \frac{\int_0^\infty I \, dq}{I_{\max}} \quad (3.32)$$

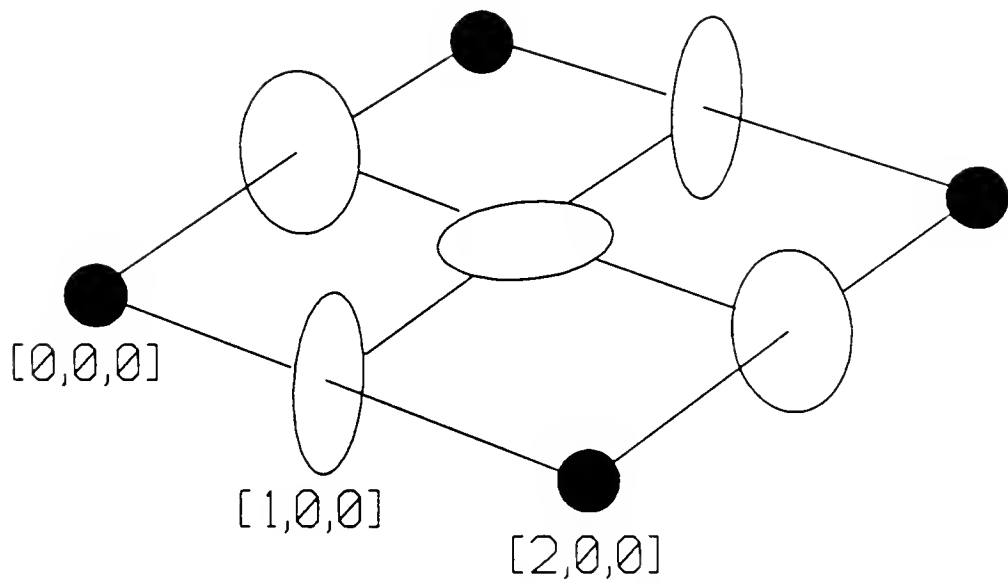


FIG. 8. Shapes of the reflections in reciprocal space for type 1 walls normal to the three axes. The fundamental reflections are spheres, and the superlattice reflections are disk-shaped.

Also in appendix A, the relation between domain size and superlattice peak width is shown from 3.32 to be,⁽⁹⁰⁾

$$\text{FWHM} \propto (2\pi/L) \frac{(|h| + |k|)}{\sqrt{h^2 + k^2 + 1}}. \quad (3.33)$$

This result is for type 1 walls, however, type 2 walls also produce broadening with a $2\pi/L$ dependence. The correction of 2.21 for the $[0,1,0]$ type peak is one, and for the $[1,0,\bar{1}]$ is $\sqrt{2}$. For a given functional form equation 3.32 can be used to relate the corresponding width to L . For a gaussian with width σ , defined as,

$$F(x) = A \cdot \exp \left[-\frac{(x-x_0)^2}{2\sigma^2} \right] \quad (3.34)$$

equation 3.33 gives,

$$\sigma = (\sqrt{2}\pi/L) \frac{(|h| + |k|)}{\sqrt{h^2 + k^2 + 1}} \quad (3.35)$$

where as for a lorentzian squared with width Γ , defined as,

$$F(x) = \left[1 + \frac{1}{2} \left[\frac{(x-x_0)}{\Gamma} \right]^2 \right]^{-2} \quad (3.35)$$

equation 3.33 gives,

$$\Gamma = (\sqrt{2}\pi/L) \frac{(|h| + |k|)}{\sqrt{h^2 + k^2 + 1}}. \quad (3.36)$$

The reader should be aware of the above corrections for type 1 walls. However, throughout this work it is assumed that 2.21 is correct for both types of walls.

CHAPTER 4 EXPERIMENTS

The Bulk Single Crystal

Experimental Details

The crystalline sample of Cu_3Au used in these experiments was cut at Oak Ridge National Laboratories to expose the $[h,0,0]$ face. In order to remove any oxidation the surface was etched in nitric acid and then annealed for 12 hours at 700°C under an Ar atmosphere.

The furnace used in these experiments is composed of an evacuable chamber and a heating element. Heating was performed by running AC current through a 0.003mm diameter tungsten coil wrapped around a 9mm diameter copper rod that had been covered with a 1.5mm thick layer of electrically insulating boron nitride. The tungsten coil consisted of 20 to 25 loops covering a length of 35mm. The sample was mounted to the rod as shown in figure 9. This heating rod is placed in the chamber which is equipped with a 360° Beryllium window. Beryllium is a light metal that is almost transparent to 8 KeV x-rays. The tantalum shown in figure 9 was used to keep Cu from diffusing from the mount into the sample. Tantalum foil was also placed above the copper rod for the same reason.

A proportional relay (Douglas Randall model RD04A) was used to control the current to the heating coil, and hence, the temperature. The proportional relay was connected to a model 828D Micristar temperature controller which used a K-thermocouple placed at the top of the copper rod to get a reference temperature.

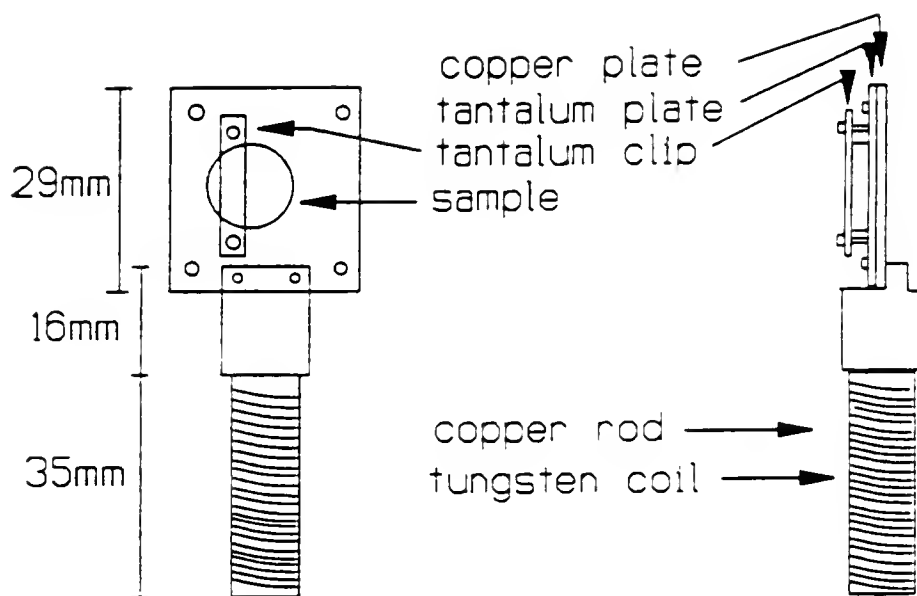


FIG. 9. Heating element and sample mount used in connection with the bulk sample, the sputtered films, and the 4500 Å (M.B.E.) film.

In the initial experiments quenches were done by putting the Micristar on manual which fixed the current, then the Micristar's temperature set point was changed to 2 to 5°C above the final post temperature desired. Next the current was turned off at the source allowing the sample to cool. As the post temperature reached the Micristar's new set point the current source was turned back on and the Micristar put on automatic. The system would soon reach an almost constant temperature a few degrees below the set point. If left alone the system temperature would slowly be raised till it reached the set point. Therefore, the Micristar was temporarily put on manual and the set point lowered to the post temperature. The Quenches took place in 30 to 90 seconds depending on depth. Quench times were measured from when the temperature crossed T_c to when the temperature was within one degree celsius of the final temperature. The quenches did not over shoot but smoothly went to the final temperature. The quenches were significantly improved in later experiments as will be disused in connection with the M.B.E. films.

In addition to the thermocouple used for temperature control there also was a K-thermocouple held directly onto the face of the sample. The temperature difference between the sample and the top of the heating rod was about 9°C. The vast majority of this gradient existed in the tantalum plate protecting the sample from the Cu plate. The gradient across the sample is believed to be small due to the geometry of the heater. Moreover, an estimate of the gradient suggests that the temperature gradient across the sample was 0.01C/mm. This estimate was based on the thermal conductivity of Cu and Au and the Stefan-Boltzmann law, weighted by the emissivity of Cu and Au. The x-ray spot size on the sample was roughly $1 \times 6 \text{ mm}^2$, consequently the temperature difference within the area of interest was about 0.06°C. The temperature control was good to $\pm 0.3^\circ\text{C}$ over several hours and $\pm 0.5^\circ\text{C}$ over several days. Therefore, the gradient was negligible relative to the temperature stability.

In order to determine the transition temperature the intensity of the $[0,1,0]$ peak was recorded as a function of time for several temperatures after raising the temperature from below T_c to near T_c . The intensity at each temperature was then plotted as a function of inverse time and the curve was extrapolated to $1/\text{time} = 0$. At 385.2°C the peak was observed for 3.5 hours and the extrapolation suggested that the sample would almost disorder but not completely. On the other hand at 385.7°C the peak was nearly gone after 1.5 hours and the extrapolation clearly showed that the sample was above T_c . The transition temperature was then taken to be the value of a weighted average based on the extrapolations, and found to be 385.3°C . This extrapolation is not very important because the temperatures used are only half a degree apart, but it was clear that the transition was closer to $385.2 \pm 0.5^\circ\text{C}$ than $385.7 \pm 0.5^\circ\text{C}$.

The wavelength of the x-rays used is named from the core electron levels of the metal target used in the Rigaku RU300. The doublet line of Cu is referred to as CuK^a ($\lambda = 1.54178\text{\AA}$) or just K^a . The two components of this doublet line are K_1^a ($\lambda = 1.54051\text{\AA}$) and K_2^a ($\lambda = 1.54433\text{\AA}$).

The x-rays were produced by a rotating anode. The major components of a rotating anode are, the anode and cathode or filament. To produce x-rays, electrons are accelerated by a potential difference from the filament to the anode or target. In so doing x-rays are produced in several ways. The first is from bremsstrahlung, the sudden deceleration of the electrons. The second is through the process of exciting core energy levels of the metal target, which then decay producing x-rays of specific wavelengths. Almost all of the work done here used a Cu target. The most intense core energy levels are labeled K^a and K^β . This method of x-ray production is very inefficient, only about one percent of the energy used goes into the production of CuK^a radiation. The majority of the energy goes into heating the

target. Therefore, the target must be cooled. Tube sources have a fixed target that is typically cooled by running water. Tube sources at best are run at around 3kW. In order to increase the intensity the anode (or target) is rotated increasing the area that is heated. In such cases the anode is in the shape of a cylindrical bowl that is rotated about the axis of the cylinder with the electrons bombarding the side.

For geometrical reasons the resolution or spot size is best at smaller angles. An angle of six degrees as measured from the surface of the target was used here. Six degrees gives a 1 to 10 reduction of the spot size. Other commonly used angles are 3, 9, and 12 degrees.

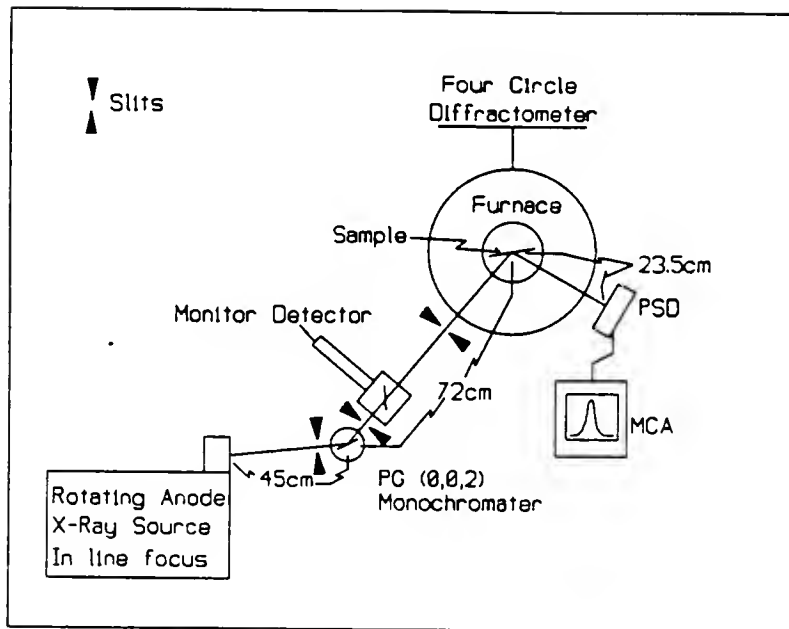
The RU300 can be operated in two different geometries (point or line focus). If the filament is mounted perpendicular to the scattering plane associated with the Huber diffractometer, then the anode must spin in the scattering plane. The electrons must then hit the anode in a line perpendicular to the scattering plane. This produces a bar or line of x-rays perpendicular to the scattering plane. If the situation is reversed then the bar lies in the plane at an angle of 6 degrees to the direction of the incident beam. The projection of this bar onto a cross section of beam perpendicular to its motion is a point. For a PSD a line focus has better instrumental resolution than a point focus, but the point focus generally gives higher counting rates, because more of the x-rays are focused onto the sample.

The optics following the x-ray source differ according to whether the direction scanned in reciprocal space was parallel to the ordering vector Q (radial scan) or perpendicular to Q (transverse scan). Radial scans probe reciprocal space along a line that passes through the origin and the peak in question. Hence, in a radial scan the magnitude of Q is directly varied. Mathematically any point in a radial scan is definable as $(c \cdot h, c \cdot k, c \cdot l)$ where c is a real number. For the $[0,1,0]$ a radial scan is along the $[0,k,0]$ direction. Transverse scans in contrast probe a

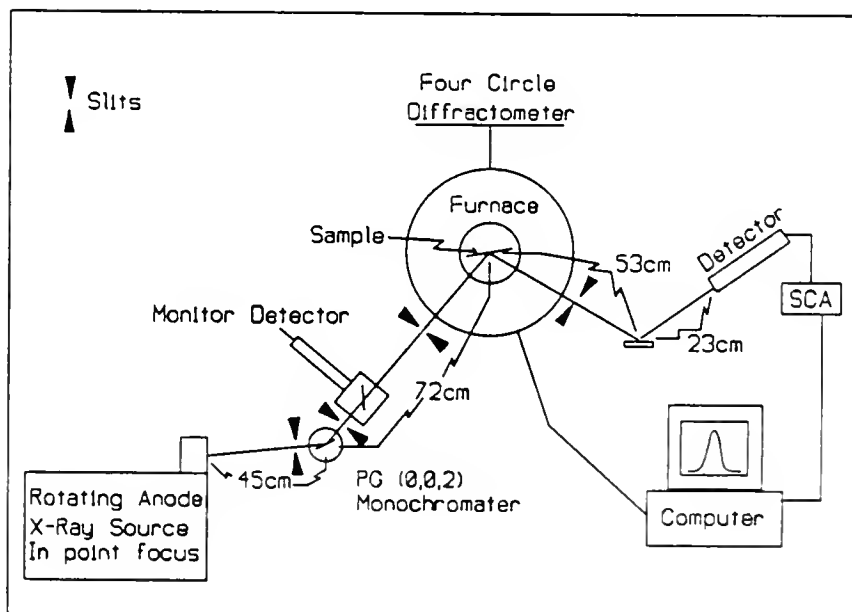
direction perpendicular to the radial direction. For example, at the $[0,1,0]$ a scan that varied h , l , or, a linear combination of the two would be a transverse scan. In this study the magnitude of Q is almost constant in a transverse scan. Hence, a transverse scan is almost identical to a mosaic scan in which the sample is rocked while Q is held fixed.

Recalling the disk shaped scattering profiles for a superlattice peak previously shown in figure 8 a transverse scan of the $[0,1,0]$ is along the diameter of the disk and a radial scan is through the disk. Equation 3.31 implies that type 1 walls do not affect the width in the radial direction at the $[0,1,0]$. Therefore, the radial direction probes type 2 walls only. The transverse direction probes type 1 and 2 walls. However, the broadening in this direction is dominated by type 1 walls.

The sample was placed at the center of rotation of a Huber Eulerian cradle by adjusting an x - y translation at the base of the furnace. Figure 10a and 10b shows schematically the apparatus in the two geometries used; 10a was used to collect the radial data and 10b the transverse data. Set up 10a uses a line focus and a Braun model OEO-50M linear platinum wire based position sensitive detector (PSD). The Braun detector's signal is binned into 1024 channels by a multi channel analyzer. For the sample to detector distance used (23.5cm) each channel corresponds to 0.0125 degrees in 2θ . The window on the PSD was 5cm long which corresponds to a solid angle of 10.3 degrees. The transverse set up (figure 10b) employed a point focus and a Bicron model 1XMP040B scintillation detector. The Bicron's signal was fed into an E.G.&G. Ortec model 590A single channel analyzer which is connected to an E.G.&G. model 974 quad counter/timer. The counter/timer is in turn connected to an IBM XT PC through an I.E.E.E.-488 interface bus. The PC also directs the Huber through a Klinger Scientific MC4



a)



b)

FIG. 10. Lay out of equipment: a) Radial setup b) Transverse setup.

stepping motor controller. Both set ups use a second Bicron detector, interfaced with the PC as an incident intensity monitor, so that fluctuations in intensity can be corrected for.

For the radial set-up over 90% of the K_2^a ($\lambda=1.54433\text{\AA}$) intensity was slit out leaving mostly K_1^a ($\lambda=1.54051\text{\AA}$) where the subscripts define the two components of the doublet line. The slitting out of K_2^a was done on the $[0,2,0]$ peak with the pre-sample slits shown in figure 10a. At the $[0,2,0]$ K_1^a and K_2^a were well separated as opposed to at the $[0,1,0]$ where the two components were not completely resolved. It was important to slit out K_2^a due to the complications it would have added to the resolution correction. In the transverse set-up it was not necessary to do so because of the analyzer. The resulting instrumental resolution for both set-ups, in the corresponding directions of the scans in reciprocal space was $0.003\text{\AA}^{-1}(\text{HWHM})$.

In the above discussion, PSD scans have been called radial scans. A radial scan in real space involves varying the detector angle 2θ while half angling the sample ($\theta=0$). The major difference in a PSD scan relative to a radial scan is the lack of half angling of the sample. The two are approximately the same for small distances about a peak. For the sample to detector distance used the 1024 PSD channels covered ± 6.4 degrees in 2θ . The maximum error in the sample angle is then 3.2 degrees. Typically a range less than 400 channels (or 2.5 degrees) was used in the analysis. At the $[0,1,0]$ the radial direction probes the thin part of $S(Q)$. Therefore it is reasonable to assume that $S(Q)$ is constant (or flat) for small deviations from the radial direction. Under this assumption, a PSD scan differs from a radial scan in reciprocal space by a displacement of 90 degrees from the radial direction of $(Q-q) \cdot \tan(\theta-0)$. For the range used in the analysis, the difference in the distances from Q between the two types of scans is less than 7.7

percent at the end points and 3.4 percent at the mid-points. The mosaic spread of the sample (0.25 degrees) would further lessen the difference between these two types of scans. This small difference between a PSD scan and a radial scan only affects the results in that the width of a PSD scan is slightly dependent on type 1 walls where a true radial scan probes only type 2 walls.

Analysis of the Bulk Data

One of the purposes of this work was to consider the growth kinetics in an anisotropic system. Noda, Nishimura, and Takeuchi⁽⁴³⁾ measured the [1,1,0] superlattice peak in Cu_3Au by time resolved x-ray scattering techniques. They found evidence for scaling of $S(Q,t)$, a Lorentzian-squared line shape, and curvature-driven growth. However, they incorrectly assumed isotropic scattering profiles, casting some doubt on the validity of their conclusions. It was postulated that type 2 walls, which were not considered in this earlier work, would have a slower growth due to the need to diffuse one type of atom relative to the other in moving a type 2 wall. The off stoichiometric nature of type 2 walls that might have caused the growth to become diffusion limited is discussed in chapter 3 section C.

In these experiments the intrinsic x-ray peak width and shape is of interest for several reasons as discussed earlier. Measuring the intrinsic line shape of $S(Q,t)$ is complicated by several extraneous contributions to the line width, arising from the effects of, instrumental resolution, finite grain size, strain, and the mosaic spread. The correction for instrumental resolution is the most important. The accuracy of all results depends heavily on a careful handling of the resolution. The radial data was corrected for instrumental resolution as well as finite size and strain as discussed below. The correction for the transverse direction was further

complicated by the mosaic of the sample. In both set ups the instrumental resolution was measured by placing a perfect Ge single crystal at the sample position and observing the [1,1,1] reflection, which is at an angle near that of the [0,1,0] of our sample. The intrinsic width of a Ge single crystal peak is negligible compared to the instrumental resolution. Estimates of broadening from sample characteristics other than the ordered domain size are made from the broadening of fundamental Cu_3Au bragg peaks. Graphs of the measured instrumental resolution functions are shown in figures 11 and 12 for the radial and transverse set ups respectively. A detailed study, involving both theoretical and experimental determinations of the instrumental resolution function show the complex nature of this function.^(102,103) In this work the instrumental resolution was carefully measured. The validity of the procedure discussed here is supported by the detailed study. The contribution to the width of the [0,1,0] arising from finite size and strain was estimated from radial scans of the [0,2,0] and [0,4,0]. These scans were fit to gaussian profiles, and the resulting widths in degrees were corrected for instrumental resolution assuming the widths add in quadrature ($\sigma_{\text{cor}} = \sqrt{\sigma_{\text{measured}}^2 - \sigma_{\text{res}}^2}$).

Ultimately the effects of finite grain size and strain can be included in an effective resolution function. Finite grain size leads to an identical contribution to the reciprocal space line width of each bragg peak in the sample. Strain can be viewed as providing a distribution of lattice constants, leading to an additional width at each peak that is linearly proportional to Q . To obtain the contribution to the width at the [0,1,0] arising from finite size and strain the [0,2,0] and [0,4,0] corrected widths were converted into units of inverse angstroms and fit to $[a + bQ]$, where a and b are fit parameters and Q is the magnitude of the corresponding scattering vector. The widths due to finite size and strain correspond to a and bQ respectively. The result of this fit suggested that the correction at the [0,1,0] was

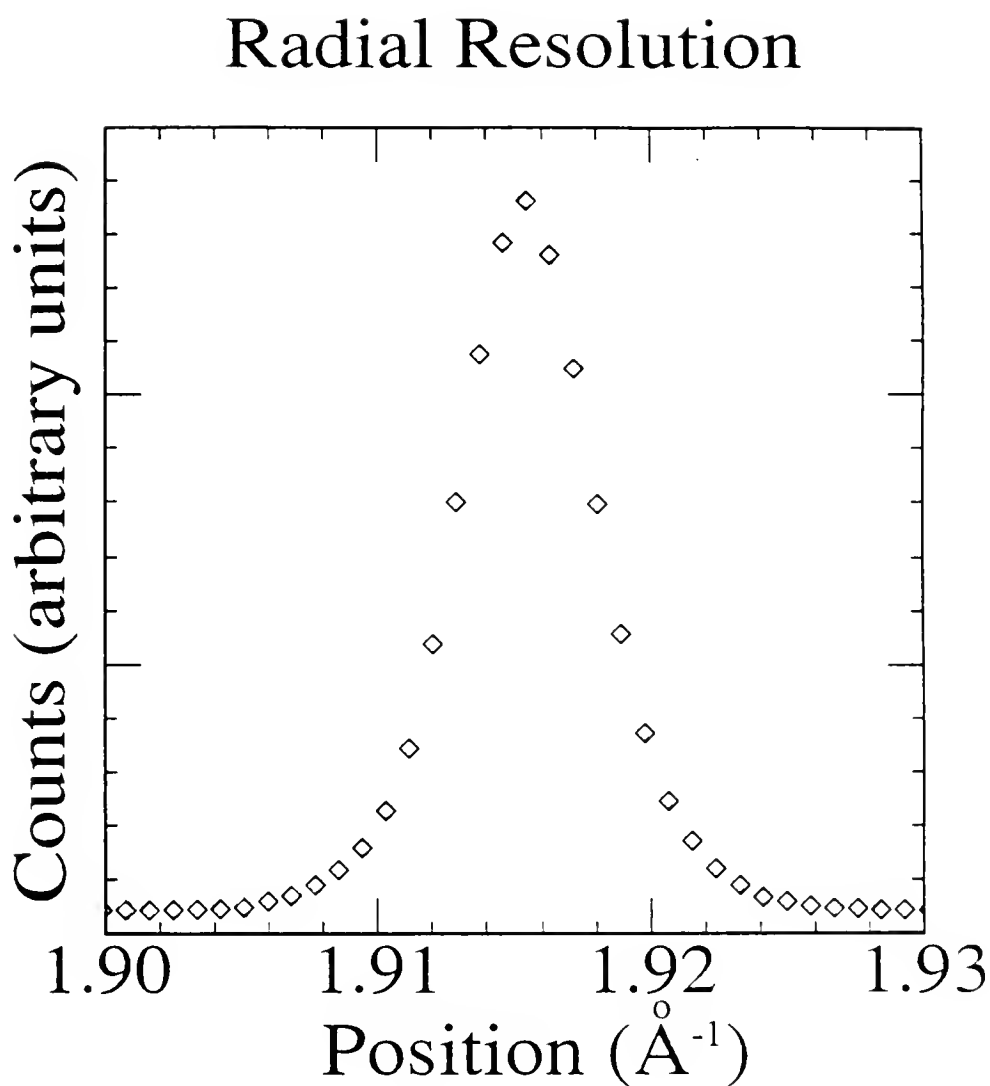


FIG. 11. Scan of Ge [1,1,1] used to measure instrumental resolution in the radial direction. The graph shows only the central portion of the scan, many more points were taken in the tails.

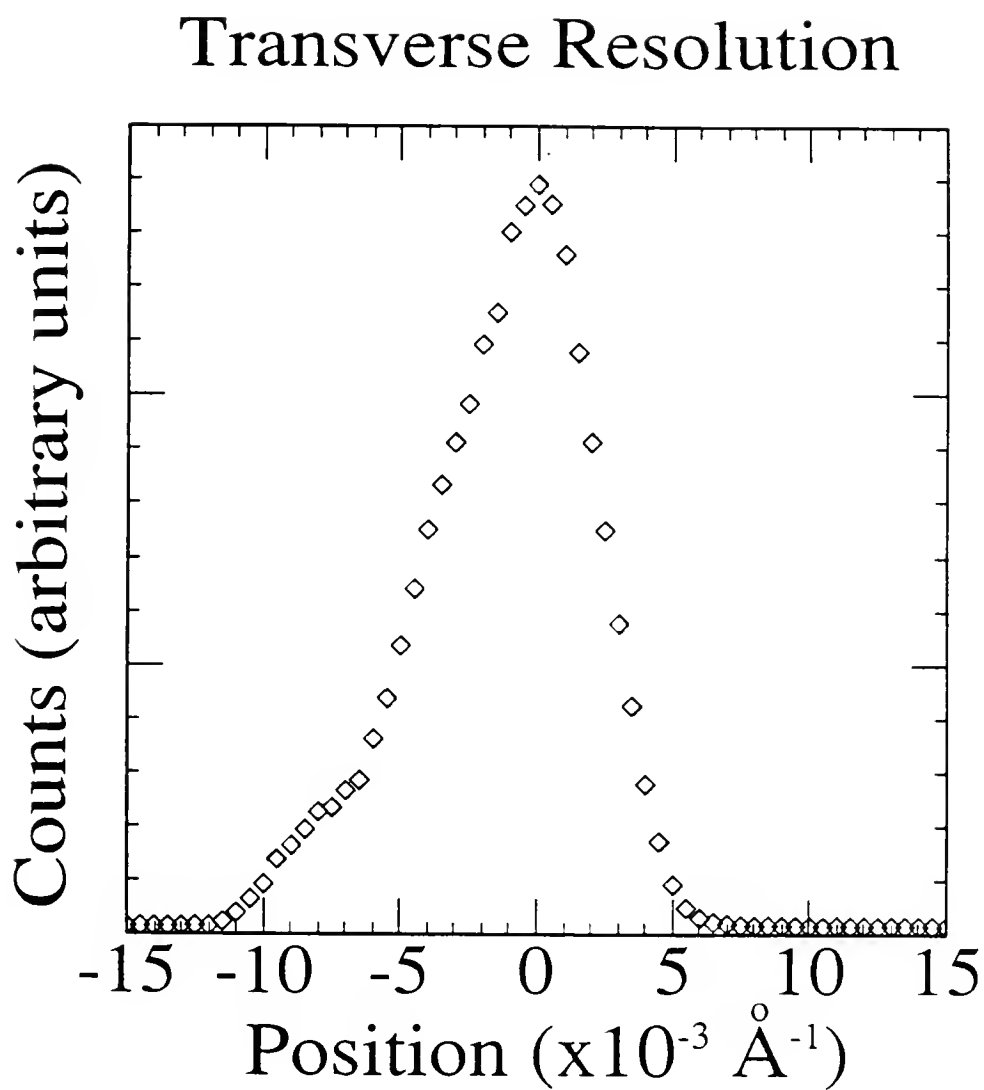


FIG. 12. Scan of Ge [1,1,1] used to measure instrumental resolution in the transverse direction.

0.002\AA^{-1} (FWHM), one third that of the instrumental resolution. One could argue that the widths should be added as $a+bQ^2$, not linearly as was done. If the fits are done this way the correction for finite size and strain becomes ten percent larger and the overall correction 1.4 percent larger. The simplest correction is what was done, this method is equivalent to assuming the widths add like lorentzian widths. The case for using $a+bQ^2$ assumes the widths add like gaussian widths and that the width from strain is small compared to that for finite size, both of which are poor assumptions. In any case the final result is not sensitive to the choice. A high resolution set-up similar to 10b but with a germanium monochromator and analyzer was used to measure the mosaic of the Cu_3Au sample at the $[0,2,0]$. Mosaic spread is a measure of the distribution of orientations of the grains in the sample. The mosaic spread contributes to the each peak a constant angular width in real space, and hence, in reciprocal space is proportional to Q . The transverse scans were taken as a function of Q so the positions in the high resolution scan were converted to Q at the $[0,1,0]$ after a small correction for finite size and strain. The mosaic at the $[0,1,0]$, shown in figure 13, has a FWHM of 0.0044 radians (0.007\AA^{-1}), a value that is a little larger than instrumental resolution.

Initially the data from the bulk sample was fit to a lorentzian squared form and then the width were corrected by subtracting the effective resolution⁽¹⁰⁴⁾. That method, although useful for preliminary analysis, introduces a systematic error. Unlike a lorentzian and a gaussian the convolution of two lorentzian squared functions is not a similarly shaped function, hence, there is not a simple analytical way to remove the resolution from a lorentzian squared fit. In order to correctly account for the resolution the data was fit to the convolution of the resolution function and a model functional form. Although this procedure was a better method, attempts to assign a functional form to the resolution failed to model

Mosaic of Bulk Sample

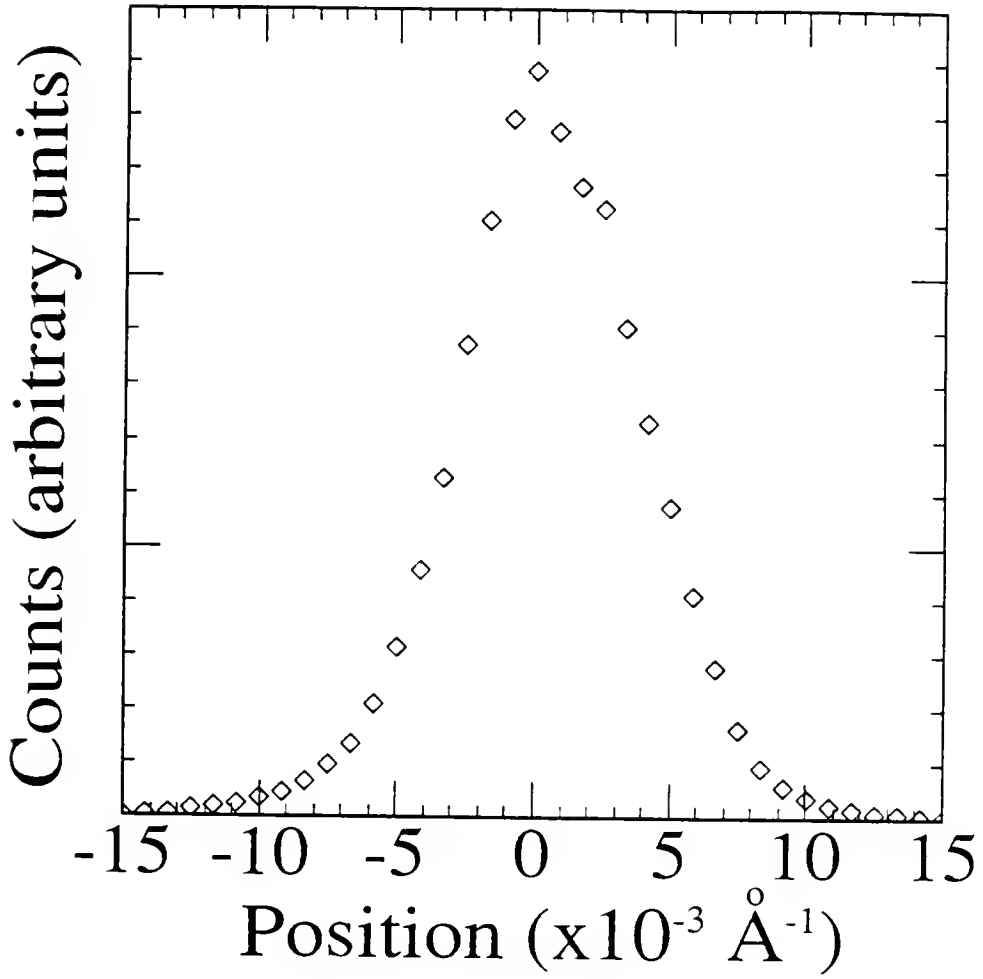


FIG. 13. Scan of the $[0,2,0]$ of Cu_3Au with the position linearly corrected to correspond to the mosaic spread at the $[0,1,0]$.

the data well. The reason for this is simple: The various contributions to the resolution were in general equally poorly fit by a gaussian and/or a lorentzian squared. Other forms fit even worse. The instrumental resolution had a slight asymmetry from slitting, and the mosaic had a little structure in it (see figures 11–12). Therefore, fitting was done by convolving the instrumental resolution data itself point by point with a narrow gaussian representing finite size and stain and the model line shape. This method worked very well for the radial data. The radial data was collected with a PSD as described earlier which took many points in the radial direction minimizing any error from the uncertainty in the shape of the peak. Figure 14 is the result of convolving the instrumental resolution (figure 11) with a gaussian representing finite size and strain. Moreover, the correction in the radial direction did not involve a mosaic spread. In the transverse direction this method also worked well. However, the uncertainty in the line width, which is dominated by errors in the resolution correction, is larger in the transverse data than the radial data. The convolution of the transverse instrumental resolution (figure 12) with a gaussian representing finite size and strain as well as the mosaic (figure 13) is shown in figure 15. Despite the larger absolute resolution correction, the raw transverse data shows changes in the shape of the peak, and hence, $S(Q,t)$ more clearly than the radial data. In fact the resolution is not very important to the change in $S(Q,t)$ because the change occurs early when the resolution correction is small compared to the peak width.

Nucleation is associated with very early times and the equilibration of short range order. The short range order peak intensity is very low, consequently only its existence could be seen by the lack of a long range order peak. However, changes during the growth stage that are revealed through changes in the shape of the scattered intensity are seen. This change is analyzed by fitting the data to both

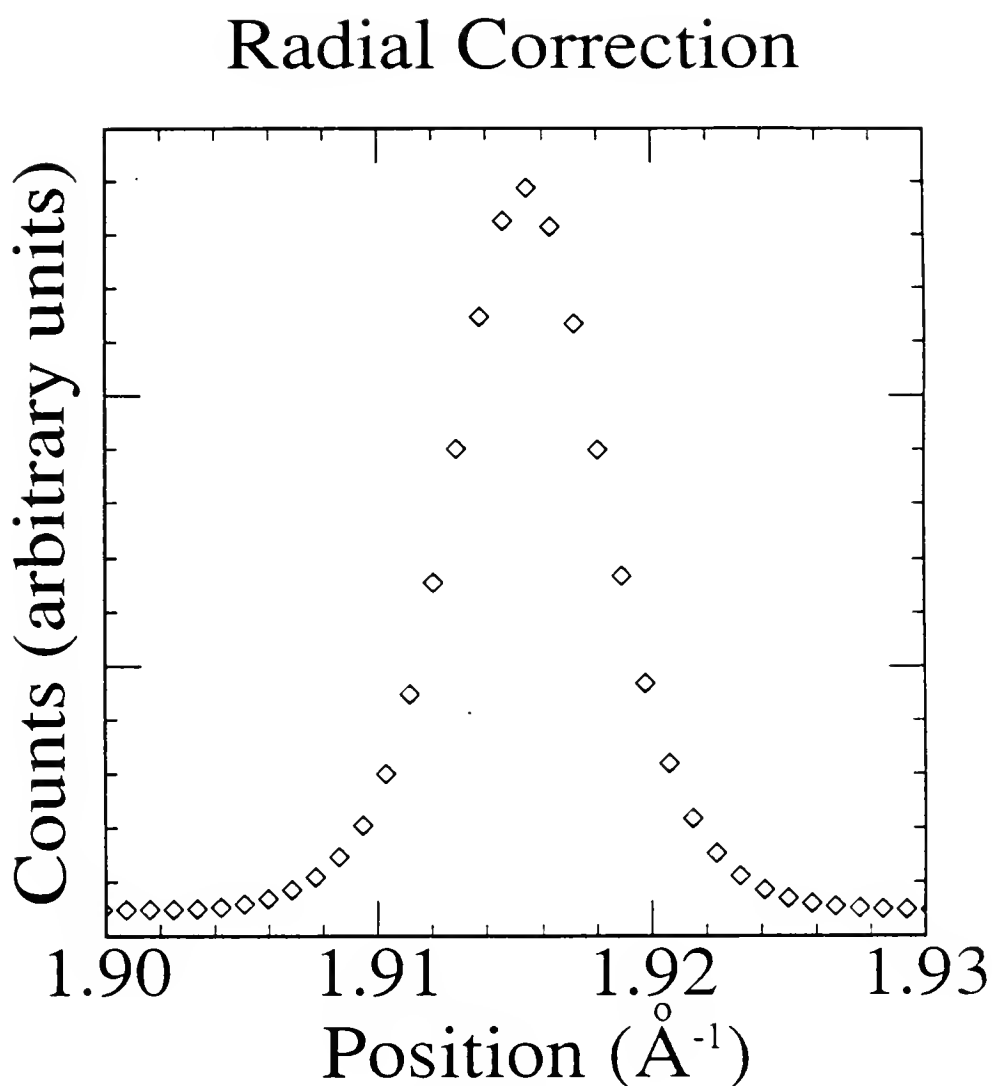


FIG. 14. Convolution of the instrumental resolution (fig. 11.) with a gaussian of width 0.001 \AA^{-1} ($.002 \text{ \AA}^{-1}$ FWHM) (representing finite size and strain. The convolution represents the correction in the radial data.

Transverse Resolution Correction

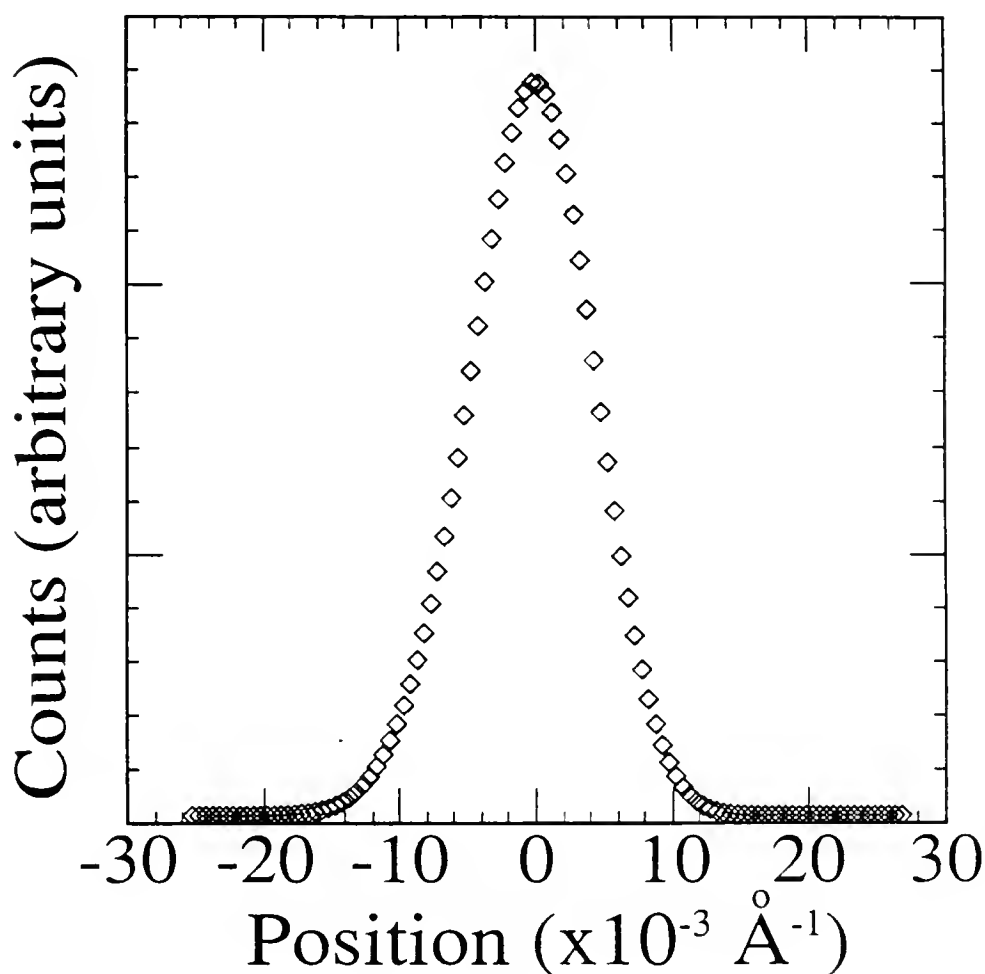


FIG. 15. Convolution of the instrumental resolution (fig. 12.), mosaic spread (fig. 13.), and a gaussian of width 0.001 \AA^{-1} ($.002 \text{ \AA}^{-1}$ FWHM) representing finite size and strain. The convolution represents the correction in the transverse direction.

theoretical and fundamental functions. Another method for seeing changes in line shape is to scale peaks from different times by their amplitude and width. In such scaling plots, differences in shape are apparent. However, they do not define or systematize the change as do the fits.

The fits to the data are used to extract a reciprocal space line width which is inversely proportional to an ordered domain size $L(t)$. $L(t)$ is compared to various functional forms, specifically a power law (equation 2.5) and/or a logarithmic law (equation—2.12). The fits also provide an amplitude and integrated intensity (width multiplied by the amplitude) as functions of time and temperature. Scaling the intensity and time gives information relating to changes, or lack thereof, in the mechanisms for growth.

Results from the Bulk Data:

The shape of our peak at early times (first half hour) is gaussian (GS). During this time the superlattice peak arises from isolated ordered clusters embedded in a disordered matrix. A GS shape at early times is not surprising, after all it is associated with finite size broadening. At later times the line shape crosses over to a Lorentzian—squared (LSQ) form. The LSQ shape is characteristic of the coarsening process, and results from a random distribution of ordered domains separated by sharp domain walls.⁽⁹⁶⁾ Figure 16 compares the shape of the peak at early and late times.

The simplest model for superlattice peak line shapes in Cu_3Au is a Hendrichs—Teller⁽¹⁰⁵⁾ (HT) approach, which assumes independent domain walls as discussed in chapter 3 section D. The predicted scattering function⁽⁸⁾ in this approximation is an anisotropic lorentzian in the small q limit. The function

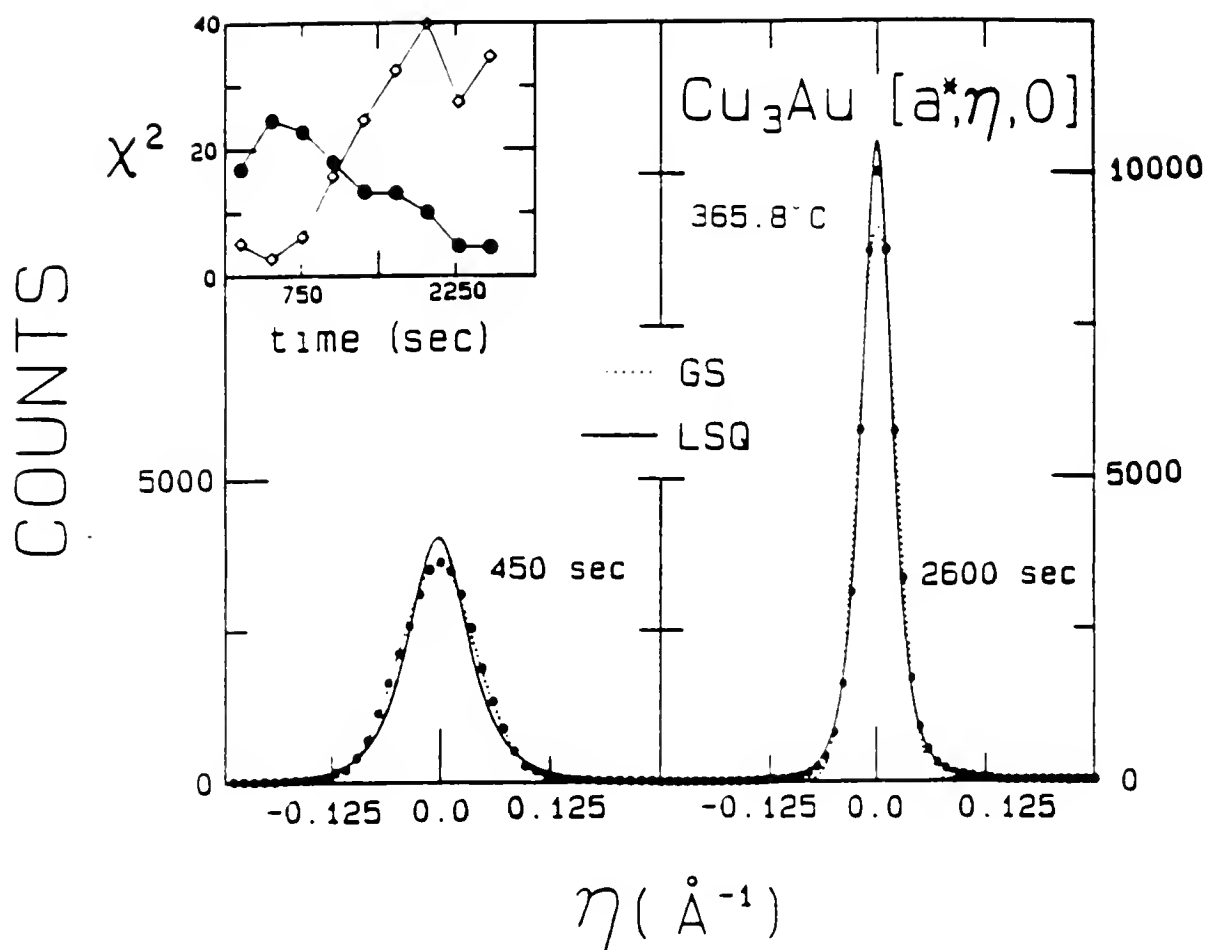


Fig. 16. Change in the line shape after a quench. Transverse scans of the $[0,1,0]$ with $a^* = 1.666 \text{\AA}^{-1}$. Solid (dotted) line is a GS (LSQ) least-squares fit. The FWHM of the instrumental resolution is equal to the width of the tic marks on the η axis.

Inset: χ^2 (as later defined) of the fit vs. time for the GS(diamonds) and LSQ(circles).

definition is presented in appendix B. This HT approach, was used by Ludwig et al⁽⁸⁾ to parameterize early-time kinetic experiments on Cu_3Au . The small q limit is a modified Lorentzian where the line width depends on the direction in k -space. Although this approach effectively parameterized their data it would not do so here. However, this is not a contradiction because all of their scans were taken in the time it took to take our first scan, the resolution they used was very broad compared to the present work, and their sample was a poly-crystalline wire. The modified Lorentzian produced poorer fits to our data than a straight Lorentzian which did not fit well at any time. However, if the shape was convolved with the resolution function the fits were poor but acceptable. It is worth noting that the background for these fits was constrained to be positive, if negative backgrounds were permitted considerably better fits were found in the transverse scans which contained considerably few points in the tails.

Several theoretical predictions on coarsening suggest^(35,39) that the tails of $S(q,t)$ should decay as q^{-4} , consistent with a LSQ peak. The theory of Ohta, Jasnow, and Kawasaki⁽³⁵⁾ (OJK) derives an equation for the line shape that involves an integration for each q . Using numerical integration non-convolution fits to this line shape have been done on selected peaks from quenches to various temperatures and times such that the resolution is small compared to the overall width. However, the resulting fits during coarsening were significantly worse than the LSQ fits for the transverse scans but only slightly worse for the radial scans. Definitions for this theory and the one that follow are summarized in appendix B.

Recently Z. W. Lai has developed a coarse-grained model of the phase transition kinetics for a Cu_3Au type system⁽⁹²⁾. The model is based on a Ginzburg-Landau hamiltonian with the symmetry of Cu_3Au . This model exhibits distinct regimes from early to late time. Moreover, the line shape of the structure

factor starts off gaussian and then crosses over to approximately lorentzian—squared in agreement with our observations especially in the transverse direction. At late times this model produces a modified lorentzian squared of the form,

$$F_1(k) = \frac{1}{(1+b_1k^2)^2+2b_2k^2} \quad (4.1)$$

Fits of this form to our data do not favor this form over that of a pure lorentzian—squared (the $b=0$ case). However, Z. Lai points out that this variance could be due to the size and time used in the computations for this model. Moreover, due to the need for a larger system, and hence, more computer time a smaller anisotropy in the shape of the domains was used in the numerical calculations than is found in Cu_3Au . Z. Lai also suggested that this model might not be "completely settled into the longest time asymptotic regime". Recalling that during the crossover there is a period where the peak is neither gaussian or lorentzian—squared, our fits were checked to see if b_2 could be related to the crossover. However, there was no evidence of b_2 contributing in any systematic way. In fact even at the crossover this modification has very little effect on the shape of the fits. Nevertheless this model exhibits the qualitative behavior that we have observed.

In table 1 are listed the reduced chi—squared (χ^2) values for non—convolution and some resolution convolution fits to gaussian, lorentzian, lorentzian—squared, lorentzian to a variable power, and the two shapes based on the discussed theories (see appendix B for functional definitions). In the fits, up to a second order polynomial background $[a(x-x_0)^2+b(x-x_0)+c]$ was added to the model function. Chi—squared is the goodness of fit parameter used in the fitting routine $[\chi^2 = \Sigma(I_{\text{fit}} - I_{\text{meas}})^2 / (\text{degrees of freedom})]$ All but the latest times given in table 1 are such that the resolution width is small compared to the over all width. Therefore, the resolution is not important for the first four times listed in table 1.

Table 1.
Chi-squared values for selected scans as a
function of time after a quench on the bulk Cu₃Au sample. Tables are
arranged by decreasing quench temperature and direction in reciprocal space.

Transverse		T=382°C					[$\chi^2=\Sigma(I_{\text{fit}}-I_{\text{meas.}})^2/(n_{\text{pnt}}-n_{\text{par}})$]				
line shape	order of bg	(non convolution fits)									
		8 minutes	23 minutes	48 minutes	123 minutes	493 minutes					
Gaussian	0		2.5	16.2	72.3	24.8	48.3				
	1		2.0	16.3	73.8	25.0	49.2				
	2		1.5	11.1	56.8	22.0	34.8				
Lorent- zian	0		8.3	135.6	229.5	48.8	82.6				
	1		8.3	138.1	234.4	48.4	84.1				
	2		8.2	122.2	188.3	41.3	70.2				
LSQ	0		2.9	9.2	2.2	2.6	6.6				
	1		2.5	9.3	2.3	2.5	6.7				
	2		2.1	7.0	2.2	2.4	4.3				
Lor. to m (m) chi	0	(4.6)	2.5	(3.3)	1.9	(2.1)	2.0	(1.8)	1.9	(1.8)	5.4
	1	(4.8)	2.2	(3.3)	1.8	(2.1)	2.0	(1.8)	1.8	(1.8)	5.5
	2	(6.2)	2.2	(3.6)	1.6	(2.1)	2.0	(1.7)	1.8	(2.0)	4.2
HT ⁽⁸⁾ Theory	0		10.0	151.8	264.8	67.4	85.1				
	1		10.1	155.1	244.4	64.4	86.7				
	2		9.8	131.2	189.0	62.1	71.4				
O.J.K. ⁽³⁵⁾ Theory	0		2.8	31.4	77.9	17.0	119.4				
	1		2.5	32.0	79.9	17.0	331.2				
	2		2.3	29.7	76.3	14.8	90.5				
(convolution fits)											
Gaussian	0		2.7	16.9	75.5	25.9	50.7				
	1		2.1	16.6	75.4	25.5	50.6				
	2		1.5	11.1	56.8	22.0	35.1				
Lorent- zian	0		8.5	134.6	217.9	42.3	65.7				
	1		7.9	134.1	217.8	41.0	65.3				
	2		8.0	115.3	167.7	33.2	18.4				
LSQ	0		2.8	8.2	2.0	3.4	11.5				
	1		2.5	8.3	2.0	3.3	11.7				
	2		2.1	7.4	2.0	3.0	6.5				
Lor. to m (m) chi	0	(4.6)	1.9	(3.2)	1.9	(2.0)	1.9	(1.6)	1.5	(1.3)	1.7
	1	(4.8)	1.4	(3.2)	1.8	(2.0)	1.9	(1.6)	1.4	(1.3)	1.7
	2	(9.0)	1.4	(3.5)	1.7	(2.0)	1.9	(1.6)	1.4	(1.4)	1.6
HT Theory	0		8.7	136.5	213.0	41.8	43.9				
	1		8.3	139.5	214.6	43.0	44.8				
	2		8.4	118.1	172.8	29.8	28.4				

Table 1. (cont.)
Values of chi-squared

Transverse (non convolution fits)		T=375.6°C				
line shape	order of bg	8 minutes	23 minutes	48 minutes	123 minutes	494 minutes
Gaussian	0	3.9	31.0	81.8	133.7	55.6
	1	3.5	30.8	83.0	136.0	56.8
	2	2.2	24.5	64.3	117.8	42.0
Lorent- zian	0	101.8	191.9	283.4	325.4	93.3
	1	102.6	194.8	288.6	332.0	95.2
	2	92.0	174.2	245.4	307.7	79.2
LSQ	0	21.3	8.3	5.1	11.7	7.6
	1	21.6	8.3	5.1	11.8	7.7
	2	16.3	6.4	5.2	11.1	4.8
Lor.to(m) (m) chi	0	(18.5) 5.8	(2.7) 3.3	(2.1) 4.7	(1.9) 10.4	(1.7) 5.6
	1	(14.5) 5.6	(2.8) 3.1	(2.1) 4.7	(1.9) 10.4	(1.7) 5.7
	2	(93.4) 4.5	(2.8) 3.2	(2.2) 4.6	(1.9) 10.4	(1.9) 4.5
HT Theory	0	155.0	200.4	295.5	342.3	133.2
	1	138.0	207.8	300.3	349.7	121.1
	2	100.1	174.9	239.2	307.7	95.5
O.J.K. Theory	0	5.3	19.3	101.7	92.5	39.1
	1	5.1	19.2	104.1	94.2	40.8
	2	5.0	16.9	38.6	80.4	28.1

(convolution fits)

Gaussian	0	4.1	32.4	85.5	139.9	58.6
	1	3.5	31.5	84.9	139.2	58.5
	2	2.2	24.5	64.3	118.0	42.4
Lorent- zian	0	103.5	186.9	260.4	273.4	24.7
	1	102.1	185.9	259.4	272.9	24.7
	2	89.1	161.1	210.9	187.9	16.7
LSQ	0	20.5	6.9	4.0	14.3	15.1
	1	20.8	6.9	4.0	14.4	15.4
	2	20.7	5.9	4.0	12.4	9.4
Lor.to(m) (m) chi	0	(20.3) 3.7	(2.6) 2.8	(2.0) 3.9	(1.6) 6.7	(1.3) 1.5
	1	(23.4) 3.3	(2.7) 2.5	(2.0) 3.9	(1.6) 6.7	(1.3) 1.6
	2	(139.6) 2.2	(2.7) 2.6	(2.0) 3.9	(1.6) 6.8	(1.3) 1.6
O.J.K. Theory	0	111.1	207.9	314.0	265.9	23.1
	1	127.0	212.4	317.9	271.7	23.4
	2	90.8	159.3	190.4	182.1	20.1

Table 1. (cont.)
Values of chi-squared

Transverse
(non convolution fits) $T=370.8^{\circ}\text{C}$

line shape	order of bg	8 minutes	23 minutes	48 minutes	123 minutes	494 minutes
Gaussian	0	3.5	29.8	47.9	24.9	55.0
	1	2.8	29.4	45.1	24.9	56.2
	2	2.1	22.2	31.5	22.0	41.7
Lorent- zian	0	127.6	224.7	199.5	85.6	122.7
	1	128.4	227.2	190.1	85.0	125.1
	2	114.4	204.0	159.4	76.8	107.2
LSQ	0	25.8	10.9	5.3	3.3	7.7
	1	26.1	11.0	4.7	3.1	7.8
	2	17.9	8.5	4.8	3.0	5.8
Lor.to(m) (m) chi	0	(19.3) 6.5	(2.9) 3.8	(2.2) 4.8	(2.0) 3.2	(1.8) 6.9
	1	(15.1) 6.2	(3.0) 3.4	(2.2) 3.9	(2.0) 3.0	(1.8) 7.1
	2	(59.7) 5.6	(3.1) 3.3	(2.5) 3.0	(2.0) 2.9	(2.0) 5.6
O.J.K. Theory	0	145.7	279.4	208.9	93.7	161.1
	1	132.9	257.7	203.8	92.0	158.6
	2	126.6	213.2	169.4	81.6	119.2
HT Theory	0	6.9	19.9	27.0	17.3	38.4
	1	6.7	20.2	24.9	17.3	40.2
	2	6.4	17.1	17.8	14.6	26.8

(convolution fits)

Gaussian	0	3.7	31.2	50.0	26.0	57.9
	1	2.9	30.0	46.1	25.5	57.9
	2	2.1	22.2	31.6	22.1	42.2
Lorent- zian	0	130.1	219.5	184.7	73.9	37.1
	1	128.1	217.1	170.5	71.4	37.0
	2	111.1	189.2	136.0	48.4	25.9
LSQ	0	24.9	9.1	4.2	3.2	13.2
	1	25.3	9.2	3.5	3.0	13.4
	2	25.8	8.3	3.4	2.7	8.3
Lor.to(m) (m) chi	0	(23.7) 3.3	(2.8) 2.5	(2.0) 4.1	(1.7) 2.3	(1.4) 2.5
	1	(28.4) 2.6	(2.8) 2.1	(2.1) 3.3	(1.7) 2.1	(1.3) 2.5
	2	(209.4) 2.1	(3.0) 2.0	(2.3) 2.6	(1.7) 2.1	(1.4) 2.5
HT Theory	0	143.9	216.3	209.3	58.9	34.8
	1	129.5	218.1	163.6	57.5	35.6
	2	125.5	196.2	127.5	51.8	29.9

Table 1. (cont.)
Values of chi-squared

Transverse (non convolution fits)		T=365.8°C				
line shape	order of bg	8 minutes	23 minutes	48 minutes	123 minutes	514 minutes
Gaussian	0	2.8	24.6	35.7	25.6	60.5
	1	2.4	24.2	36.2	25.4	61.2
	2	1.8	17.2	26.8	23.0	40.2
Lorentz- zian	0	129.3	217.1	187.9	97.3	142.0
	1	131.0	219.8	191.6	96.9	143.2
	2	112.6	197.7	68.2	88.6	118.3
LSQ	0	24.6	13.3	5.3	3.0	8.5
	1	25.1	13.5	5.4	2.9	8.5
	2	16.4	10.7	5.2	2.9	6.8
Lor.to(m) (m) chi	0	(20.0) 5.5	(3.2) 4.8	(2.4) 3.1	(2.0) 3.0	(1.9) 8.3
	1	(14.7) 5.5	(3.2) 4.6	(2.5) 3.1	(2.0) 2.8	(1.9) 8.3
	2	(66.8) 5.0	(3.5) 4.2	(2.7) 2.7	(2.0) 2.9	(2.2) 6.2
HT Theory	0	172.6	235.6	207.9	116.3	158.9
	1	161.6	236.8	212.7	103.5	168.6
	2	123.0	193.8	163.7	94.1	120.6
O.J.K. Theory	0	5.9	19.0	19.3	18.1	42.6
	1	5.9	19.6	19.8	17.7	43.1
	2	5.6	16.3	15.1	15.2	27.9

(convolution fits)

Gaussian	0	2.9	25.7	37.3	26.8	62.9
	1	2.5	24.7	37.0	26.0	62.8
	2	1.8	17.2	26.8	23.1	41.1
Lorentz- zian	0	132.1	213.2	174.8	84.6	45.5
	1	130.9	211.2	174.3	81.9	45.0
	2	109.5	184.4	147.3	71.1	27.7
LSQ	0	24.1	11.5	3.5	2.9	13.0
	1	24.5	11.6	3.6	2.7	13.1
	2	25.7	10.7	3.6	2.7	7.0
Lor.to(m) (m) chi	0	(24.1) 2.6	(3.0) 2.8	(2.3) 2.3	(1.8) 2.3	(1.4) 3.0
	1	(27.4) 2.3	(3.1) 2.4	(2.3) 2.3	(1.8) 2.2	(1.4) 2.9
	2	(89.0) 1.8	(3.4) 2.1	(2.5) 2.0	(1.8) 2.2	(1.4) 2.8
HT Theory	0	148.1	222.7	193.9	110.7	40.2
	1	142.5	221.6	198.3	81.4	40.6
	2	109.7	178.0	148.8	61.3	29.2

Table 1. (cont.)
Values of chi-squared

Radial (non convolution fits)		T=382.0°C				
line shape	order of bg	8 minutes	22 minutes	47 minutes	123 minutes	485 minutes
Gaussian	0	1.2	2.5	13.3	38.6	23.0
	1	1.2	2.5	13.4	38.7	23.1
	2	1.2	1.3	6.5	23.7	16.6
Lorent- zian	0	1.2	2.4	23.0	103.1	87.9
	1	1.2	2.4	23.1	103.7	88.4
	2	1.2	1.3	11.7	63.5	62.4
LSQ	0	1.2	1.0	2.3	6.3	6.4
	1	1.2	1.0	2.3	6.3	6.5
	2	1.2	1.0	2.3	6.4	6.5
Lor.to(m) (m) chi	0	(1.1)	(2.4)	0.9 (2.4)	1.7 (2.4)	3.9 (2.5)
	1	(1.4)	(2.4)	0.9 (2.4)	1.7 (2.4)	3.9 (2.5)
	2	(1.0)	(2.9)	0.9 (3.0)	1.3 (2.8)	2.2 (2.9)
HT Theory	0	8.7	3.4	43.3	178.5	138.8
	1	8.6	3.4	45.2	168.3	139.8
	2	2.5	3.2	34.1	149.2	122.8
O.J.K	0	1.6	3.1	7.6	19.2	11.4

(convolution fits)

Gaussian	0	1.2	2.5	11.9	28.9	13.3
	1	1.2	2.5	11.9	28.7	13.3
	2	1.2	1.3	5.6	17.1	9.4
Lorent- zian	0	1.2	2.4	20.0	38.4	8.8
	1	1.2	2.4	20.0	38.2	8.8
	2	1.2	2.3	16.7	36.5	8.8
LSQ	0	1.2	0.9	1.4	2.8	4.5
	1	1.2	0.9	1.4	2.7	4.6
	2	1.2	0.9	1.3	1.4	3.1
Lor.to(m) (m) chi	0	(1.0)	(2.2)	0.9 (2.0)	1.4 (1.7)	1.9 (1.4)
	1	(1.3)	(2.2)	0.9 (2.0)	1.4 (1.7)	1.8 (1.4)
	2	(1.0)	(2.6)	0.9 (2.4)	1.2 (1.9)	1.3 (1.5)
HT Theory	0	6.6	3.1	31.8	133.6	208.9
	1	5.3	3.1	31.6	132.7	208.9
	2	1.6	2.6	19.8	79.0	66.3
O.J.K.	0					9.3

Table 1. (cont.)
Values of chi-squared

Radial (non convolution fits)		T=375.6°C				
line shape	order of bg	8 minutes	23 minutes	49 minutes	126 minutes	491 minutes
Gaussian	0	1.9	8.1	20.3	42.8	50.1
	1	1.8	8.1	20.3	43.0	50.4
	2	1.2	3.5	10.5	24.0	36.0
Lorent- zian	0	2.9	19.5	51.3	150.7	215.9
	1	2.9	19.6	51.6	151.7	217.4
	2	1.4	8.4	25.3	95.8	153.3
LSQ	0	1.4	3.3	4.5	11.4	15.1
	1	1.4	3.3	4.5	11.5	15.2
	2	1.2	2.8	4.2	11.5	15.3
Lor.to(m) (m) chi	0	(3.6) 1.1	(3.0) 1.7	(2.7) 2.2	(2.6) 5.5	(2.6) 7.9
	1	(3.7) 1.1	(3.0) 1.7	(2.7) 2.1	(2.6) 5.5	(2.6) 7.9
	2	(5.1) 1.1	(4.0) 1.4	(3.2) 1.5	(3.2) 2.2	(3.0) 4.7
HT Theory	0	9.0	48.7	112.8	244.2	347.2
	1	8.7	47.3	111.9	245.7	349.2
	2	4.4	31.2	79.2	209.3	279.8
O.J.K.	0	2.4	4.0	10.2	19.2	26.0

(convolution fits)

Gaussian	0	1.9	7.5	17.4	31.1	27.5
	1	1.8	7.5	17.3	31.1	27.4
	2	1.2	4.7	16.4	63.4	149.8
Lorent- zian	0	7.2	31.2	51.8	129.6	21.6
	1	7.0	31.0	51.6	129.4	21.6
	2	3.8	21.1	38.9	58.5	33.5
LSQ	0	1.3	2.3	1.8	3.0	7.4
	1	1.3	2.3	1.8	3.0	7.4
	2	1.2	2.1	1.8	1.6	4.4
Lor.to(m) (m) chi	0	(3.4) 1.1	(2.7) 1.7	(2.2) 1.7	(1.9) 2.8	(1.5) 3.4
	1	(3.4) 1.1	(2.7) 1.6	(2.2) 1.6	(1.9) 2.8	(1.5) 3.4
	2	(4.7) 1.1	(3.5) 1.4	(2.5) 1.3	(2.2) 1.3	(1.6) 3.0
HT Theory	0	7.2	30.7	61.0	149.9	463.8
	1	6.9	30.4	59.3	150.7	466.8
	2	4.0	22.2	47.2	80.3	270.6
O.J.K.	0					20.9

Table 1. (cont.)
Values of chi-squared

Radial (non convolution fits)		T=370.8°C				
line shape	order of bg	8 minutes	23 minutes	49 minutes	126 minutes	487 minutes
Gaussian	0	1.9	8.8	19.4	49.1	51.7
	1	1.9	8.7	19.5	49.4	52.0
	2	1.0	3.1	9.1	28.7	37.2
Lorent- zian	0	3.6	23.6	65.4	170.0	237.7
	1	3.7	23.7	65.8	171.1	239.3
	2	1.5	8.9	30.5	100.3	164.9
LSQ	0	1.5	3.8	7.5	12.6	17.3
	1	1.5	3.8	7.6	12.6	17.4
	2	1.1	2.8	6.3	12.4	17.4
Lor.to(m)	0	(3.9)	(3.2)	(3.0)	(2.7)	(2.7)
(m) chi	1	(4.0)	(3.2)	(3.0)	(2.7)	(2.7)
	2	(8.9)	(4.5)	(3.8)	(3.2)	(3.1)
HT	0	17.0	69.7	144.6	317.3	362.8
Theory	1	16.6	68.4	152.1	320.2	366.5
	2	6.3	40.2	101.6	249.2	304.8
O.J.K.	0	2.5	4.0	8.9	21.7	22.7

(convolution fits)

Gaussian	0	1.9	8.3	16.9	37.0	29.3
	1	1.9	8.1	16.8	37.0	29.3
	2	1.0	4.2	14.7	20.6	20.4
Lorent- zian	0	14.0	47.3	81.2	101.5	68.7
	1	14.0	47.0	81.1	101.4	68.7
	2	5.5	28.9	58.7	87.2	41.4
LSQ	0	1.4	2.6	3.5	2.8	5.6
	1	1.4	2.6	3.5	2.8	5.6
	2	1.4	2.4	3.3	2.1	3.4
Lor.to(m)	0	(3.7)	(2.9)	(2.5)	(2.0)	(1.6)
(m) chi	1	(3.7)	(2.9)	(2.5)	(2.0)	(1.6)
	2	(8.4)	(4.0)	(3.2)	(2.3)	(1.7)
HT	0	13.8	47.0	88.7	165.3	442.7
Theory	1	13.6	46.8	86.3	165.5	449.2
	2	5.7	29.5	66.0	109.5	64.3
O.J.K.	0					17.1

Table 1. (cont.)
Values of chi-squared

Radial
(non convolution fits) $T=365.8^{\circ}\text{C}$

line shape	order of bg	16 minutes	27 minutes	52 minutes	128 minutes	496 minutes
Gaussian	0	5.0	10.5	24.1	51.6	55.0
	1	4.9	10.5	24.3	51.9	55.4
	2	1.8	3.8	10.9	29.7	37.9
Lorent- zian	0	12.2	26.4	67.4	170.0	237.7
	1	12.2	26.6	67.9	171.2	239.3
	2	3.6	9.6	31.1	96.1	161.9
LSQ	0	2.6	4.1	7.5	12.6	16.3
	1	2.5	4.1	7.6	12.7	16.5
	2	1.6	3.0	6.5	12.2	16.5
Lor.to(m) (m) chi	0	(3.5) 1.1	(3.2) 1.6	(2.9) 3.0	(2.7) 5.3	(2.7) 7.7
	1	(3.5) 1.0	(3.2) 1.5	(2.9) 3.0	(2.7) 5.3	(2.7) 7.8
	2	(4.6) 0.9	(4.2) 1.2	(3.6) 2.1	(3.2) 2.9	(3.0) 4.3
HT Theory	0	45.4	80.0	167.0	322.0	364.0
	1	43.3	79.9	168.1	323.1	366.5
	2	21.6	45.1	110.9	252.5	302.7
O.J.K	0	3.7	5.1	11.7	23.2	23.9

(convolution fits)

Gaussian	0	4.8	9.9	21.4	40.2	32.7
	1	4.7	9.8	21.4	40.1	32.7
	2	1.7	3.5	9.3	22.2	21.5
Lorent- zian	0	32.8	55.0	97.2	115.8	42.1
	1	32.4	54.7	97.1	115.7	42.1
	2	17.1	32.8	64.9	93.5	42.1
LSQ	0	2.0	2.8	3.8	3.0	5.2
	1	2.0	2.8	3.8	3.0	5.2
	2	1.9	2.6	3.7	2.6	2.7
Lor.to(m) (m) chi	0	(3.2) 1.0	(2.8) 1.5	(2.5) 2.5	(2.0) 3.0	(1.6) 2.8
	1	(3.2) 0.9	(2.8) 1.4	(2.5) 2.6	(2.0) 2.9	(1.6) 2.8
	2	(4.2) 0.9	(3.8) 1.2	(3.0) 1.9	(2.3) 1.8	(1.8) 2.1
HT Theory	0	32.7	54.5	100.1	171.5	425.4
	1	32.1	54.4	100.8	172.6	428.3
	2	17.4	34.1	72.7	157.4	62.9
O.J.K.	0					20.1

One would expect for late times the convolution of the resolution function with a LSQ would fit better than a straight LSQ, as is the case in the radial data.

However, this is so for the transverse data, implying that the uncertainty in the transverse resolution function is too great to adequately define its shape, which is the case due to the uncertainty in the shape of the mosaic.

The difference in the chi squared values between the LSQ and lorentzian to the m^{th} power during coarsening is never so great as to make one believe that the peak is not a LSQ shape. In fact, the dependence of chi squared on m is relatively flat between about 1.3 to over 3 but rises quickly near 1.0.

Fits to the convolution of the resolution function and the first theoretically based shape discussed have not been done in the transverse direction. It is unlikely that such a fit would be an improvement over the non-convolution fit, because this shape is similar to a LSQ in the tails and the convolution fitting with a LSQ function did not improve the fits in the transverse direction. However, despite the computer time needed for such a convolution fit a few have been done for the radial data. Improvement in the chi squared values in the convolution fits relative to the non-convolution fits for this first theoretical shape were similar to what was found in the LSQ shape. The chi squared values for the LSQ function at late times are approximately half those of the OJK theory. Keeping in mind that the justification for assuming a LSQ peak has always been that the tails decay as q^{-4} as OJK theory predicts, it is some what surprising that a LSQ shape actually fits better than the full theory. However, several approximations were made in the theory that may explain this. The theory assumes an isotropic system, and a gaussian distribution of fluctuations of the domain wall positions. The authors point out the dependence of their results on the choice of this distribution.⁽³⁵⁾

Another way to see the change in the line shape, and hence, $S(q,t)$ is to scale the peaks. If the peaks were the same shape, plots of counts divided by the fitted amplitude vs. position divided by the width, would lie on the same curve. Figure 17 shows some of the raw data for the transverse 365.8°C quench with LSQ fits to all but the earliest one which is fit to a GS. Figure 18 shows the data after being scaled, the two lines are a scaled LSQ fit and a scaled GS fit. From the scaled data it is apparent that the earliest peak has a different shape than all the rest. This demonstrates that $S(q,t)$ can not be scaled from the coarsening regime to the growth regime, but does scale during coarsening. Moreover, $S(q,t)$ should not scale in this way during growth when the ratio of the volume of the sample in one of the ordered phases to the volume in a disordered phase is constantly changing. In order for scaling to be valid the physical picture after rescaling must be identical to an earlier time. This is not the case during the growth stage, if the length scale is reduced during growth the percentage of the sample that is in a disordered state will be greater than it was at all earlier times.

The crossover in the line shape has been observed in over a dozen quenches. Most of these quenches were to 375°C ($T_c - 10^\circ\text{C}$). In one quench to 378°C ($T_c - 7^\circ\text{C}$) the crossover is present, however, the greatest difference in their respective chi-squared values while the peak favored a GS line shape was 1.37 to 2.21 where for deeper quenches ratios of 1 to 9 were found. Moreover, in the 382.0°C quench the first peak mildly favored a GS line shape with chi-squared values of 1.9 and 2.2 for GS and LSQ fits respectively. In the deeper quenches to below 376°C where the crossover is pronounced the peak does not fit well to either a GS or LSQ shape at the point the chi-squared values for the GS and LSQ fits cross. In fact, the peak starts off GS and then continuously changes until it is LSQ, but during the change

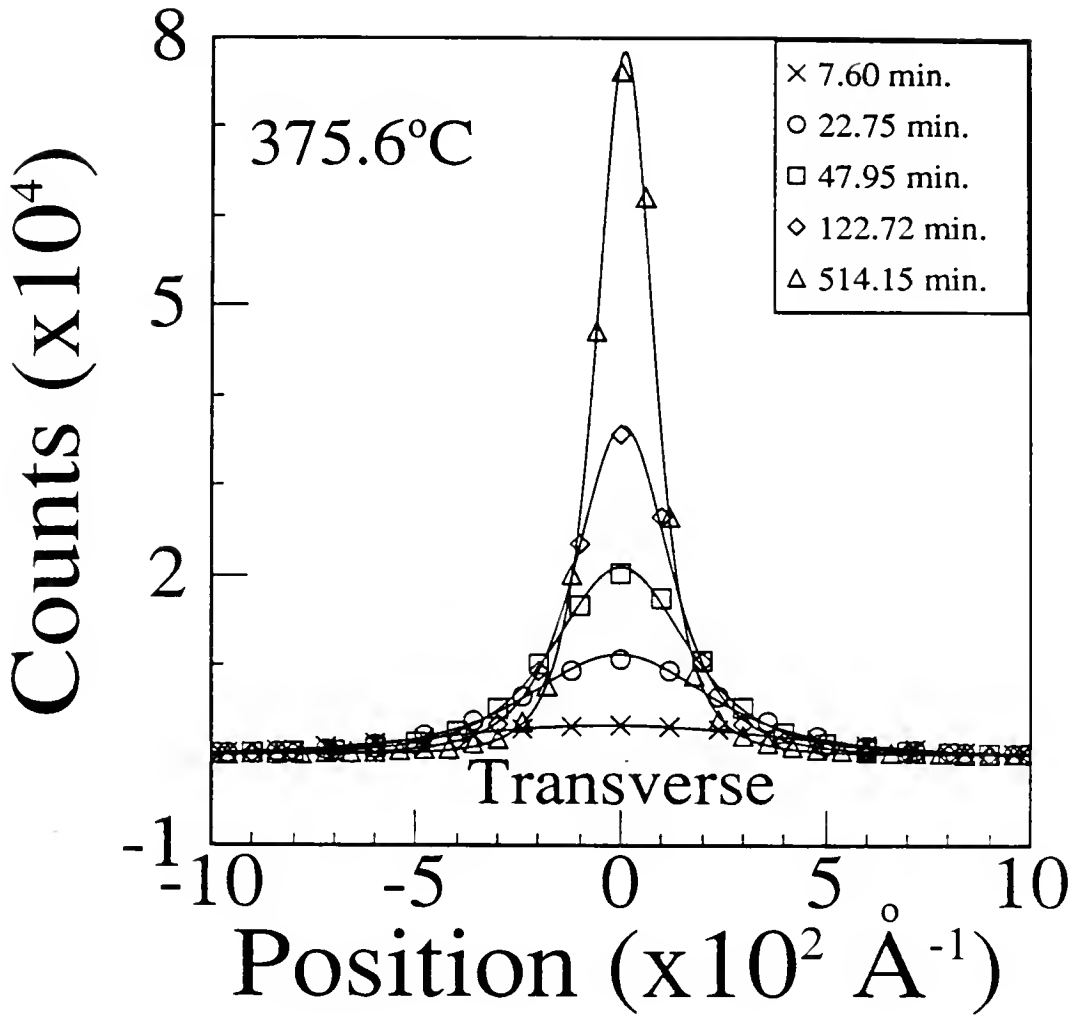


FIG. 17. Raw data on the $[0,1,0]$ bulk superlattice diffraction peak. Solid lines are fits to the data. For the 7.60 min. scan a gaussian fit is shown, the rest are lorentzian-squared fits.

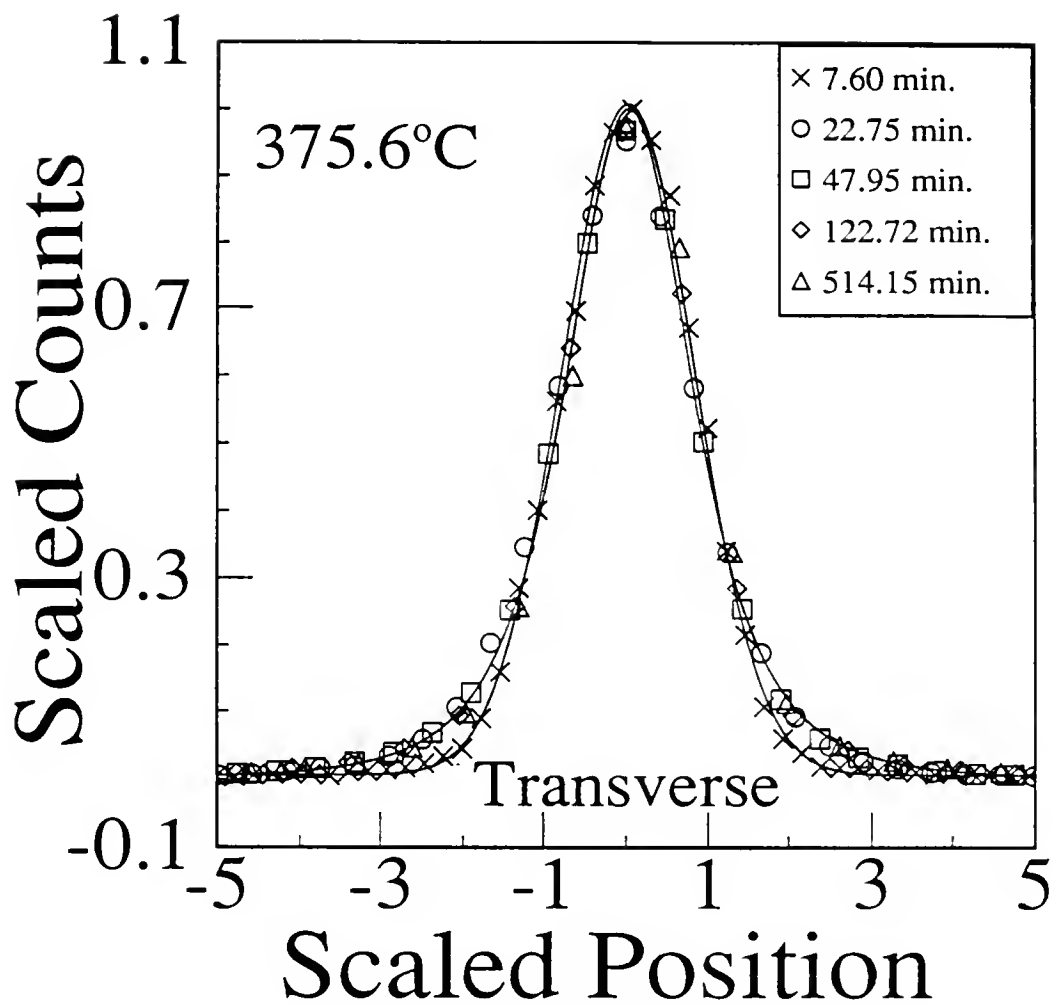


FIG. 18. Data shown in fig. 17 scaled by amplitude and width. The solid lines describe a gaussian and a lorentzian—squared shape. The 7.60 min. peak is gaussian, the rest are lorentzian—squared.

it is neither. The rate of change seems to be slower with lower temperature, in fact for quenches above 376°C it seems as if the change to LSQ was almost complete by the end of the first scan. In a typical quench 300 second scans were taken at the start of the experiment, attempts with shorter scanning times only made the effect less clear, due to the shape of the peak being statistically less well defined.

Moreover, for quenches close to T_c , the intensity of the peak is weaker than it is for deeper quenches, making it more difficult to see this change at higher temperatures for the same reason as above.

The change in line shape also occurred earlier with each quench. This suggests that the coarsening stage is reached sooner if the sample has been ordered for long times and disordered at temperatures within $(T_c + 40^{\circ}\text{C})$ prior to the quench. If the sample is heated to 700°C for 10 or more hours the change in line shape is again found to take place over the original longer time period. Coarsening being reached sooner suggest that nucleation and or growth is faster in samples that have not been annealed at high temperatures than in ones that have. This effect may involve the migration of vacancies to domain wall and grain boundaries during coarsening.

The change in line shape although present in the radial data is not as clear as in the transverse data. There are two reasons for this. The first is that the radial data was taken after the transverse data and the history dependence discussed above would lessen the effect. The second is that the width in the radial direction is narrower being due to only type 2 walls. Therefore, in the radial direction resolution is more important. Type 2 walls being farther apart may also have an effect on the peak shape.

Figure 19 displays the integrated intensities (fitted amplitude multiplied by fitted width) versus time after a thermal quench for the transverse directions at

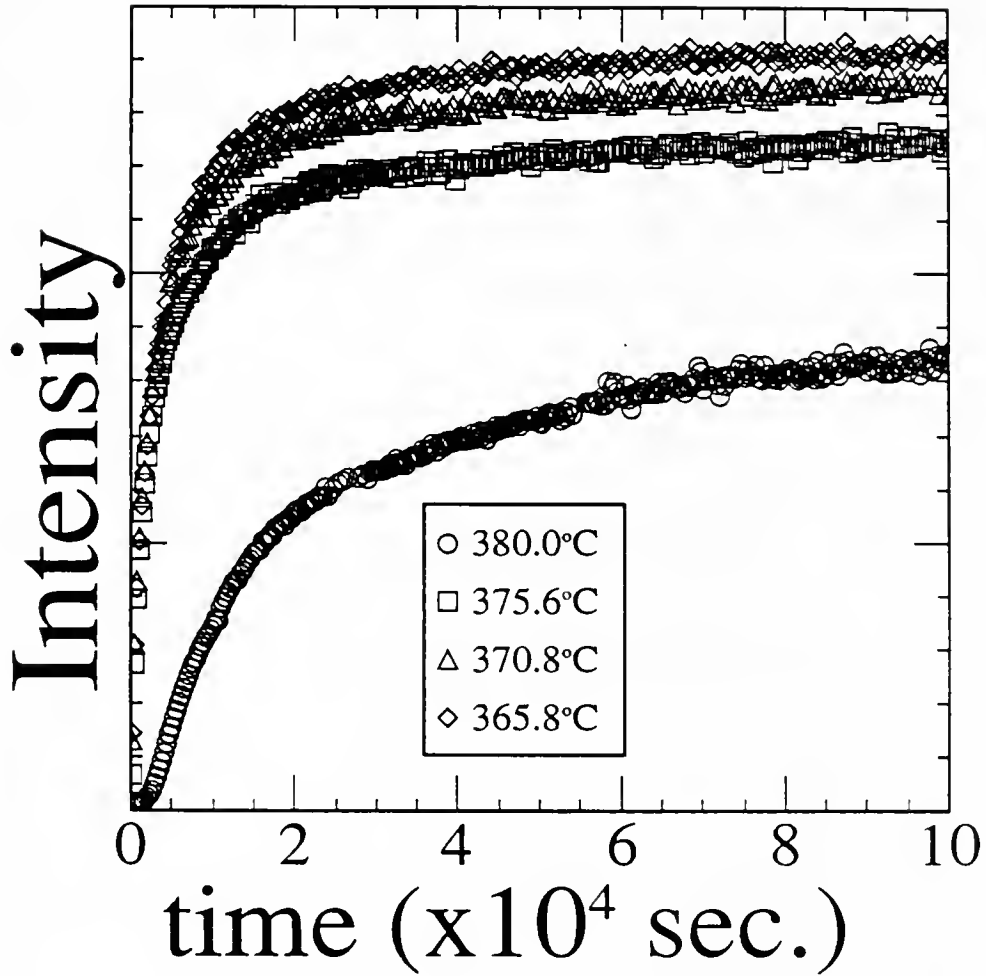


FIG. 19. Intensity (width of convolution fits multiplied by the amplitude of the fit) vs. time. The 380.0°C data shows a delay of approximately 1900 seconds that corresponds to a period of nucleation. The data shown was taken in the transverse direction at the $[0,1,0]$.

several temperatures. The 380.0°C transverse data shows a delay immediately after the quench, similar delays have also been observed in other quenches to temperatures closer to T_c . This delay is a result of an incubation time for nucleation. Such delays have been clearly observed in single grains of Mg_3In by Konishi and Noda⁽¹⁰⁶⁾. The delay time depends on the sample history which for the bulk sample is shown in figure 20. In light of the history dependence discussed above it is not too surprising that the deepest quench in which a delay is seen is the first one after etching and annealing at 700°C. After the delay a period of rapid growth in intensity is observed corresponding to the linear rise with time. At late times the intensity starts to saturate, asymptotically approaching some maximum ($I_\infty(T)$) that increases with decreasing temperature. The intensity after the delay fits well to

$$I(t) = I_\infty \left[1 - \exp \left[-[(t-t_0)/\tau] \right] \right]. \quad (4.2)$$

Figure 21 shows the data from 19 scaled by plotting I/I_∞ vs. t/b where b is the time for the intensity to reach $I_\infty/2$. As expected,⁽⁴³⁾ the data falls on a universal curve. In theory, one could use τ from the fits to equation 4.2, however, that proved to be less accurate. The reason for this is simply that the τ in the fits corresponds to a crossover time, which is early and our time resolution, being at best 1/2 the time to take a spectrum, is a sizable percentage of τ .

The delay seen in the integrated intensity is also in the amplitude. A plot of amplitude vs. time is shown in figure 22. The amplitude used in the plot is the convolution fitted amplitude and as such is corrected for resolution effects in the direction of the scan. The amplitude is proportional to the square of the order parameter and should scale as $L(t)^d$. Therefore, the amplitude should have a time dependence $t^{d/2}$. However, the data has only been corrected for resolution effects in one direction and the measurement approximately integrates over the other two

Sample History

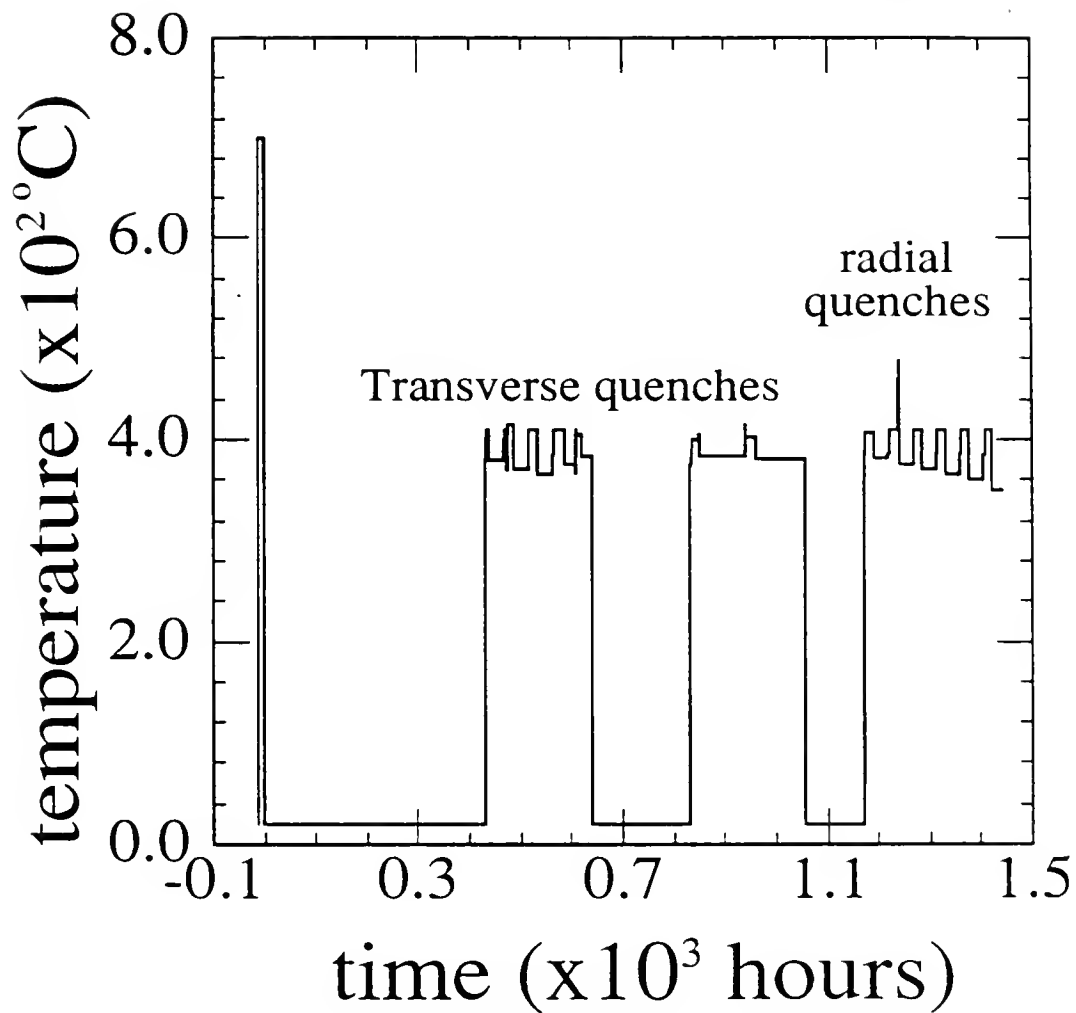


FIG. 20. Bulk Cu_3Au sample history starting from etching and annealing in an Ar atmosphere at 700°C to end of radial quenches. An etching and annealing followed by quenches similar to above was done prior to what is shown.

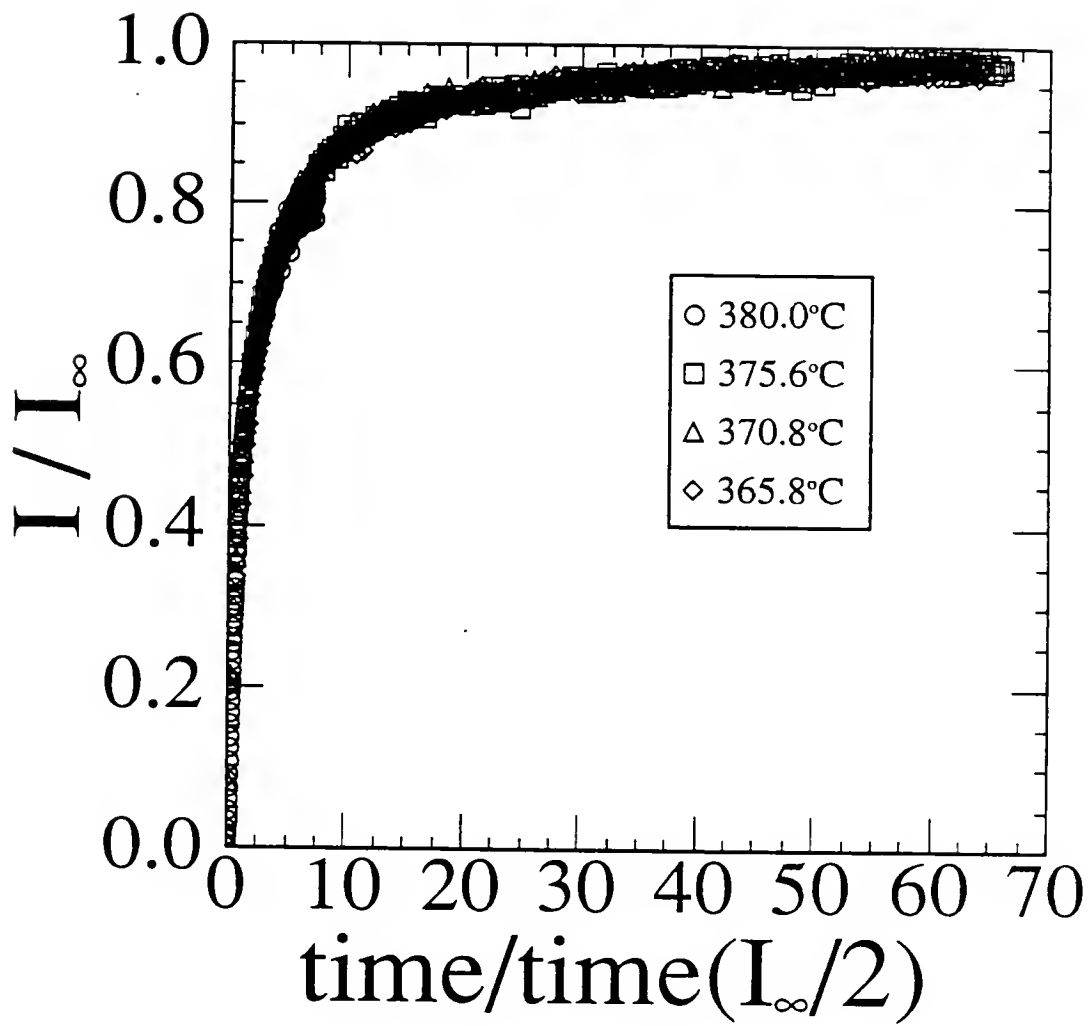


FIG. 21. Scaled intensity vs. scaled time. The nucleation period for the 380.0°C data was subtracted from the time before scaling. The unscaled data is shown in fig. 19.

Transverse Amplitude

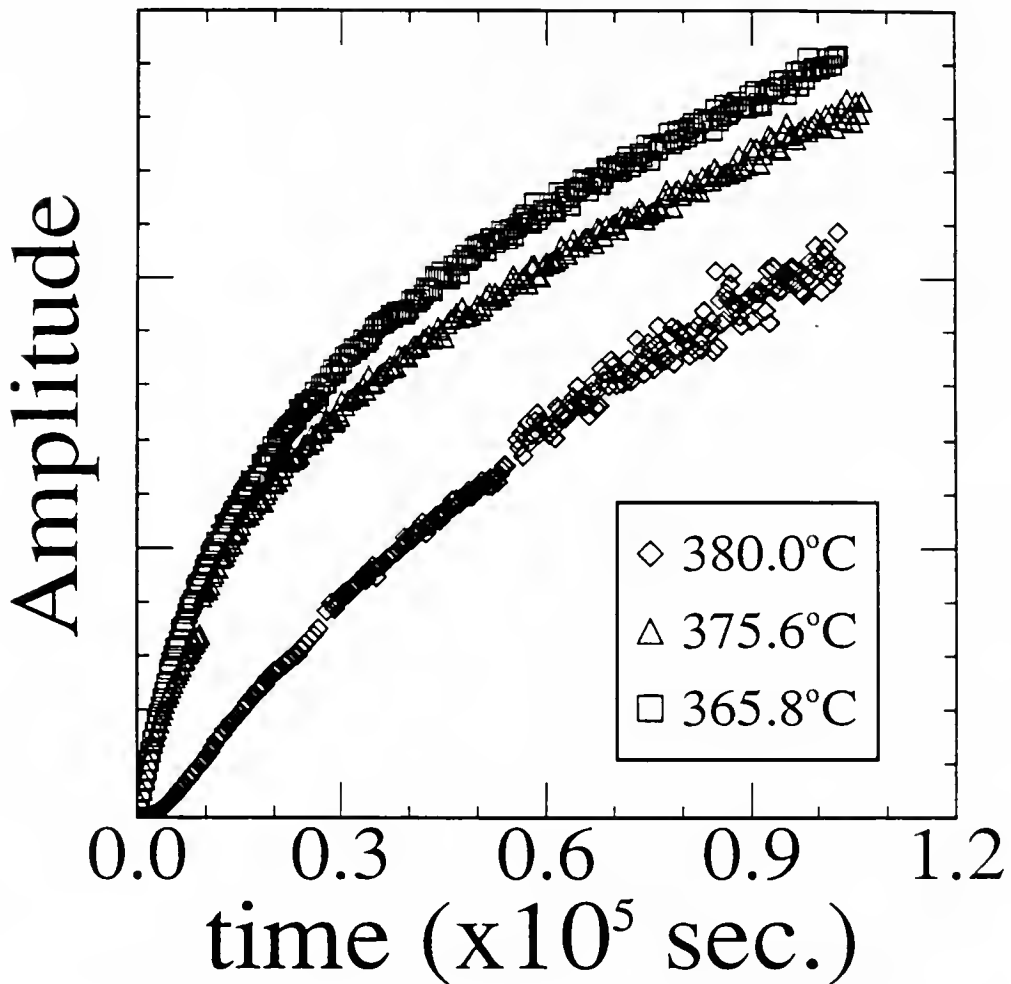


FIG. 22. Convolution fitted amplitude vs. time for the temperatures shown. The delay seen in the plot of the integrated intensity is also seen here.

dimensions, therefore, the measured amplitude should roughly scale as $L(t)^{d-2}$ and have a time dependence of $t^{1/2}$. A plot of $\text{Log}_{10}(\text{amplitude})$ vs. $\text{Log}_{10}(\text{time})$ is shown in figure 23. The late time slope for the deeper quenches is 0.46, a value close to the value found for the time dependence of L as will shortly be discussed. Trying to extract the time dependence of L from the amplitude would not be a good method due to the uncertainty of the resolution effect. However, it is reassuring that a value close to the expected value of $1/2$ is found, indicating that the scaling involved is as expected from theory. The curvature in the Log-Log plot is at least in part due to the resolution function.

From a simplistic Ising model calculation it might be argued that the integrated intensity should be constant and that in the previous graphs the rise in integrated intensity is due to the resolution function integrating over more of the peak as the peak becomes narrower. This is not the case. First of all the integrated intensity is calculated from the product of the fitted width and the fitted amplitude, not from the sum of all the counts. Hence, the intensity in the tails is accounted for (at least in the direction scanned). Figure 24 shows the integrated intensity, amplitude and constant background as a function of time. In this multiple plot the background has been multiplied by 1000 to plot it on the same scale as the amplitude. The fact the fitted background is 1000 times or more smaller than the fitted amplitude implies that the missing intensity would have to be spread out in a volume 10^3 times larger than what was effectively covered. It is obvious that some of the intensity is being falsely counted as the background due to the rise in the background with time. However, this change in fitted background is in the wrong direction because the argument says intensity is missing at early times not late. This is a different problem that is discussed in connection with power law growth.

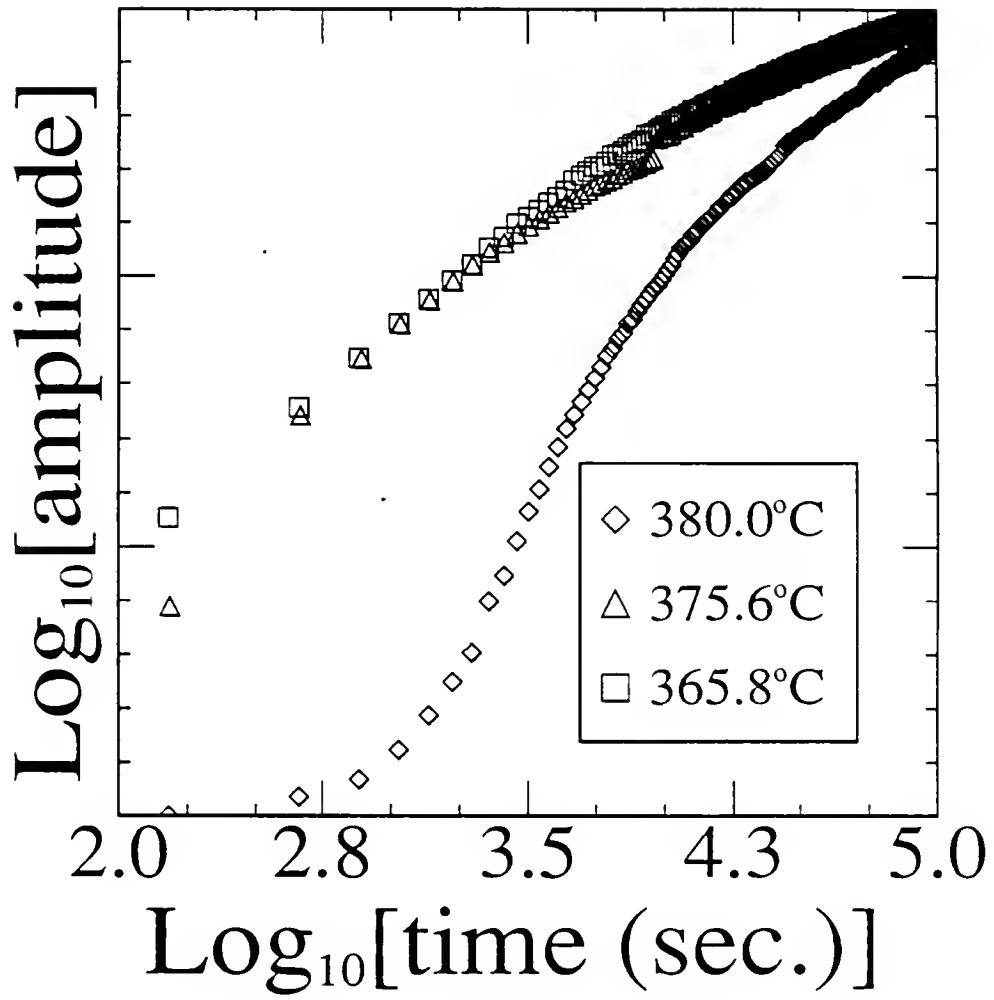


FIG. 23. $\text{Log}_{10}(\text{amplitude})$ vs. $\text{Log}_{10}(\text{time})$ for the same data as in figure 22.

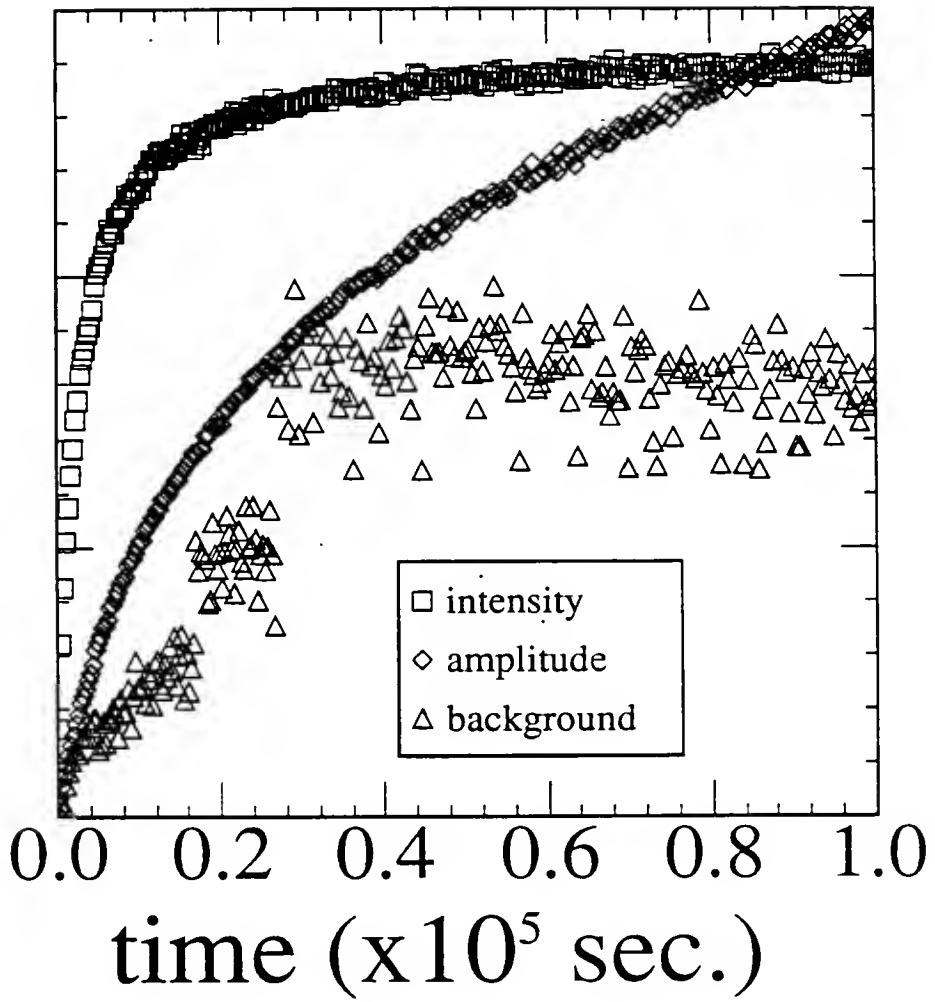


FIG. 24. Plots of integrated intensity, amplitude and fitted constant background. The background has been multiplied by 10^3 in order to plot it on the same scale as the amplitude. The integrated intensity has also be scaled to fit on the graph.

The background should probably be quadratic due to a diffuse peak arising from thermal fluctuations. Moreover, the fitted background for the second and third points is slightly negative, once again indicating that if any thing the change in intensity is greater than suggested by the plots.

The above argument shows that any missing intensity can not be coming from the direction that was scanned. The resolution function in the vertical direction is large which strongly implies that any missing intensity is lost in the radial direction. As it happens several quenches with radial scans using the graphite monochromator and analyzer (what has been called the transverse set up) were tried. The resolution in that direction turned out to be too large; within an hour after a quench the instrument was resolution limited. The width after six hours suggests that the resolution was close to $.02\text{\AA}^{-1}$ (FWHM). Remember that at the $[0,1,0]$ the radial direction probes the thin part of the scattering disk. Based on this value for the radial resolution the intrinsic peak width is equal to the instrumental resolution width 16 minutes after the quench. At this point the peak should be almost completely integrated over (for the deeper quenches). Some of the intensity could still be lost in the tails due to differences in line shapes. The intrinsic line shape at this time is approaching that of a LSQ and the instrumental resolution (figure 11) is some thing between a gaussian and a LSQ. A time of 16 minutes corresponds to the fourth point in figure 24, which has an intensity of 35 percent of the final intensity. Hence, about 65 percent of the change in intensity is real. An even stronger argument can be made for the radial data. A change in integrated intensity has also been seen in other systems by N. Wakabayashi⁽¹⁰⁷⁾

Figure 25 shows a plot of $\log_{10}(L)$ vs. $\log_{10}(t)$ whose slope is "a" in;

$$L(t) \propto t^a \quad (4.3)$$

In table 2 are listed the exponents "a" for curvature driven growth, as a function of

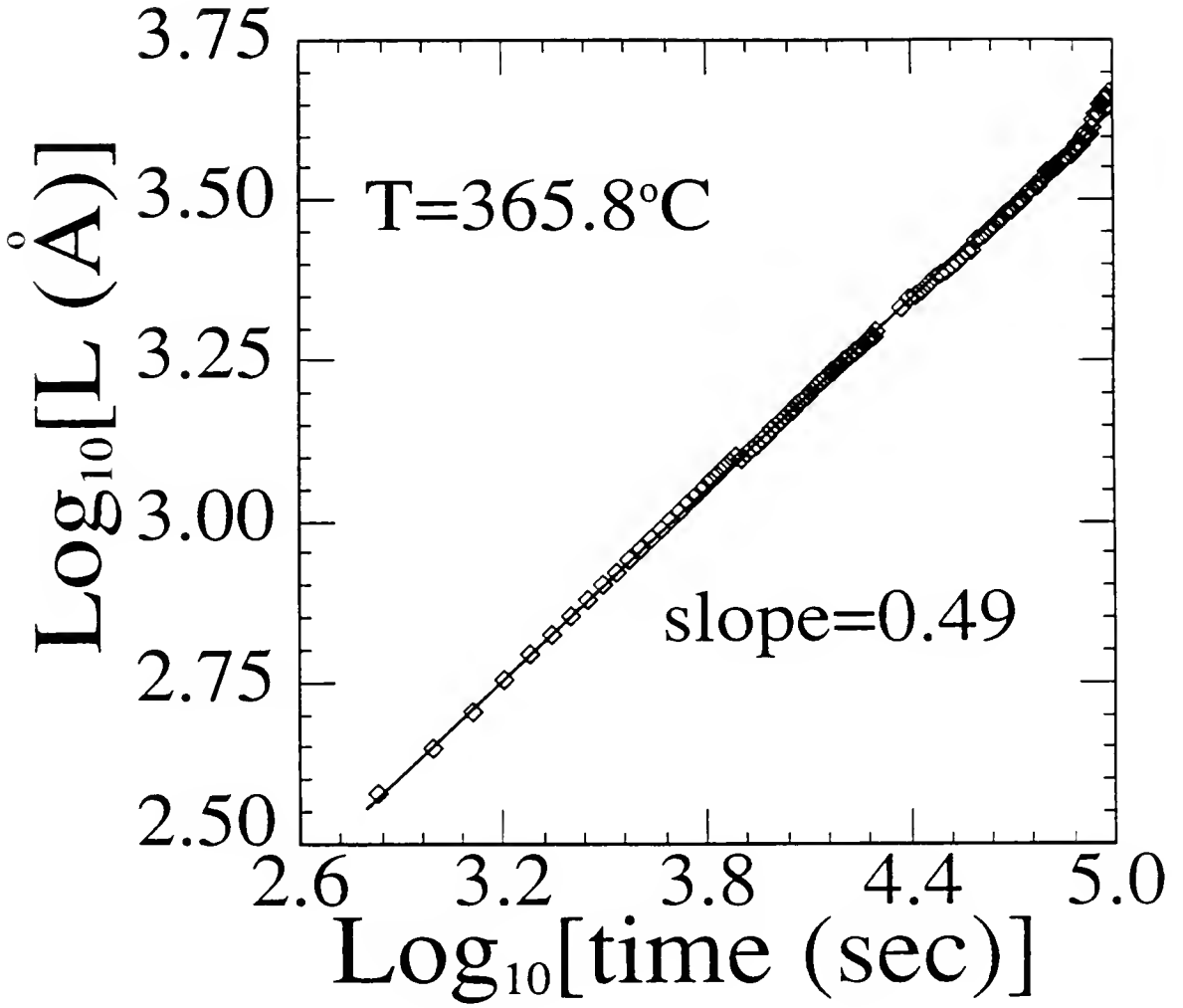
Bulk Cu_3Au 

FIG. 25. $\text{Log}_{10}(\text{Length})$ vs. $\text{Log}_{10}(\text{time after the quench})$. $L \propto 2\pi/\Gamma$, where Γ is the LSQ fitted width. Solid lines are linear fits whose slope corresponds to the exponent "a" for power law growth.

temperature and type of background. For the radial data the order of the polynomial background was not important because only the constant term gave any sizable contribution. The exponent for the radial data was found to be $.50 \pm .03$ and temperature independent. Here, the error in "a" was estimated from the effect of changing the resolution correction, as well as the standard deviation as calculated from values at different temperatures, which was 0.014. An error in the resolution correction would contribute a systematic error, however, this correction as discussed earlier is dominated by the instrumental resolution, which is well known. This is not the case in the transverse direction, where the resolution correction is less well defined and the order of the polynomial background seems to affect the result.

Table 2. Exponents "a" for power law growth (equation 4.3).

direction background	constant	transverse linear	quadratic	radial constant
temperature	"a"	"a"	"a"	"a"
382.0°C	0.45	0.47	0.49	0.49
380.0°C	0.54	0.56	0.58	—
375.6°C	0.40	0.40	0.45	0.51
370.8°C	0.42	0.43	0.46	0.51
365.8°C	0.40	0.43	0.46	0.49
average	0.44	0.46	0.49	0.50
std. dev.	0.06	0.06	0.05	0.01

It should be noted that the 380°C transverse data is inconsistent with all the other data, yielding a significantly larger exponent than the others. The reason for this is unknown. However, this set of data was from the first quench after etching and annealing of the sample, and hence, can be separated temporally from the rest of the data. During the experiment the filament in the x-ray source burnt out and

was replaced, however, this happened late in the series of quenches rather than after the first one. However, changes in the filament before failing may be important. Evidence for the change in "a" being due to the filament can be found in the fact the exponents "a" can be correlated to the order that the data was collected. The value obtained for "a" in the transverse direction decreases with time up till the filament was replaced then goes up. This could be a result of the filament sagging with time, and hence, changing the effective resolution. Movement of the x-ray beam would have at least two effects, one it would very slightly change the area of the sample considered, perhaps having an effect through the mosaic, two it would misalign the sample. However, the most likely way that the resolution would be changed is simply by increasing the spot size on the anode that the x-rays are emitted from. A lower value for "a" would be consistent with an under correction for resolution. Furthermore, this change in "a" cannot be correlated with temperature. The filament was replaced before the 382°C quench and after all the others listed in table 1. Consequently, the instrumental resolution, which was measured after the series is better known for the 382°C data. As can be seen in table one the exponents "a" in the transverse direction found from assuming a constant or linear background are smaller than those from a quadratic background. All values of "a" in the transverse direction are less than 0.5 except for those connected with the 380°C quench, which are all above 0.5. In any case, the average values for each type of background are within their respective standard deviations to each other and 0.5 in spite of the systematic errors in determining "a" from the transverse scans. More importantly it was type 2 domain walls that were suspected of not following curvature driven growth. Type 2 walls are probed by radial scans, and hence, "a" is known to a high degree of accuracy for the domain walls in question. This implies that curvature-driven growth applies to different types of walls and confirms scaling in an anisotropic system.⁽²⁷⁾

The possibility of a lower exponent for the transverse data might be explained as being due to impurities or incorrect stoichiometry. Random imperfections lead to slower growth, possible a $\log(t)$ growth law.^(81,83,84,108) However, a systematic error in the resolution correction is the more likely explanation, especially in light of the fact type 2 walls are not affected.

The Experiments on Sputtered Films and the Effect of Stoichiometry

Experimental Details

A single target of Cu_3Au was used to produce the fine grained sputtered films on substrates of 0.13 mm thick HN kapton or 0.13 mm thick Al_2O_3 . A glass slide was placed in the chamber with the other substrates so that film thickness could be determined with a stylus profilometer. Electron—microprobe techniques verified the stoichiometry and Rutherford back scattering showed the composition to be uniform as a function of depth. The film characteristics are independent of which substrates was used. The stoichiometric film (film A) was deposited on kapton to a thickness of 7500 ± 300 angstroms, with a composition

$\text{Cu}_{0.75 \pm .01} \text{Au}_{.25 \pm .01}$ as determined by electron microprobe techniques.

The nonstoichiometric film (film B) was deposited to an initial thickness of $10,000 \pm 400$ angstroms on an Al_2O_3 substrate. Subsequently the film was placed in contact with a clean Cu block and annealed under vacuum for 2.5 hours at 500°C . The clean Cu block was the heating rod previously discussed in connection with the furnace. The tantalum foil used in later experiments to shield the sample was added due to experience with this film. After the data was collected and the transition temperature was found to be 299°C the film was recharacterized by

electron-microprobe techniques, the results showed the sample to have a homogeneous concentration profile of $\text{Cu}_{0.79 \pm 0.01} \text{Au}_{0.21 \pm 0.01}$. This stoichiometry is consistent with the transition temperature.

Preliminary x-ray characterization of the films found the $[1,1,1]$ direction to be normal to the substrate to within a mosaic spread of approximately 0.2 \AA^{-1} or 3° half width at half maximum (HWHM). The in plane orientations were random. The lattice constant at room temperature was 3.74 \AA . Prior to the first quenches both films were annealed at 350°C for over 12 hours in a vacuum. Earlier measurements on other films showed changes in the relative intensities of the $[1,1,1]$ and in plane fundamentals as a result of the first annealing, implying an improvement in the orientation of the grains along the $[1,1,1]$ direction.

Initially kapton substrates were used. Kapton is transparent to x-rays, easily cut to fit any sample mount, and inexpensive. However, it bows when heated to high temperatures. Heating the kapton prior to film deposition may have helped, but it must be heated in a vacuum. Even in a vacuum of a few millitorr the kapton would deteriorate over several weeks if held above 350°C , as was done during the experiments. Another problem with kapton substrates is its low thermal conductivity, most of the thermal conduction was in the film itself. Substrates of Al_2O_3 have better thermal properties than kapton for these experiments.

Kapton was also used for the x-ray windows on the first version of the furnace which was used in connection with all the sputtered films. Although the vacuum obtained with kapton windows is a little poorer than with beryllium windows, they are considerably less costly and worked very well in the testing of the design of the furnace, prior to manufacturing the present version. Moreover, kapton unlike beryllium is reasonably transparent to visible light allowing visual observations of the interior of the furnace which helped pinpoint weakness in the

design. The only other relevant difference between the furnace described for the bulk sample and this one is that the sample mount was a frame not a plate, allowing the diffraction peaks to be observed in a transmission geometry. Improvements in the heating element are discussed in connection with the experiments on the M.B.E. films where the changes were implemented.

The data was collected in the radial direction with a PSD as described earlier and shown schematically in figure 10a. The instrumental resolution was $.06^\circ$ (HWHM in 2θ) or 0.0042\AA^{-1} at the $[1,0,0]$, and 0.0041\AA^{-1} at the $[1,-1,0]$. Quenches on both the $[1,0,0]$ and $[1,-1,0]$ were done, in order to observe both types of walls. Radial scans widths of the $[1,0,0]$ are broadened by type 2 walls. The $[1,0,-1]$ peak width is affected by both types of walls but is dominated by type 1 walls. The notation $[1,-1,0]$ instead of $[1,1,0]$ is used to indicate that it is perpendicular to the $[1,1,1]$, or in the plane of the film. The transition temperature T_c for each sample was determined from the disappearance of superlattice peaks upon heating. The samples were heated well above T_c to ensure complete disorder, then cooled to an initial temperature $T_i > T_c$. After establishing equilibrium the films were quenched rapidly to $T_f < T_c$. X-ray scattering scans were collected and stored sequentially at fixed T_f .

Analysis for Data on the Sputtered Films

In analyzing the data a gaussian shape was assumed for all the fitted peaks. Superlattice peaks from a bulk sample are lorentzian squared like, not gaussian. The shape of the peak due to the existence of anti-phase domains is difficult to see experimentally in films due to the contribution from finite size. A gaussian shape, however, can be supported. Each grain in the film that contributes to the

scattering, will in general be out of phase with the rest, producing the superposition of (possibly LSQ shaped) peaks with a random distribution in phase. The resulting peak should be well approximated by a gaussian. Furthermore, the peaks as measured were gaussian. Therefore, the data was fit to gaussians, and then instrumental resolution, finite size and strain were subtracted in quadrature,

$$\sigma = \sqrt{\sigma_{\text{fit}}^2 - \sigma_c^2} \quad (4.4)$$

where σ_c is the correction from instrumental resolution, finite size and strain. The values of σ_c are listed with the results. Instrumental resolution was measured by the width of a Si [1,1,1] as was done with Ge for the bulk data. The contribution from finite size and strain was estimated from measurements of fundamental Bragg peaks in the same directions in reciprocal space as the superlattice peak. The measurements from the fundamental peaks were not sufficient to consistently determine the corrections for these samples. The actual correction used was a probable upper bound, which as discussed below, may cause a cause a systematic error in analyzing the data.

The time dependence is analyzed by fitting to functional forms as discussed in chapter four, specifically power law (equations 2.5 and 4.3) and logarithmic (equation 2.12) time dependence. The comparisons made between samples are such that the quench depths are the same. The quench depth being the same means that the absolute temperatures are 187°C apart. In order to rule out the possibility of any effect being due to the difference in absolute temperature one quench to 278°C on the bulk sample was done. The results indicated curvature driven growth as is found at higher temperatures.

Results from the Sputtered Films

Some typical raw data from a time resolved run on the Cu rich film are shown in figure 26. The data on the stoichiometric film is similar but with better signal to background. Figure 27 shows log-log plots of L vs t for the $[1,0,0]$ and $[1,-1,0]$ superlattice peaks in both film A and B. The quench depth ($T_c - T_f$) is roughly the same for each run shown. In both films the $[1,0,0]$ peaks are much narrower than the $[1,-1,0]$ peaks, due to the anisotropy of the domains. These results support, although not as strongly, the isotropic growth found in the bulk sample.

Comparing the results from the different samples, it is clear that domain growth proceeds much faster in the stoichiometric film. Fitted growth exponents, as in equation 4.3, are listed in Table 3. The quoted errors are dominated by estimates of the systematic error arising from uncertainty in the resolution and finite size corrections. The stoichiometric film has a ≈ 0.4 , roughly consistent (within experimental uncertainties) with curvature driven growth ($a = 1/2$). On the other hand, values of $a \approx 0.2$ are obtained for the film with extra Cu. This cannot be reconciled with curvature driven growth.

Table 3. Quenches and fitted exponents.

film	peak	$T_f (^{\circ}\text{C})$	$T_i (^{\circ}\text{C})$	$T_c (^{\circ}\text{C})$	σ_c (channels [*])	a [Eq. 4.3]	m [Eq. 2.12]
A	(1,-1,0)	365	393	386	17.1	0.42 ± 0.08	4.9
A	(1,0,0)	364	396	386	14.8	0.41 ± 0.11	4.2
B	(1,-1,0)	278	320	299	13.5	0.23 ± 0.04	2.2
B	(1,0,0)	283	320	299	19.0	0.18 ± 0.06	1.9

* At the (1,-1,0) peak position, 1 channel corresponds to $\Delta Q = 8.51 \times 10^{-4} \text{ \AA}^{-1}$.
At the (1,0,0) peak position, 1 channel corresponds to $\Delta Q = 8.71 \times 10^{-4} \text{ \AA}^{-1}$.

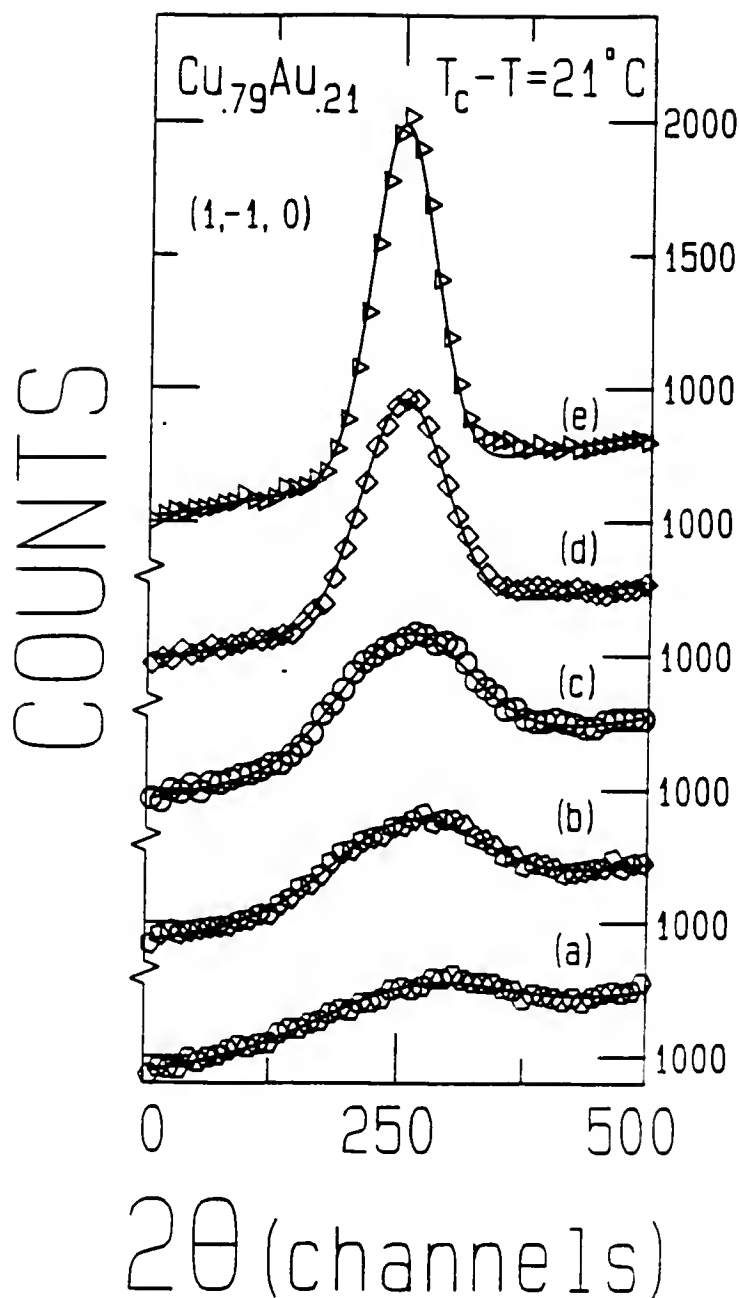


FIG. 26. Typical $[1,-1,0]$ profiles from film B quenched to 278°C . For clarity of presentation, the data points are averaged in groups of ten, and spectra are offset in increments of 500 counts. Counting times are 1000 sec. for each 1024 channel scan. Only the central 500 channels are shown. Each channel corresponds to $\Delta Q = 8.51 \times 10^{-4} \text{ \AA}^{-1}$. The solid lines are gaussian fits. Times after the quench: (a) 1.50×10^3 sec., (b) 3.48×10^3 sec., (c) 6.48×10^3 sec., (d) 3.65×10^4 sec., (e) 1.70×10^5 sec.

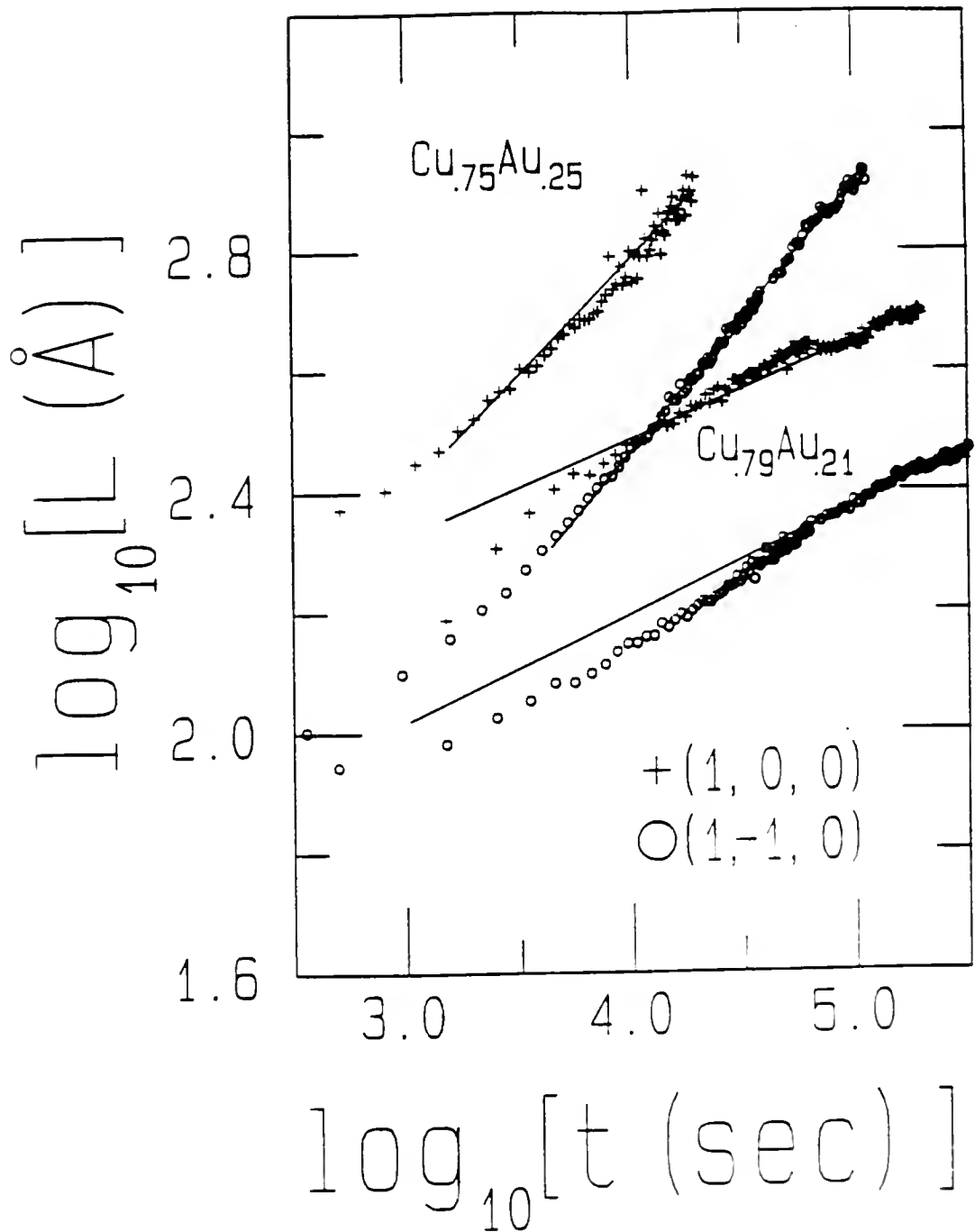


FIG. 27. $\log_{10}L$ ($2\pi/\sigma$ in \AA) vs. $\log(t)$ (time after quench in seconds) for film A (upper curves) and film B (lower curves). The solid lines are power law fits to the late-time data. The discontinuity in the film B $[1,0,0]$ data is a known experimental artifact.

Figure 28 is a plot of L vs $\log(t)$ for the same four runs. Over the range of times measured, it is apparent that the data for stoichiometric film are not consistent with $L \propto \log(t)$, while the Cu rich film data are consistent with a logarithmic growth law. Since it is energetically favorable for ordered domains to have Cu_3Au stoichiometry the extra Cu in film B can be viewed as a diffusing impurity.

Recent simulations^(84,109) of diffusing impurities in an Ising model with Kawasaki dynamics found that domain coarsening begins with an apparent $t^{1/2}$ regime which saturates at an impurity concentration dependent value. At late times impurities concentrate along the domain walls, eventually restraining wall motion. The order of the ground state degeneracy and the symmetry of the order parameter⁽¹⁰⁹⁾ involved do not change these results..

Although the $\text{Cu}_{0.79}\text{Au}_{0.21}$ data do not display an obvious early time $t^{1/2}$ regime, the general behavior is consistent with that observed in the simulations. In particular, the ongoing concentration of extra Cu atoms along domain walls is a physically attractive and reasonable scenario.⁽⁸⁵⁾ Further, large, massive clusters of Cu atoms will have less mobility than a single atom, hence, at late times the situation may resemble a model with quenched impurities.

It has been predicted⁽⁸⁰⁾ that an Ising system with quenched, random impurities will show domain coarsening of the form of equation 2.12. Figure 29 shows a plot of the $\log(L)$ vs $\log[\log(t)]$. The straight line fits give the exponents m listed in table 3. It is interesting to note that the best fit value $m \approx 2$ for the non-stoichiometric film is essentially equal to the first order ϵ expansion result (reference 80) $m = 1.82$ obtained for a three dimensional Ising model with impurities. Unfortunately, the available range of data is probably too small to extract a definitive value for m . It is evident from figure 26 that the film B data could also be consistent with $m = 1$.

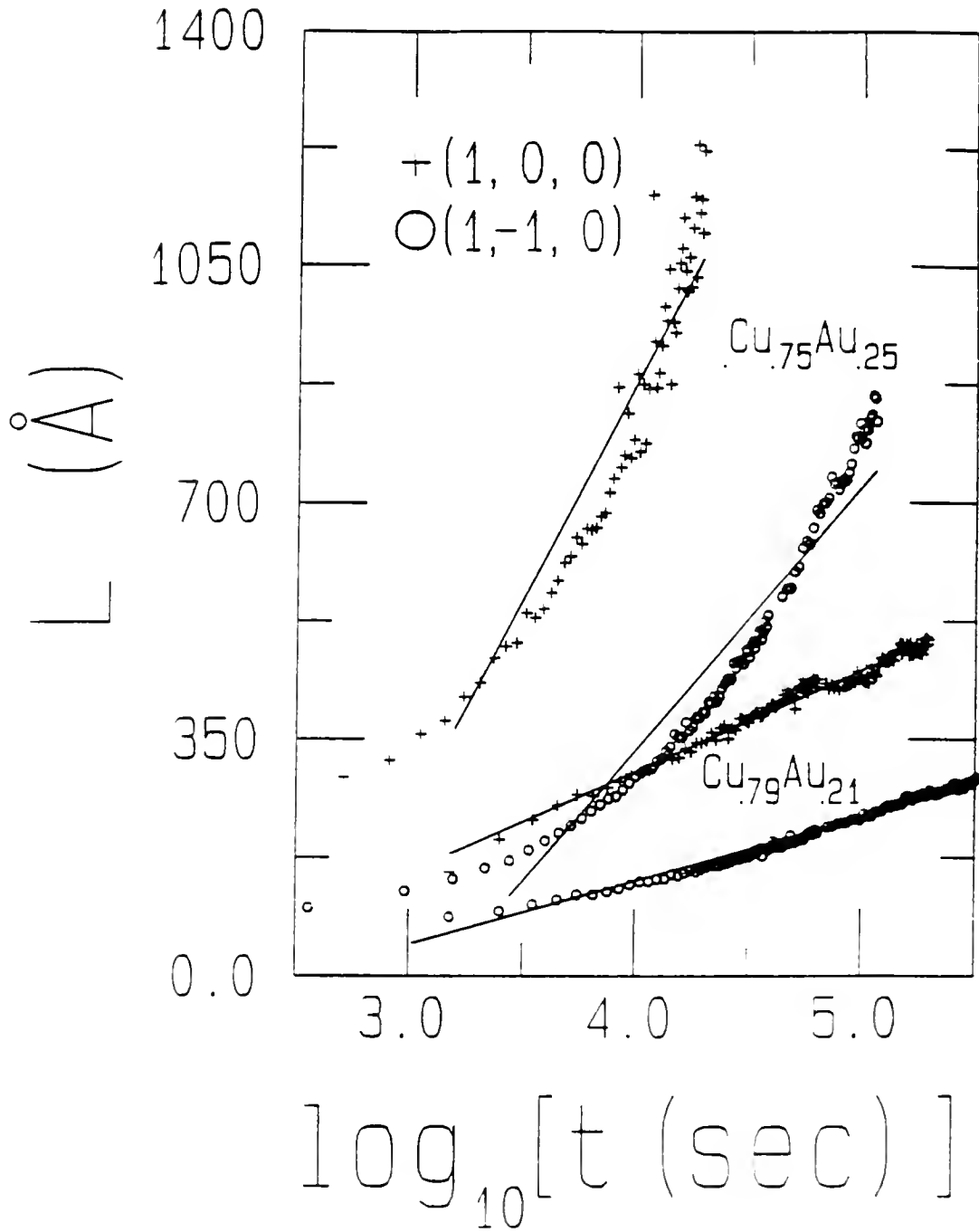


FIG. 28. L vs. $\log_{10}(t)$ for the runs summarized in table 3. The solid lines are the best linear fits to the data for each run.

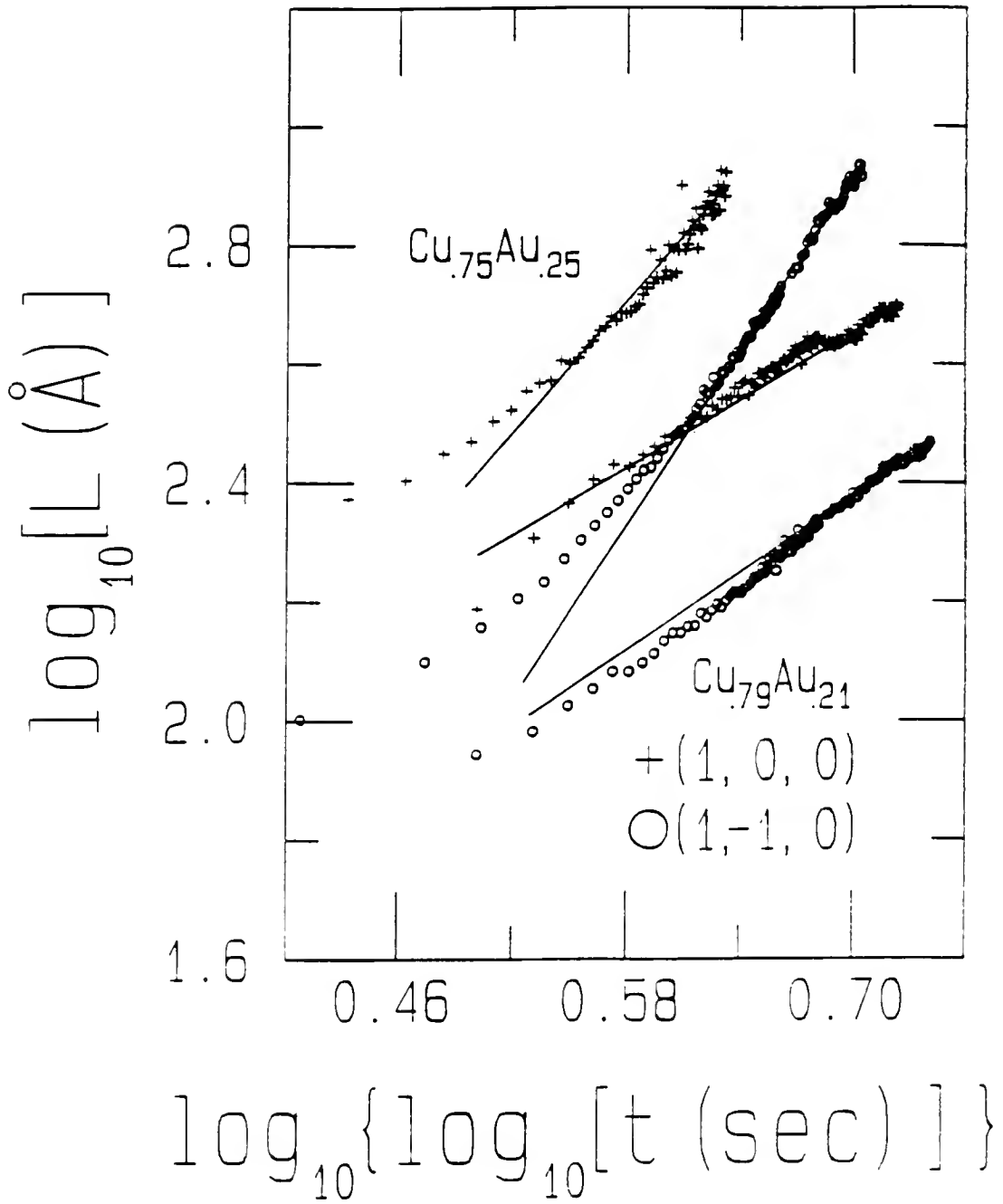


FIG. 29. $\log_{10}(L)$ vs. $\log_{10}[\log_{10}(t)]$ for the runs summarized in table 3. The solid lines are linear least square fits to the last half of the data for each run.

It might be concluded from the data on the stoichiometric sputtered film that there is no change due to sample thickness down to 7300\AA . This would not be a valid conclusion. The time dependence of the domain size in the stoichiometric film was found to be $L=t^{0.42\pm0.8}$, consistent with $L=t^{0.5}$. However, the correction used in association with the sputtered films was a probable upper bound to the true resolution. This tended to make the $\text{Log}_{10}(L)$ vs. $\text{Log}_{10}(\text{time})$ plot into a straighter line. In analyzing the data on the 4500\AA M.B.E. film it was discovered that significant over correction of the data was necessary to force the $\text{Log}_{10}(L)$ vs. $\text{Log}_{10}(\text{time})$ plot to be linear. Moreover, the slope of such an over corrected line was 0.4, a value close to that obtained for the sputtered film. Fortunately, the off-stoichiometric film was thicker ($10,000\text{\AA}$) than its counter part, and having analyzed the two sputtered films in the same way, means that the difference must be due to the composition not thickness. These ambiguities due to the correction serve to stress the importance of measuring the resolution very carefully.

The M.B.E. Films

Experimental Details

The M.B.E. films were grown on a sapphire (Al_2O_3) substrate with a buffer layer of Niobium at the University of Illinois by J. A. Dura and C. P. Flynn. Niobium (Nb) is bcc with a lattice constant of 3.30\AA . As with the sputtered films the $[1,1,1]$ direction is normal to the film surface. The M.B.E. films are single crystals, therefore, the $[1,0,-1]$ is in the plane of the film but the $[0,1,0]$ is not. The orientation of the crystal was determined from the $[1,1,1]$, $[1,0,-1]$ (or the $[2,0,-2]$), and the $[0,2,0]$. The lattice constants for the three films varied less than 0.3 percent

between different film thicknesses and less than 0.5 percent between different directions in each film. The in plane lattice constant is $3.770 \pm .006 \text{ \AA}$, which is the same value found for the bulk sample. The out of plane lattice constant is $3.753 \pm .006 \text{ \AA}$. This difference in the lattice constant strongly suggests that strain is important in these systems.

Shortly after the films were prepared Rutherford Back Scattering was used to determine film thickness and sample stoichiometry. The atomic percentages of Au in the 4500 \AA , 710 \AA , and 260 \AA films were 26.4 ± 0.4 , 27.2 ± 0.4 , and 26.0 ± 1.0 respectively. The results on the $4500 \pm 100 \text{ \AA}$ film indicated that the interface between the Cu_3Au layer and the Nb buffer layer was sharp. The corresponding interfaces for the $710 \pm 20 \text{ \AA}$ and 260 \AA film overlapped. After the time dependent x-ray data had been collected Auger electron spectroscopy was used to test for impurities in the 4500 \AA and 260 \AA films and Rutherford Back Scattering was again used for the 710 \AA sample. The results indicated that the 4500 \AA and 710 \AA films were free of impurities and that the 260 \AA film had slight traces of oxygen (2 ± 1 atomic percent) and niobium (3 ± 1 atomic percent) diffused throughout the film. For the thinnest film oxygen was also present in the niobium buffer layer with a peak in concentration at the Nb/ Cu_3Au interface which could be explained by oxygen diffusing through to the buffer layer along grain boundaries. The niobium concentration decreases to 3 atomic percent in approximately 70 \AA for the 260 \AA sample. For the 4500 \AA film the niobium concentration dropped to zero in approximately 170 \AA . For all the films there was of course surface carbon and oxygen.

The data taken on the 4500 \AA film was treated similarly to that of the bulk single crystal. Radial scans were collected with the exact same experimental set up used to collect the bulk radial data. The only change for the 260 \AA and 710 \AA films

was in the heating element. Due to the lower thermal conduction in the thinner films it was necessary to improve the heating element. To increase the temperature stability a larger thermal mass was used. The larger mass made quenching more difficult. Therefore, a cooling line was incorporated into the heating element. The details of the heating element/sample mount are shown in figure 30.

The use of the wound wire resistors as shown in figure 30 significantly improved the furnace. Using two resistors, one above and one below the sample minimized temperature gradients. Also the old heating element was prone to burn out, where its life time was dependent on the vacuum maintained in the furnace. The resistors also had a tendency to burn out. However, the life time of the resistors is easily increased by annealing them before placing them in the copper mount. The resistors were heated by running DC current through them, in air, till the ceramic casting just started to melt. This procedure took less than a minute per resistor. Resistors treated in this way have, so far, not burnt out.

Improved quench rates were achieved by flushing nitrogen through the cooling lines in the mount. Further improvement in cooling rates can be achieved by using helium. However, the film temperature lagged that of the mount making the thermal conductivity of the sample the limiting factor in the quench. The new sample mount could be quenched 45°C in 10 seconds using nitrogen gas. Due to the lag in temperature the films were quenched 4 to 45°C in 10 to 25 seconds depending on depth. The quenches for the 4500\AA film using the old heating element (shown in figure 9) took 45 to 90 seconds. The sample temperature was measured by a type K-thermocouple glued to the back of the Al_2O_3 substrate. A second thermocouple was placed on the copper mount where the lower resistor is clamped. This second thermocouple was used as a reference for temperature control. Quenches were performed in a similar way as before, only now a digital delay generator was used to

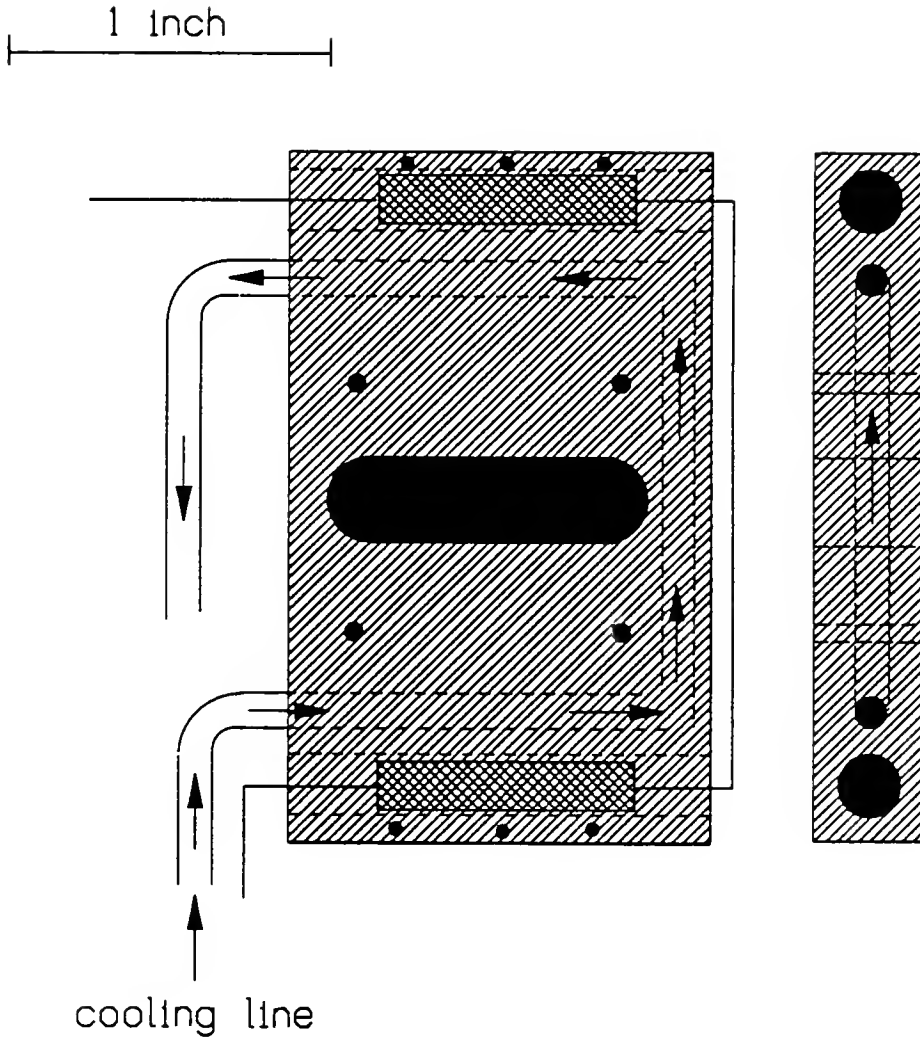


FIG. 30. Heating element/sample mount used for the 260\AA and 710\AA M.B.E. grown films of Cu_3Au . The Cooling lines were used to quench the sample. The placement of the heating resistors above and below the sample position minimizes temperature gradients.

control the flow of nitrogen and start the scans. The Micristar temperature controller was used in the same manner as described in connection with the bulk sample. Since this data was collected the entire procedure has been automated.

Analysis of the M.B.E. Film Data

The shape of the $[1,0,-1]$ peak for the 4500\AA film is LSQ, therefore, the convolution fitting routine was used, as it was with the bulk sample. A scan of the $[1,1,1]$ of Silicon was used to represent instrumental resolution. This scan was convolved with a gaussian representing finite size and strain. The shape of the $[1,0,-1]$ peak for both the 710\AA and 260\AA films is gaussian. Hence, the scans were fit by straight gaussians and then the effective resolution was subtracted in quadrature as was done with the sputtered films.

Only one fundamental peak in the $[1,0,-1]$ direction, namely the $[2,0,-2]$, is observable with CuK^α radiation. For the bulk data on the $[0,1,0]$ two fundamental peaks were used to separate finite size from strain effects. Recalling that, in units of inverse distance (\AA^{-1}) finite size should be a constant and strain should go as the magnitude of the peak, the true correction at the $[1,0,-1]$ must be between one half and one times the width of the $[2,0,-2]$, where instrumental resolution is subtracted and added back in separately. Although finite size effects for peaks out of the plane of the film are important the crystal size in the plane would only have to be three times larger than film thickness in order to make the contribution from finite size small compared to that of strain. Furthermore, from the difference in measured lattice constants relative to the film surface strain should be substantial. The large contribution to the width from strain has also been reported⁽¹¹⁰⁾ to exist in one of the M.B.E. Cu_3Au films prepared at the University of Illinois. Therefore, the

widths were corrected by assuming finite size and strain contribution was all due to strain. This correction is a lower bound to the true contribution. An upper bound would be calculated by assuming finite size broadening dominates over strain. This upper bound is roughly the width of the $[2,0,-2]$ as listed in table 4. Table 4 also lists the corrections used for the three films.

The other work⁽¹¹⁰⁾ on a 2000Å M.B.E. Cu_3Au film investigated surface ordering with time resolved grazing incidence x-ray experiments. In these grazing incidence experiments small disordered clusters were found to persist near the surface as the bulk ordered. Domain growth was seen to be depth independent. However, the average order parameter increases faster in the bulk than at the surface.

Table 4
M.B.E. Film Corrections

M.B.E. film	Instrumental Resolution at $[2,0,-2]$	Width of $[2,0,-2]$	Width of $[2,0,-2]$ -IR	Instrumental Resolution at $[1,0,-1]$	Finite size and strain correction	Total Correction
260Å	2.70	17.9	15.0	3.17	7.50	9.38
710Å	2.70	8.95	7.28	3.17	3.64	5.32
4500Å	2.09	6.52	5.26	2.45	2.63	3.49

all widths ($\times 10^{-3} \text{ Å}^{-1}$)

Results from the M.B.E. films

In the following pages are plots of L vs. time, $\text{Log}_{10}(L)$ vs. $\text{Log}_{10}(\text{time})$, and L vs. $\text{Log}_{10}(\text{time})$ for all three films. In each case the growth is slower than Cahn-Allen curvature driven growth ($t^{1/2}$). These plots also show a temperature dependence for the thinner films. In the three plots for the 4500Å film, shown in

figures 31 through 33, only one temperature has been shown, in part because all the quenches display similar behavior and in part for clarity. The plot of L vs. time for the 4500\AA film is similar to the equivalent plot for the bulk samples. However, the plot of $\text{Log}_{10}(L)$ vs. $\text{log}_{10}(\text{time})$ for this film is different from the bulk. At times shortly after the quench the domains grow with a $t^{1/2}$ time dependence. The power of the time dependence then continuously decreases so that at the end of the experiment the power of the time dependence was 0.2. It is difficult to determine from the data if 0.2 is a limiting value or not. However the range of data that follows a power law of $t^{0.2}$ is also consistent with a logarithmic time dependence. In a plot of L vs. $\text{Log}_{10}(\text{time})$, (figure 33), one can see that at late times the data is almost a straight line. In fact if a slightly larger resolution correction is used the slight curvature at late times disappears and the late time data clearly indicate a logarithmic time dependence for L . Recalling that the minimum value for the finite size and strain correction was used it is evident that L grows as $t^{1/2}$ at early times, then crosses over to a logarithmic or lower power law at late times in the 4500\AA film. Monte Carlo simulations have shown a slowing of the growth due to finite size effects,⁽⁷²⁾ but other effects such as vacancies⁽¹⁰⁹⁾, strain and impurities (or incorrect stoichiometry) induced pinning are more likely to be the dominate cause for the slower growth.

A crossover from $t^{1/2}$ to $t^{1/4}$, as discussed in chapter 2, has been predicted for late times.⁽⁹⁷⁾ The late time power of 0.2 is probably not evidence for a $t^{1/4}$ crossover. The $t^{1/4}$ late time power law is for pure systems, here the small deviation from critical stoichiometry, among other things, could easily explain the slower growth at late times. The data on the 710\AA and 260\AA films, discussed below, do not favor a $t^{1/4}$ late time power law suggesting that the 4500\AA film data, although consistent with this prediction is not related to it.

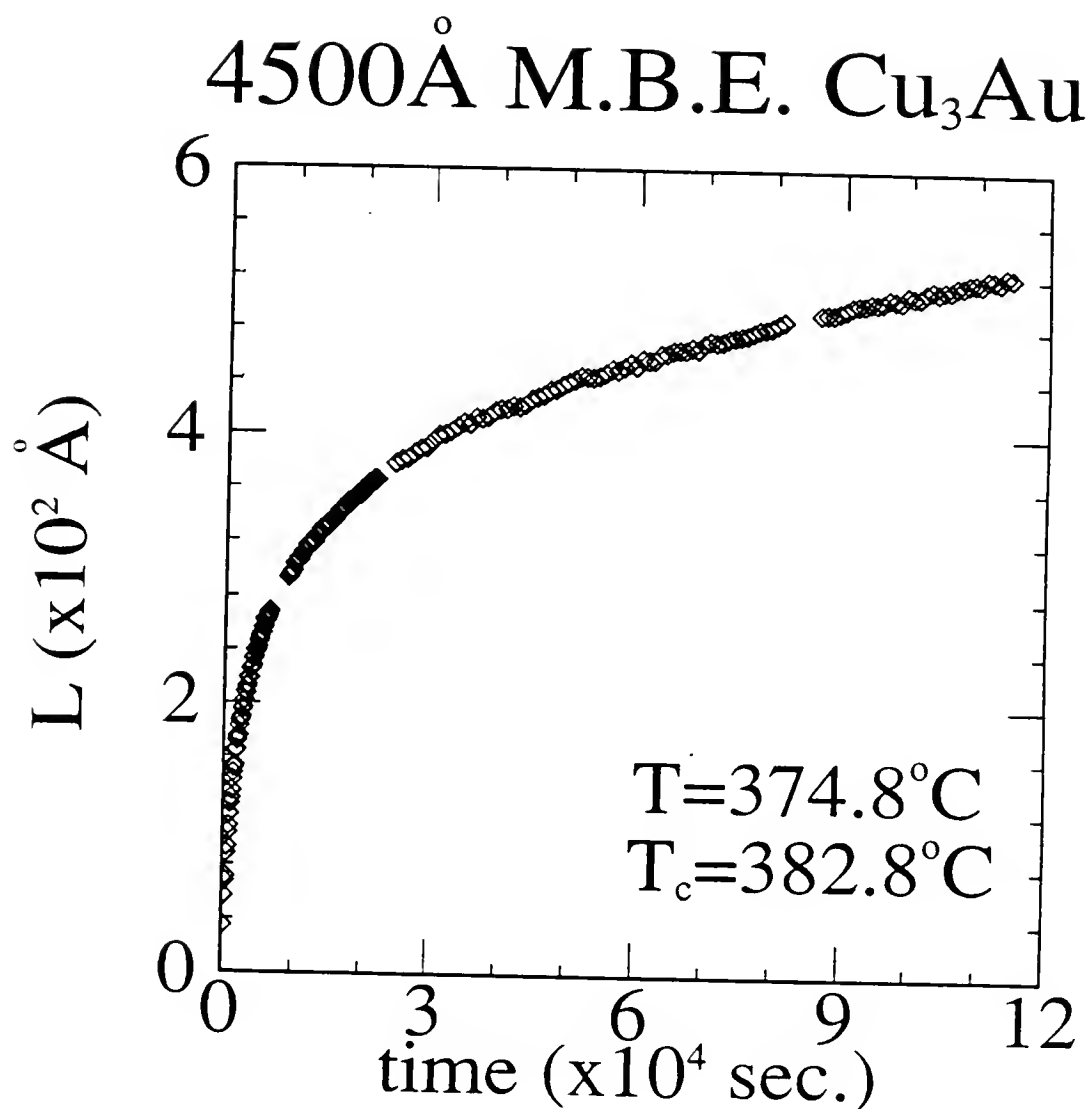


FIG. 31. Size of a domain $L=2\pi/\Gamma$ vs. time for the 4500\AA M.B.E. film of Cu_3Au .

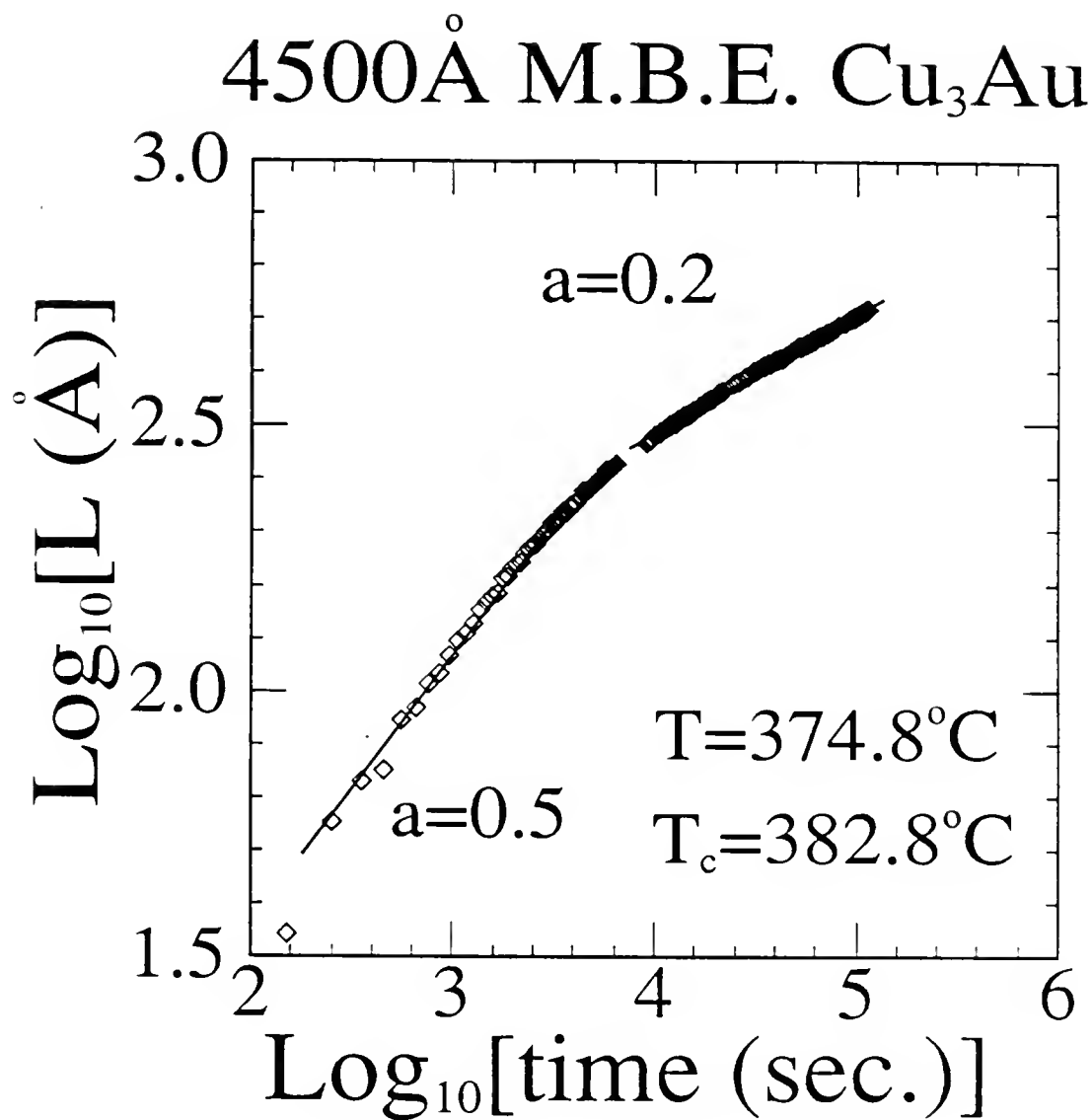


FIG. 32. $\text{Log}_{10}[\text{L}=2\pi/\Gamma]$ vs. $\text{Log}_{10}[\text{time}]$ for the 4500\AA M.B.E. film of Cu_3Au .

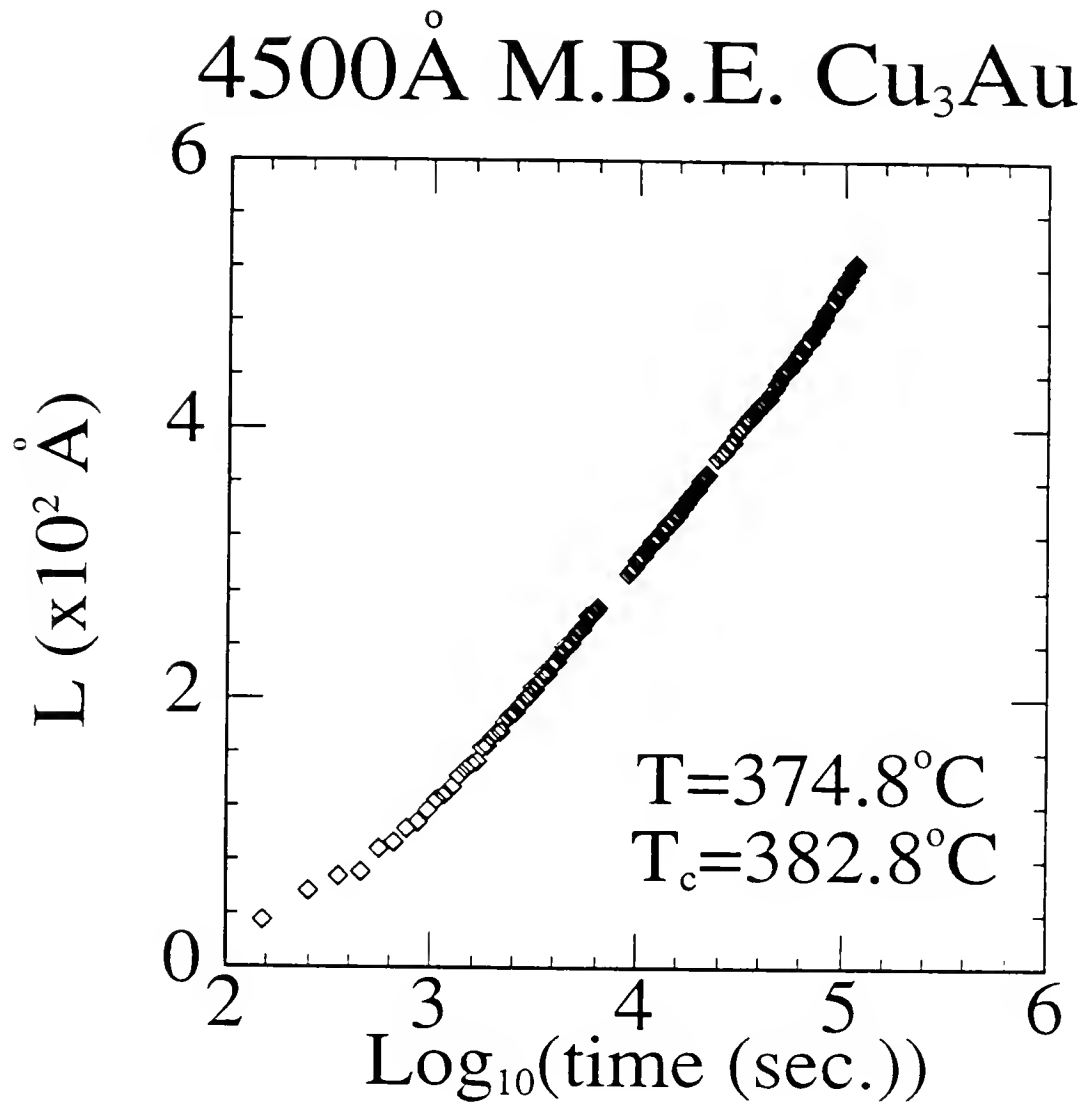


FIG. 33. Size of a domain $L=2\pi/\Gamma$ vs. $\text{Log}_{10}[\text{time}]$
 for the 4500\AA M.B.E. film of Cu_3Au .

The most interesting M.B.E. data is connected with the 710Å film. A plot of L vs. $\text{Log}_{10}(\text{time})$ is shown in figure 34. For the bulk data these curves, as a function of temperature, do not cross each other. However, for the 710Å film it seems that at higher temperatures the late time growth is slower. In fact, it appears as if growth is completely stopping as the transition temperature is approached. Figure 35 is a plot of $\text{Log}_{10}(L)$ vs. $\text{Log}_{10}(\text{time})$ for the same data shown in figure 34. The Log–Log plot shows a slowing of the growth at late times similar to that found in the 4500Å film. However, here, the late time power law for shallow quenches continuously decreases all the way to a power of zero, not to 0.2 as in the bulk. In the plot of L vs. $\text{Log}_{10}(\text{time})$ (figure 36), the deeper the quench the straighter the curve suggesting slower growth with increasing temperature. The growth is also slower at later times for all temperatures, as seen from the curves being concave down. It appears that a logarithmic behavior is approached, or that the period over which such a behavior is obeyed is increased, with decreasing temperature. As discussed in chapter two logarithmic time dependence is expected in systems with energy barriers to growth that are a function of the size of the domains L . Moreover, these barriers are assumed to decay or be overcome exponentially. In the data from the 710Å film it is likely that there are barriers to growth relative to the bulk. In fact, for shallow quenches these barriers seem almost stable at late time giving rise to the near freezing of the growth. As the temperature is lowered there is a greater driving force and the barriers become less stable and begin to decay. However, there is a temperature dependence on the decay rate. A recent Monte Carlo simulation considers ordering in a two–dimensional lattice with annealed vacancies and a NCOP.⁽¹⁰⁹⁾ This two dimensional model produces a crossover from Cahn–Allen to logarithmic like growth, even for half a percent concentration of vacancies. The authors also mention a "slab effect" in which the domains become pinned.

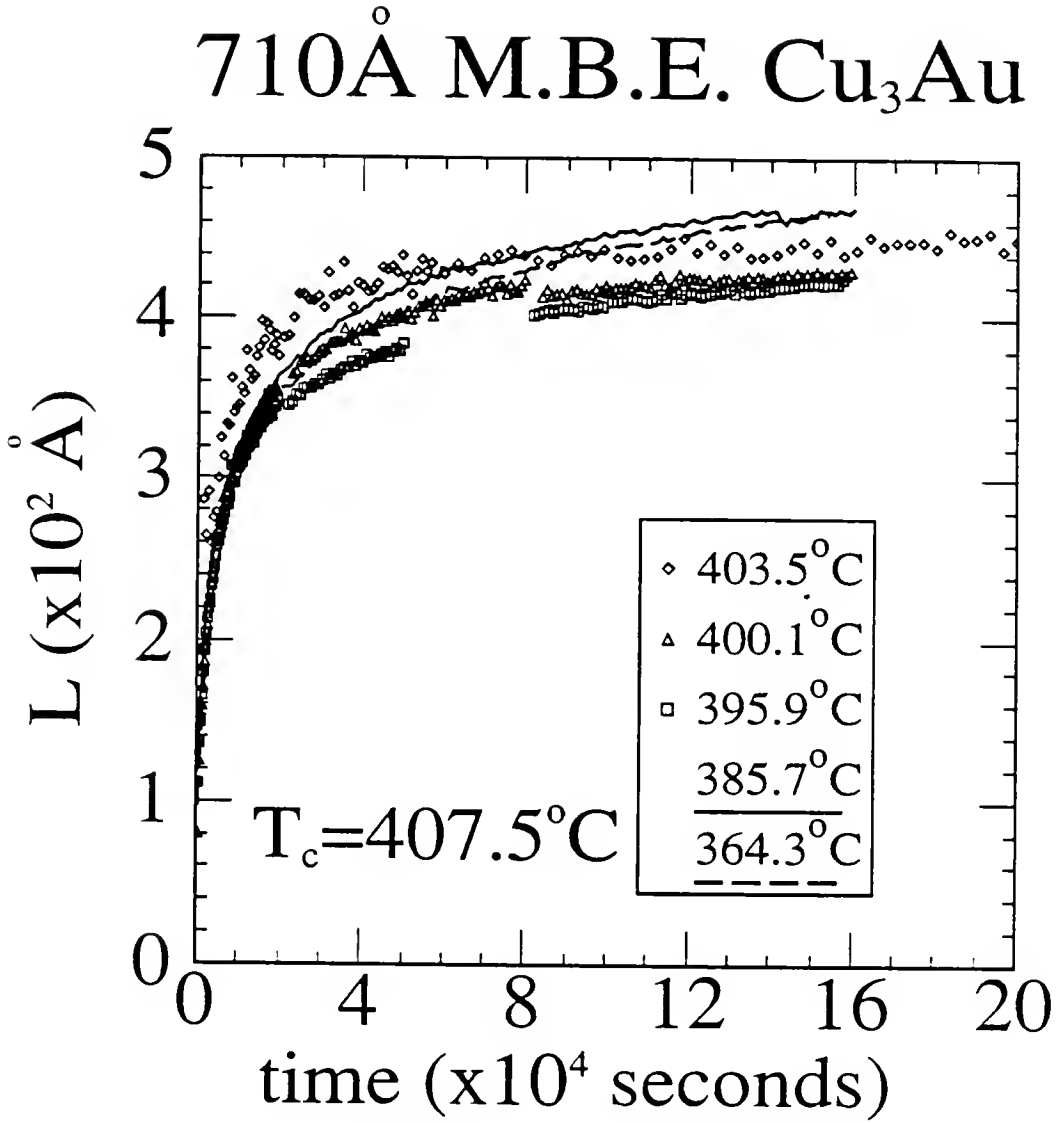


FIG. 34. Size of a domain $L=2\pi/\Gamma$ vs. time for the 710\AA M.B.E. film of Cu_3Au . Five different temperatures are shown.

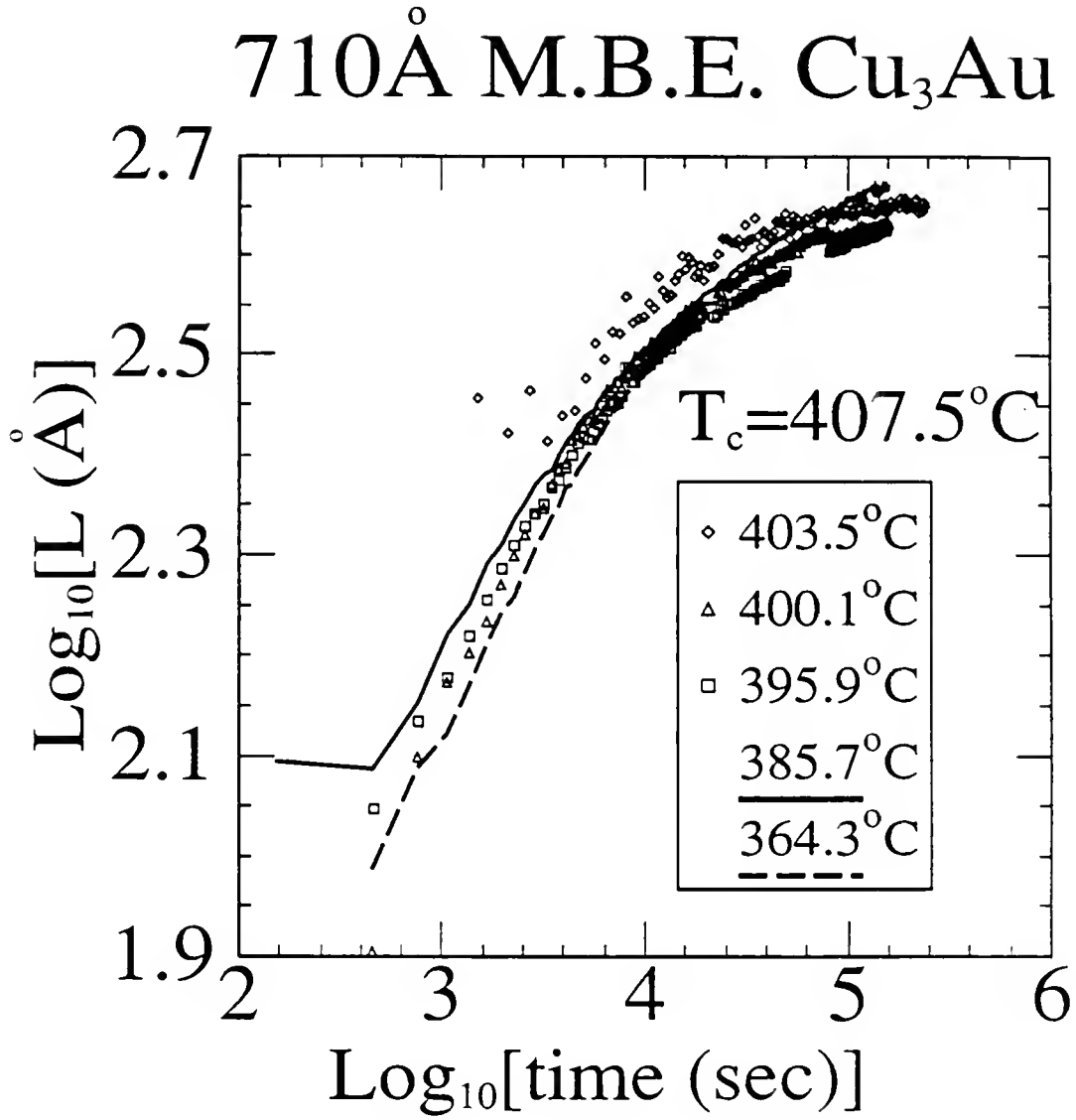


FIG. 35. $\text{Log}_{10}[L=2\pi/\Gamma]$ vs. $\text{Log}_{10}[\text{time}]$ for the 710\AA M.B.E. film of Cu_3Au . Early time slopes are about 0.4. Late time slopes are between 0.0 and 0.2.

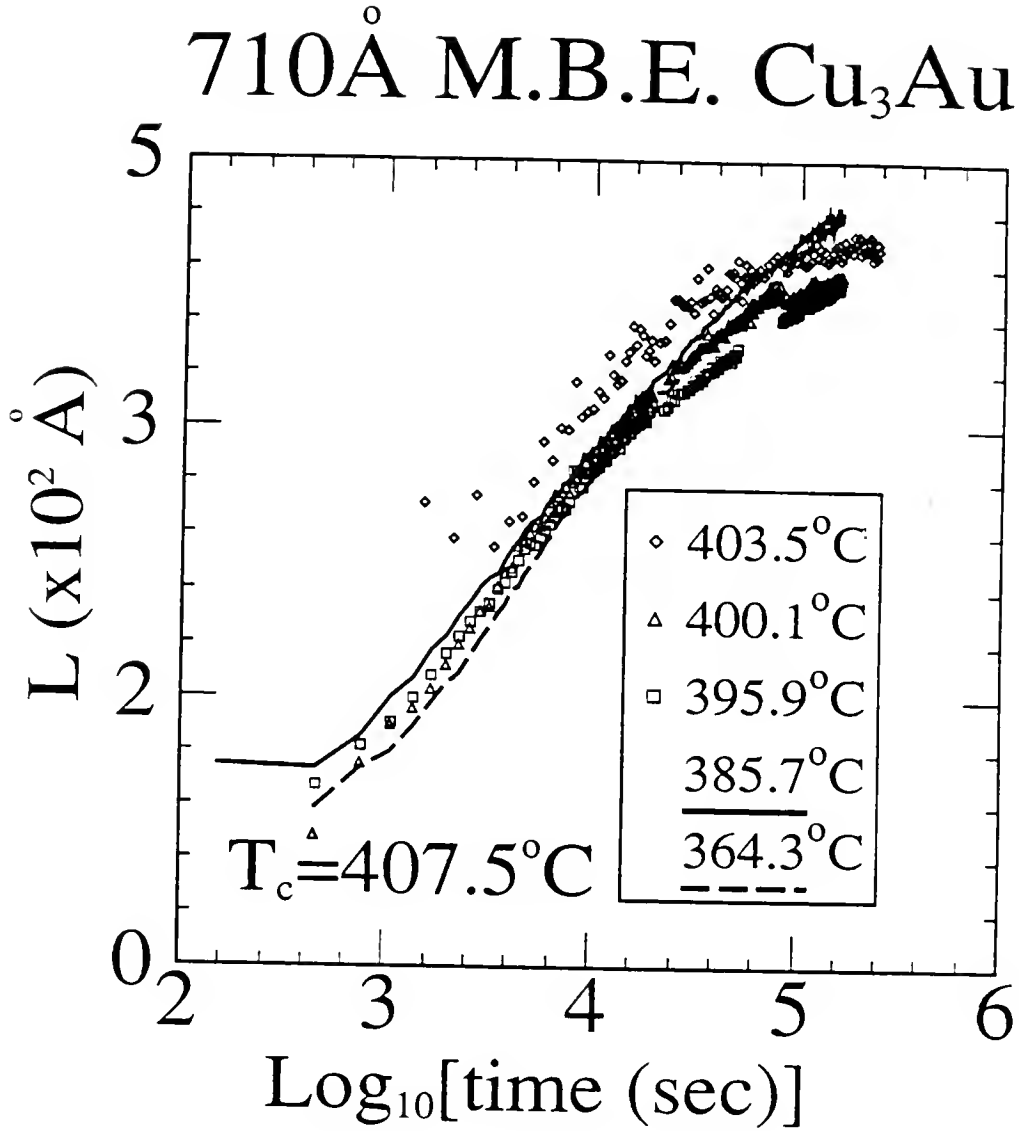


FIG. 36. Size of a domain $L=2\pi/\Gamma$ vs. $\text{Log}_{10}[\text{time}]$
for the 710\AA M.B.E. film of Cu_3Au .

The effect of these barriers is clearly seen in the 260Å film. Figure 37 is the L vs. time plot for the two relatively deep quenches done. At late times there is little change in the size of the domains. Figures 38 and 39 show $\text{Log}_{10}(L)$ and L as functions of $\text{Log}_{10}(\text{time})$ respectively, in both cases at late times there is a freezing of the growth.

This freezing of the growth in the 260Å film and in the 710Å film at temperatures close to T_c , might be due to domain walls becoming pinned at the surfaces or may be connected with the strain in the crystal.^(72,109) The strain is largest in the 260Å film and is a function of temperature. Changes in strain might explain the 710Å films temperature dependence.

By using the minimum resolution correction the slowing down is emphasized. The slowing down is still present if a larger correction is used, however, the absolute freezing is not as apparent. The raw uncorrected widths for the quenches on the 260Å film are still slightly changing at the end of the experiment.

Scaling and System Dimension

From equation 2.20 it can be seen that the scaling law for $S(Q)$ can indicate the dimensionality of the system. To determine the effective dimension for growth in the 260Å and 710Å films one would plot $S(Q) \cdot \sigma^d$ vs. Q/σ for $d=2$ and 3 for several times, then the plot that showed scaling would indicate the dimension. A consideration of the instrumental resolution shows that an uncorrected σ should be used, However, there is still one effect of instrumental resolution that must be considered, whether or not the instrumental resolution integrates over one or more dimensions. In the following it has been assumed that the instrumental resolution normal to the scattering plane integrates over that dimension. Estimates for the

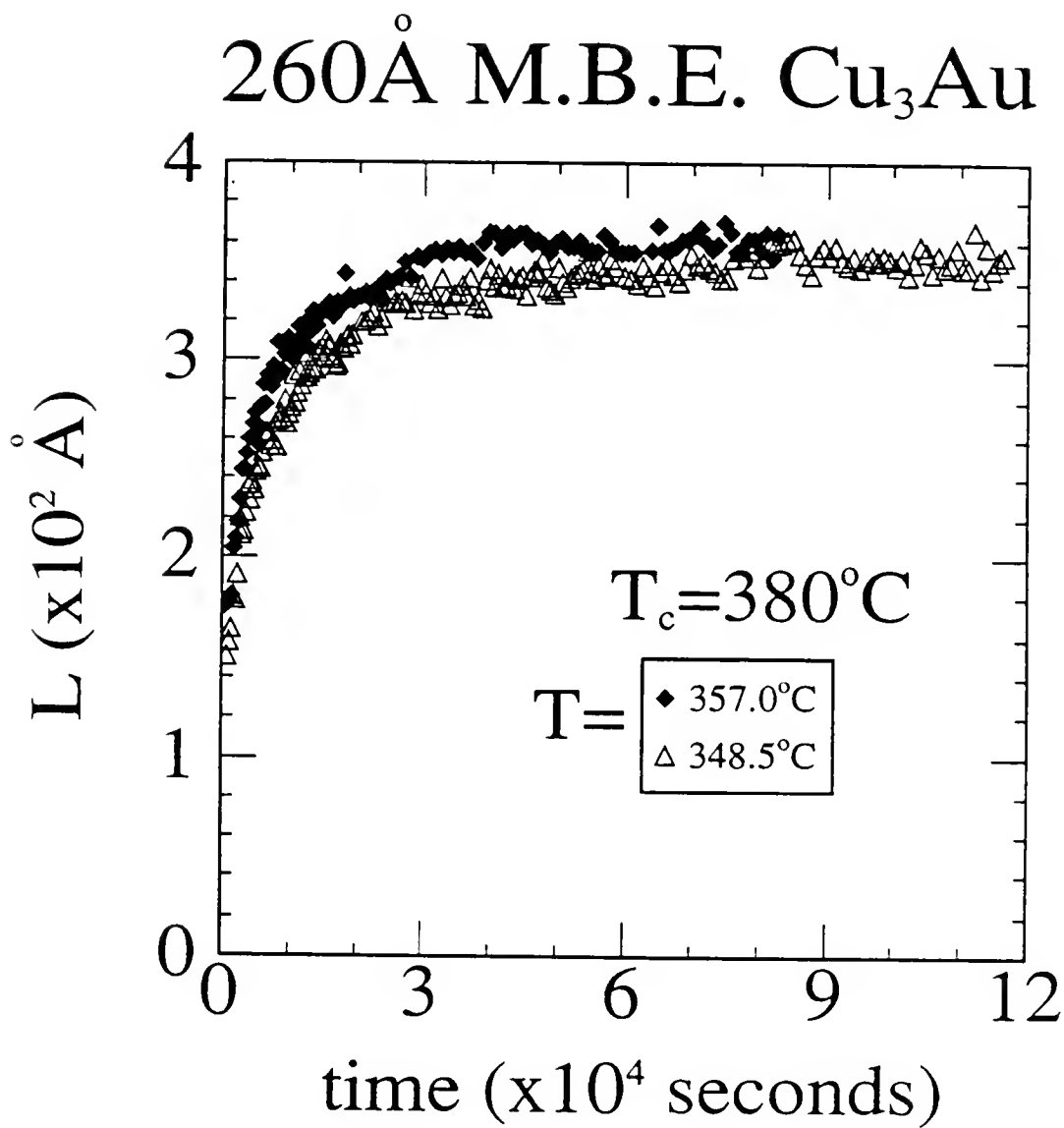


FIG. 37. Size of a domain $L=2\pi/\Gamma$ vs. time for the 260\AA M.B.E. film of Cu_3Au .

260Å M.B.E. Cu₃Au

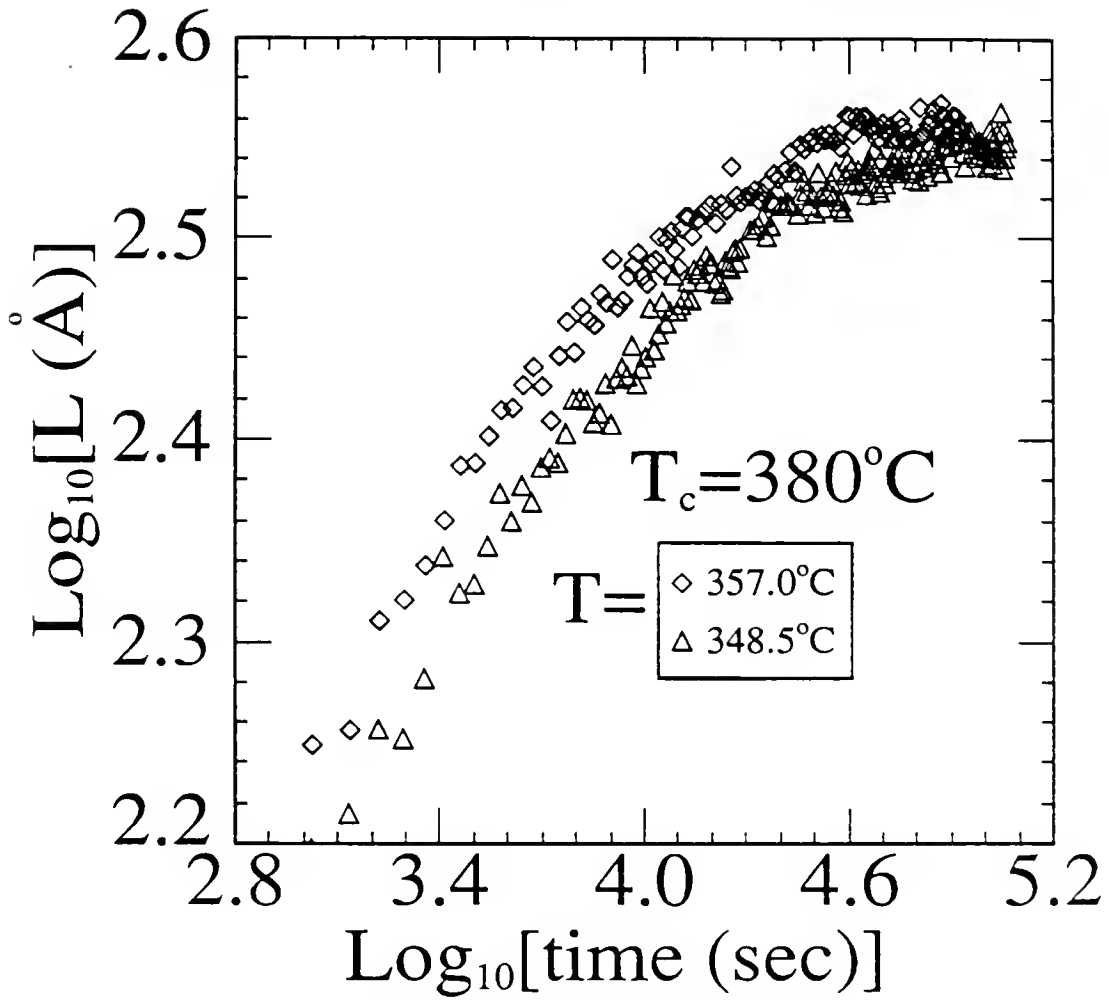


FIG. 38. Log₁₀[$L=2\tau/\Gamma$] vs. Log₁₀[time] for the 260Å M.B.E. film of Cu₃Au. Early time slope is 0.35. Late time slopes are slightly above zero.

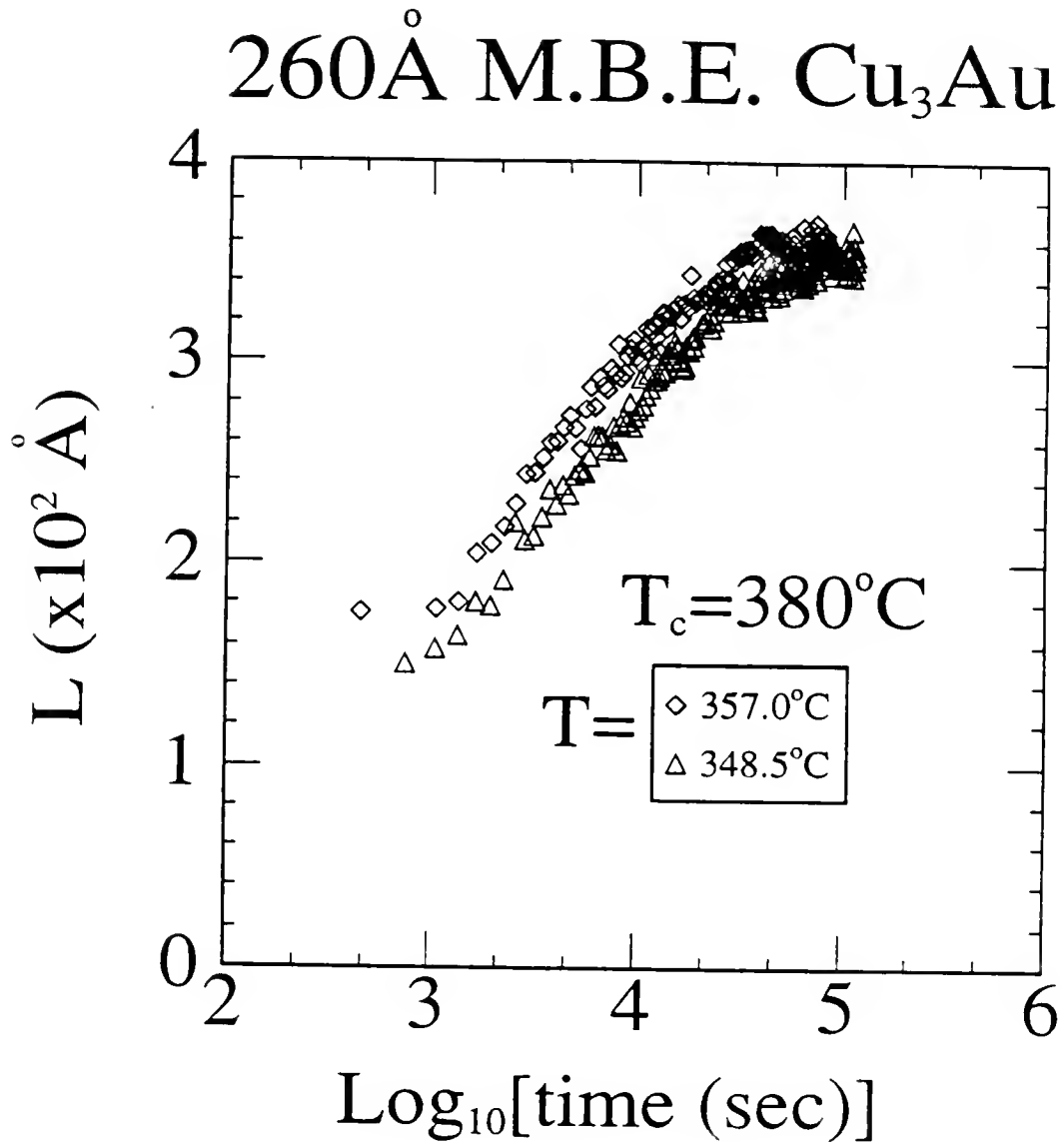


FIG. 39. Size of a domain $L=2\pi/\Gamma$ vs. $\text{Log}_{10}[\text{time}]$
for the 260\AA M.B.E. film of Cu_3Au .

260Å film indicate that at least at late times the assumption is valid. The width due to strain being smaller for the 710Å film strengthens the assumption for that system.

Figures 40 and 41 show $S(Q) \cdot \sigma^2$ and $S(Q) \cdot \sigma$ vs. Q/σ respectively for a quench to $T_c - 21.5^\circ\text{C}$ on the 710Å film. Figure 40 clearly indicate three dimensional behavior relative to the 2 dimensional scaling attempt shown in figure 41. The corresponding plots for a quench to $T_c - 31.5^\circ\text{C}$ on the 260Å film are in figures 42 and 43. For comparison the raw unscaled scans are shown in figure 44. An initial observation suggests that the growth in the 260Å film is 2 dimensional. However, there are several factors that make the difference unclear. First, the spread of the scaled plots at the peak position is smaller for the 3 dimension scaling. Second, if only times after half an hour are considered the 3 dimensional plot looks considerably better which might be due to the assumption about integrating over one dimension only being true at later times. Three, any error in the fitted width would more important in the 3 dimensional case.

Figures 45 and 46 show weak scaling (dividing counts by fitted amplitude) as well as data scaled by the corrected widths. These plots might incorrectly be interpreted as indicating two dimensional growth in the thinnest film. However the difference probably arises from instrumental resolution and strain (see table 4). From the weak scaling plots it can be concluded that the background subtraction that was made in all the scaling plots does not contribute difficulty in deciding on the dimension for the 260Å film. The fact that the scaling in the 710Å film is clearly 3 dimensional compared to being unclear in the 260Å film suggests that there is a difference in the dimensionality of the scaling between the two. Additional support for the two dimensional case is found in $L(t)$ which for the 260Å film, unlike in the others, is larger than the film thickness at late

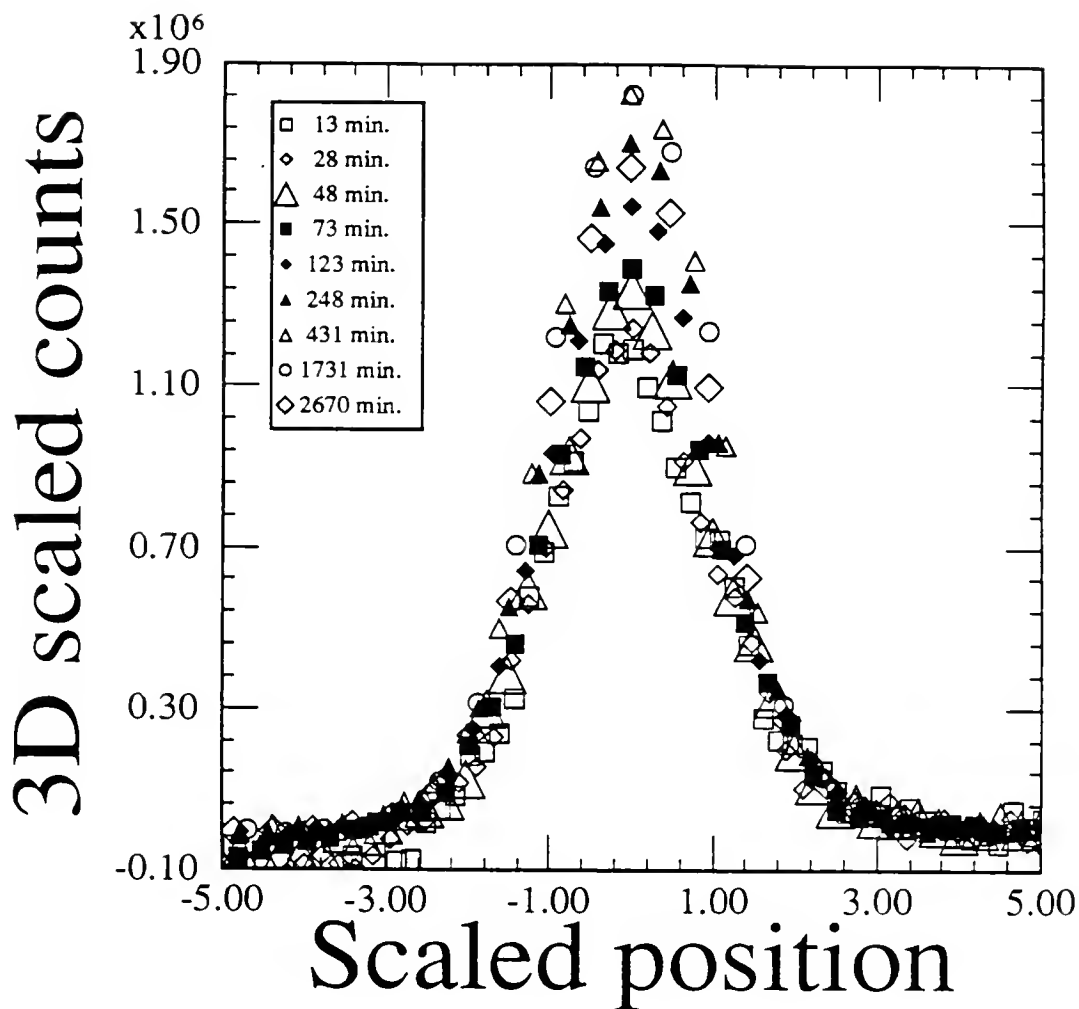


FIG. 40. 3D scaled counts vs. scaled position $(x-x_0)/\sigma_{\text{measured}}$
 $(\text{counts} \cdot \sigma^2)$ for $S(Q)$ of the 710Å M.B.E. film at a few
 selected times.

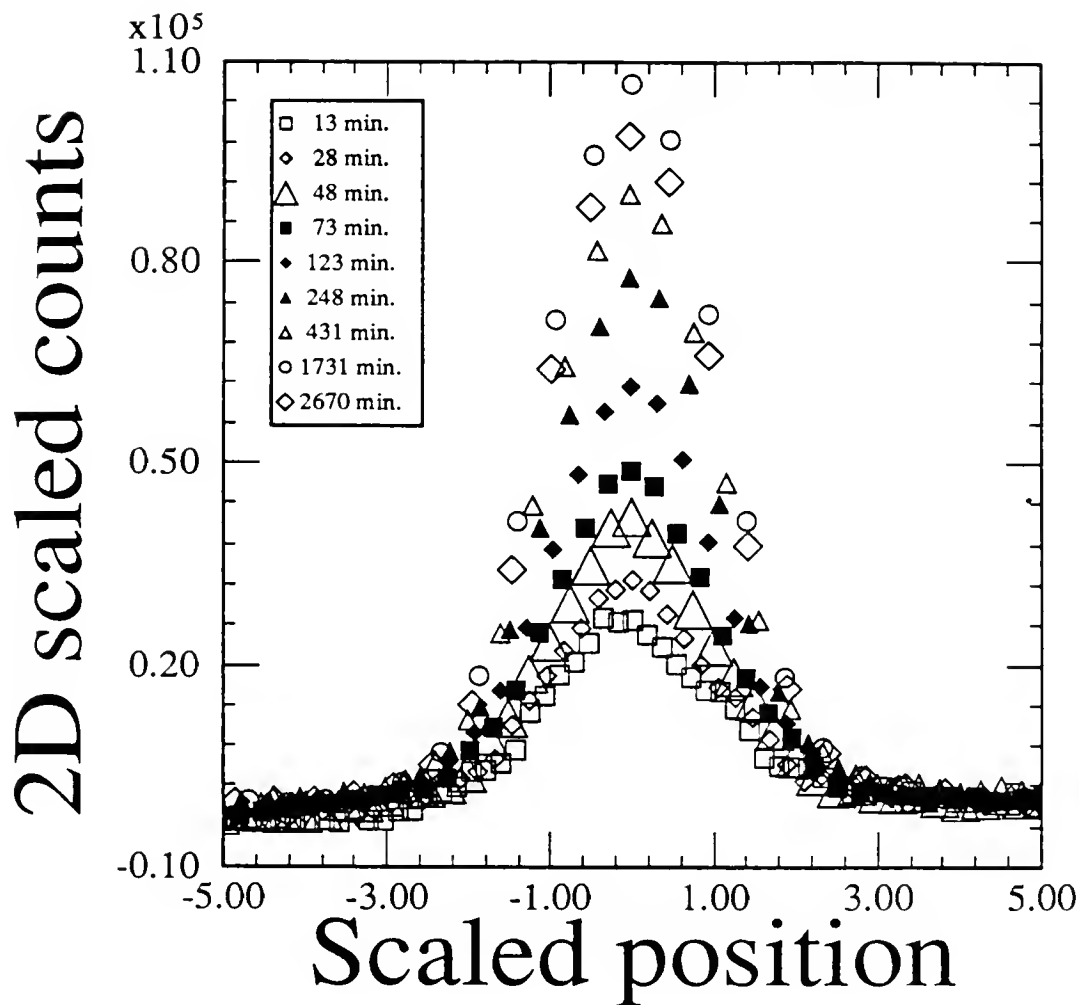


FIG. 41. 2D scaled counts vs. scaled position $(x-x_0)/\sigma_{\text{measured}}$
 (counts $\cdot \sigma$) for scans of $S(Q)$ on the 710 Å M.B.E. film for
 a few selected times.. Plot shows 2D scaling does not work.

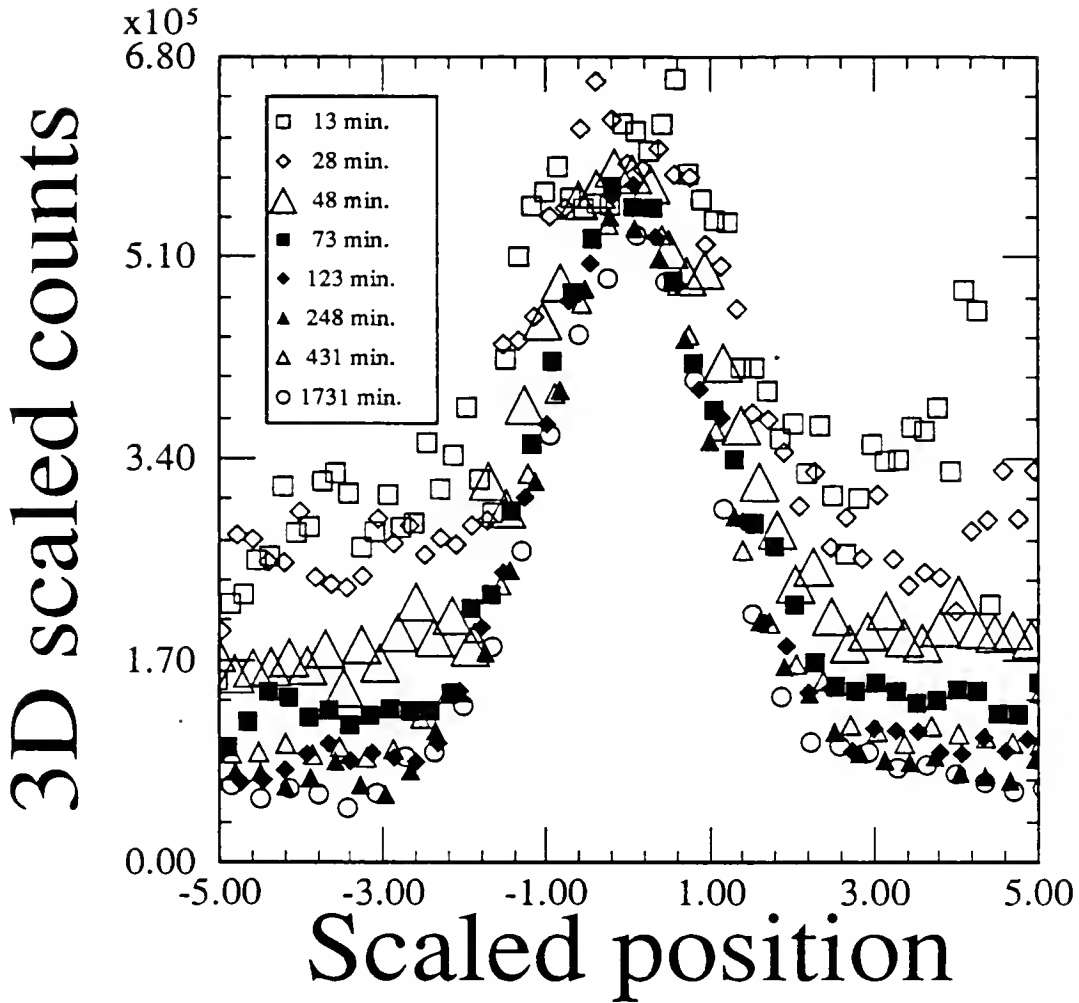


FIG. 42. 3D scaled counts vs. scaled position $(x-x_0)/\sigma_{\text{measured}}$
 $(\text{counts} \cdot \sigma^2)$ for scans of $S(Q)$ on the 260\AA M.B.E. film
 at a few selected times.

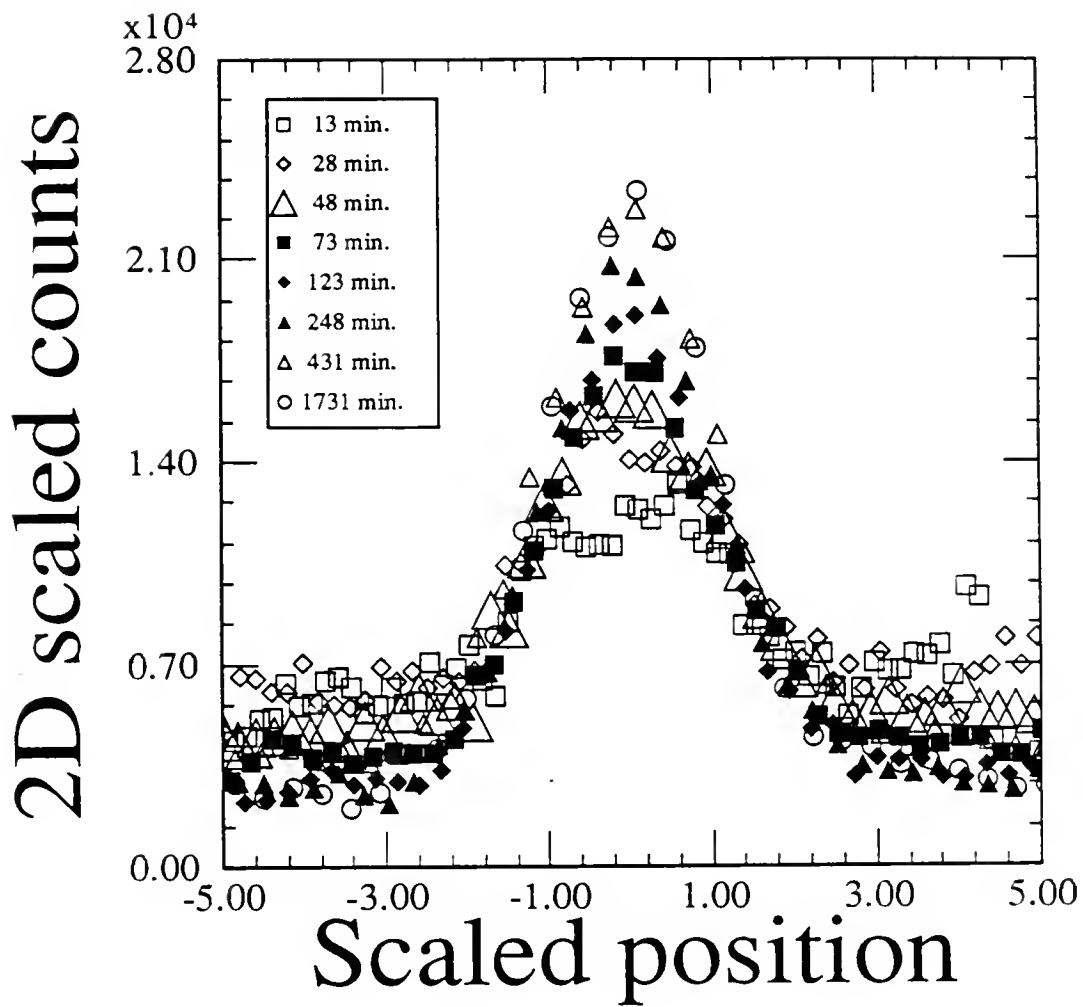


FIG. 43. 2D scaled counts vs. scaled position $(x-x_0)/\sigma_{\text{measured}}$ (counts $\cdot \sigma$) for scans of $S(Q)$ on the 260 Å M.B.E. film at the selected times.

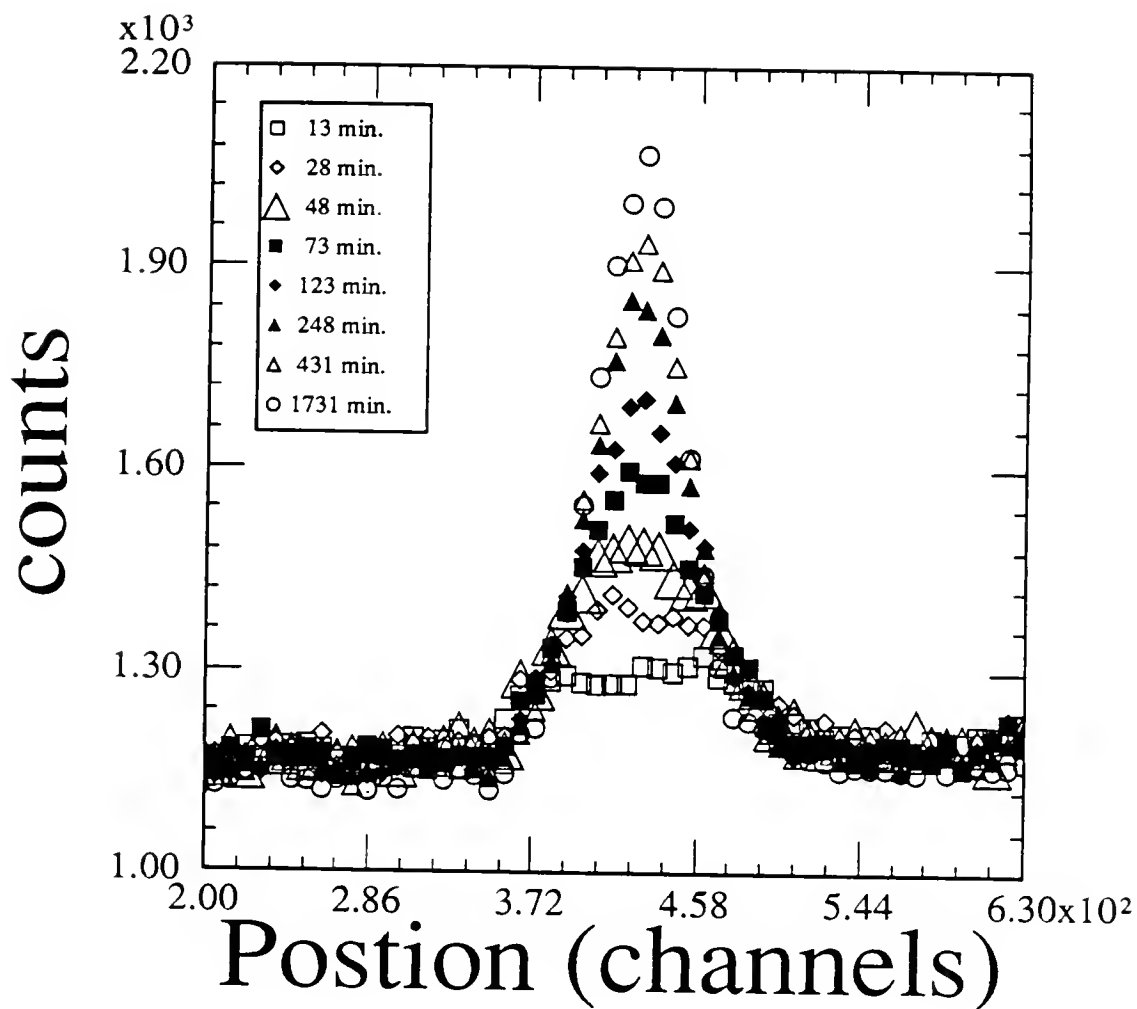


FIG. 44. Counts vs. raw uncorected, unscaled position (PSD—channels) for the 260 Å M.B.E. film at the selected times.

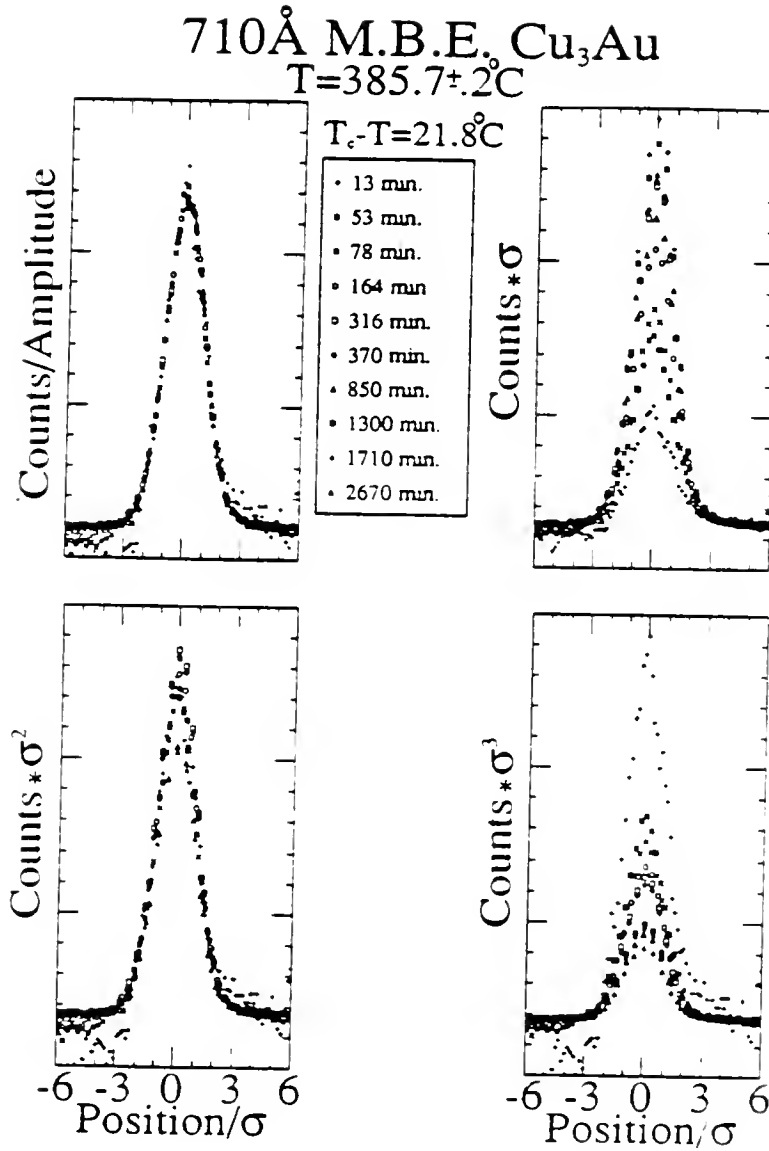


FIG. 45. Counts scaled by; fitted amplitude and $(\text{counts} \cdot \sigma_{\text{corrected}}^n)$

scaled position $(x-x_0)/\sigma_{\text{measured}}$ for the 710\AA M.B.E. film at a few selected times. Scaling by the corrected width is known to be incorrect.

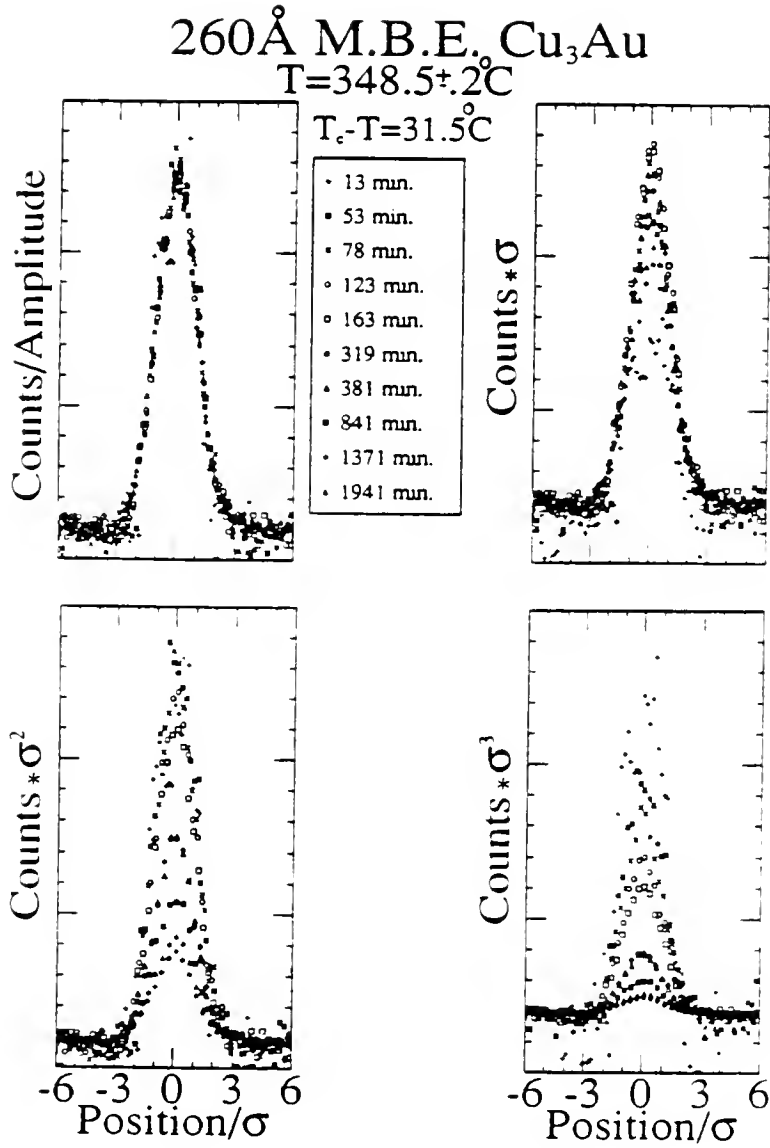


FIG. 46. Counts scaled by; fitted amplitude and $(\text{counts} \cdot \sigma_{\text{corrected}}^n)$

vs. scaled position $(x - x_0)/\sigma_{\text{measured}}$ for the 260 Å M.B.E. film at a few selected times. Scaling by the corrected width is known to be incorrect. The apparent 2D growth is known to be a resolution effect.

times (see figure 37). It is reasonable to assume that at early times the scaling in the 260\AA is three dimensional and that at some late time it crosses over to two a dimensional system. This may account for some of the confusion in the scaling. Unfortunately the larger effective resolution lessens the change in the uncorrected widths so that at late times the raw widths do not change nearly as much as at early times.

A Brief Look at the Early Time Behavair of the Bulk Single Crystal

Figure 47 shows some raw scans of the bulk sample of Cu_3Au taken at National Synchrotron Light Source (NSLS) at Brookhaven National Laboratory (BNL). The scans were collected using a silicon diode array PSD made by Princeton Applied Research (PAR). The experimental set-up was similar to that used for the radial data collected at The University of Florida as depicted in figure 10, only the synchrotron replaces the rotating anode as the x-ray source. The instrumental resolution associated with this early time data is much less than the width of the peaks for all of the data shown here. The quench took 15 seconds using the automated quenching described in connection with the M.B.E. films. One second scans were taken for 500 seconds starting at the beginning of the quench. It was expected that these early time scans would be gaussian, however, they are LSQ. The LSQ shape may be due to the sample having been ordered for a week before going to BNL. Although the history dependence of the line shape crossover was already known, it was not known that the effect could be eliminated to this extent.

A plot of Amplitude vs. time is shown in figure 48. At about 125 seconds the amplitude rapidly increases in a linear fashion. A plot of the $\text{Log}_{10}(\text{width})$ vs. $\text{Log}_{10}(\text{time})$, shown in figure 49 displays a sharp change in slope from nucleation to

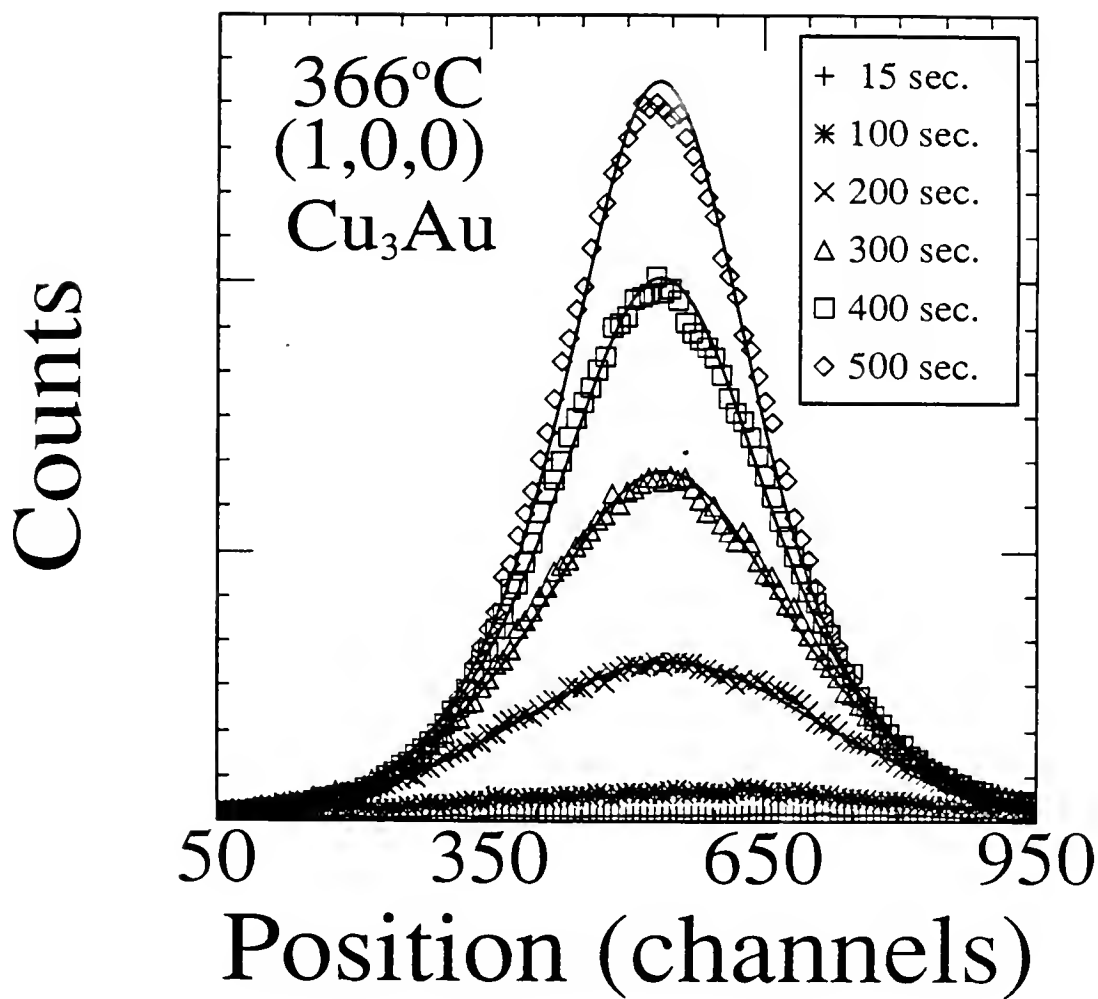


FIG. 47. Uncorrected scans of the $[0,1,0]$ of bulk Cu_3Au . Each scan was collected in one second on X-20C at BNL. Solid lines are LSQ fits.

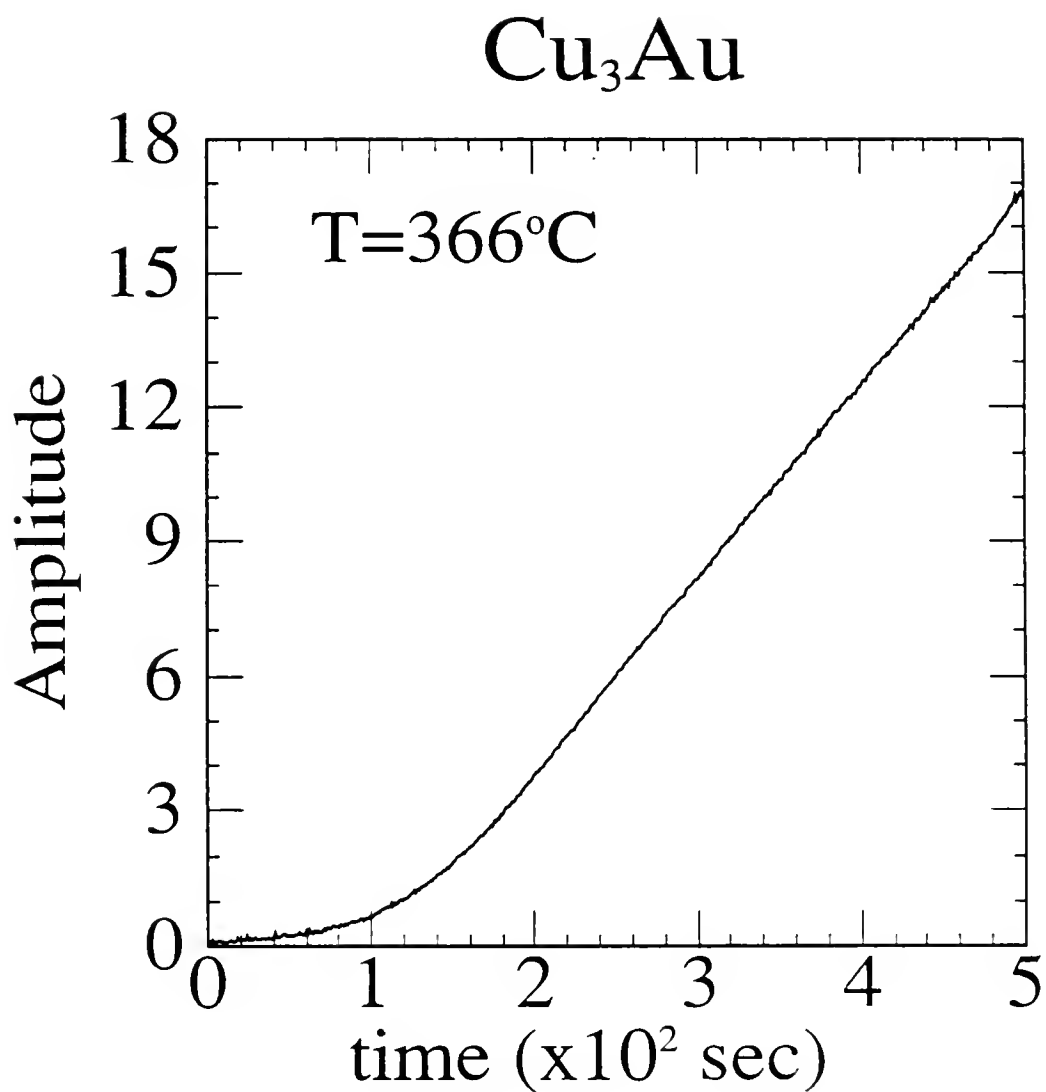


FIG. 48. LSQ fitted amplitude of the $[0,1,0]$ of bulk Cu_3Au vs. time. Each data point represents one second.

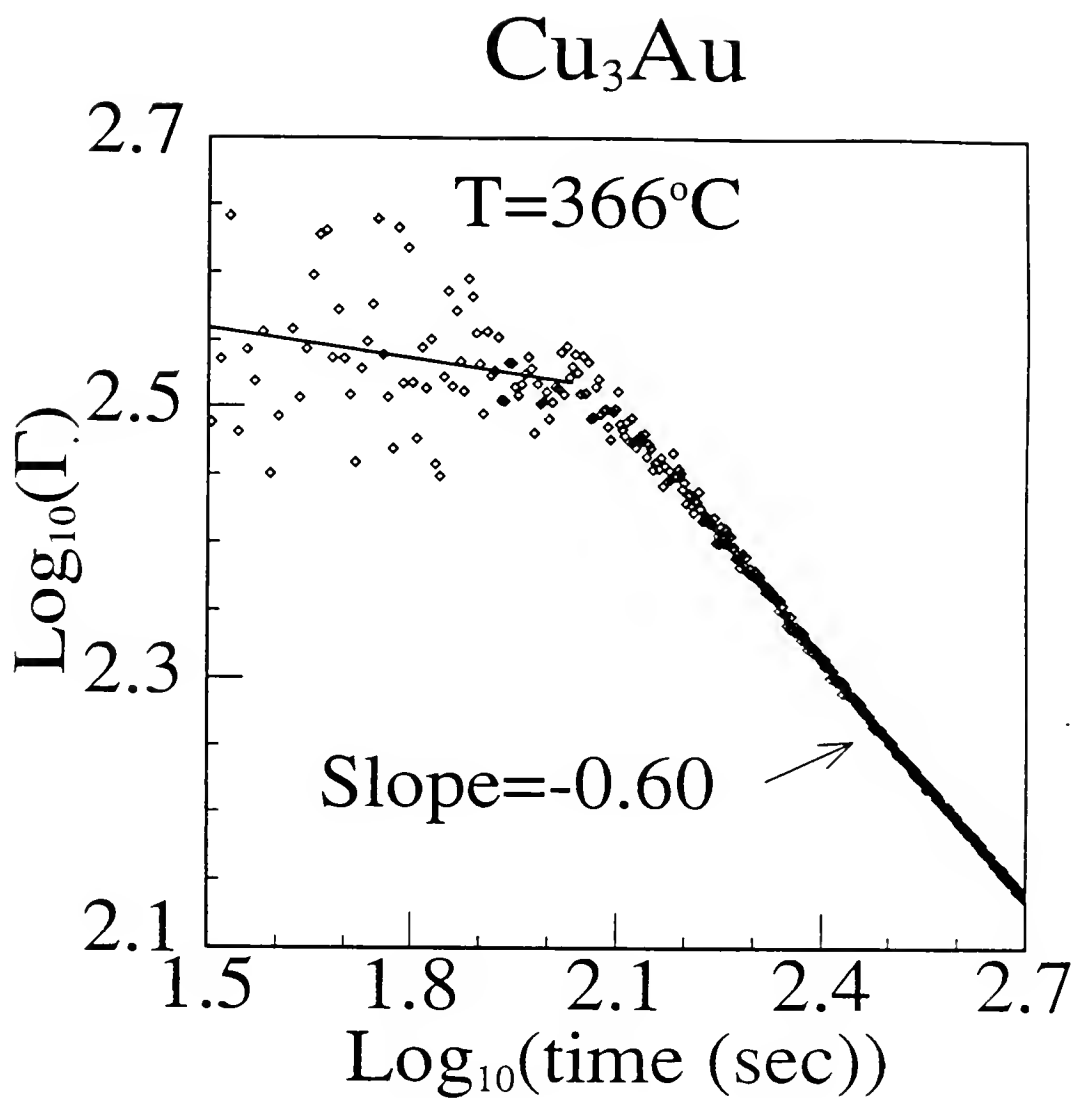


FIG. 49. Log_{10} [LSQ fitted width] of the $[0,1,0]$ of bulk Cu_3Au vs. Log_{10} [time].

growth also at 125 seconds. Figure 50 is a plot of the integrated intensity ($\text{amp} \cdot \Gamma$). It is somewhat surprising that this curve is concave down after the onset of critical nucleation. From similar plots showing the late time data (figure 18) it is known that the integrated intensity saturates at a much later time, indicating that the up turn at the end of the plot is real. This effect is an indication that two different types of nucleation are likely to be involved.

The integrated intensity is expected to follow the rule⁽¹⁾

$$I = I_{\infty} \left[1 - \exp \left[-[(t - t_0)/\tau]^m \right] \right] \quad (4.5)$$

where I_{∞} is the maximum obtainable intensity, τ is a rate constant, t_0 represents a nucleation time, and m is an integer that depends on the type of nucleation involved.

$$m = \begin{cases} 4 & \text{homogeneous} \\ 3 & \text{impurities} \\ 2 & \text{surface} \end{cases}$$

If two types of nucleation are involved then it may be possible that the initial increase in intensity is due to surface (or impurity site) nucleation with a short nucleation period t_0 . This early nucleation would soon be swamped by homogeneous nucleation. This scenario would lead to an intensity corresponding to the sum of two equations of the form of 4.5, each with different values for I_{∞} , t_0 , and τ .

Another unexpected discovery made at NSLS is the existence of satellites at $[0,0.9,0]$ and $[0,1.1,0]$. These satellites are shown in figure 51. They are found in the radial direction, but not in the transverse direction, suggesting that they are connected with type 2 domain walls. Similar satellites have been found in the CuAu system which also has an order-disorder transition.⁽¹⁰⁹⁾ The satellites in Cu_3Au behave similar to those in CuAu. The satellites appear and then grow in intensity after a quench as the main peak grows, but as the integrated intensity of the main

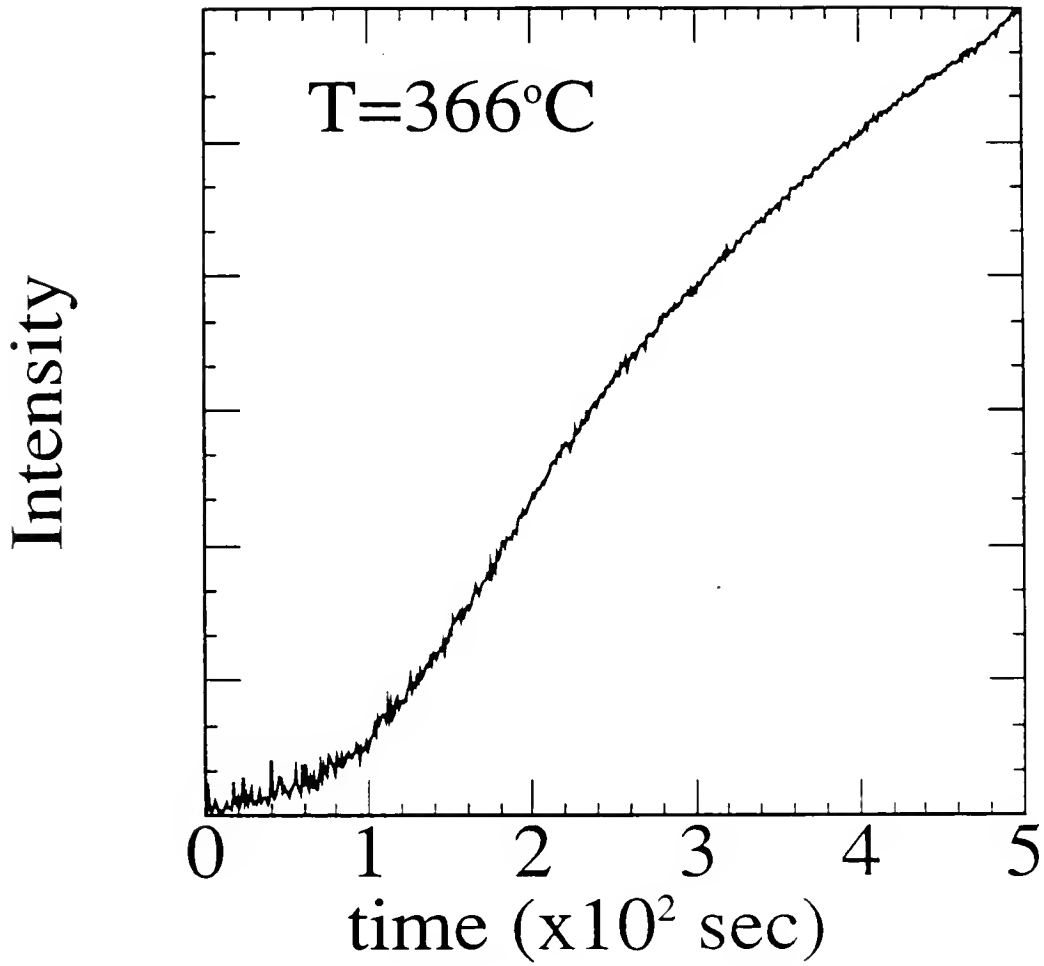
Cu_3Au 

FIG. 50. Integrated intensity [amp·width] of the [0,1,0] of bulk Cu₃Au vs. time.

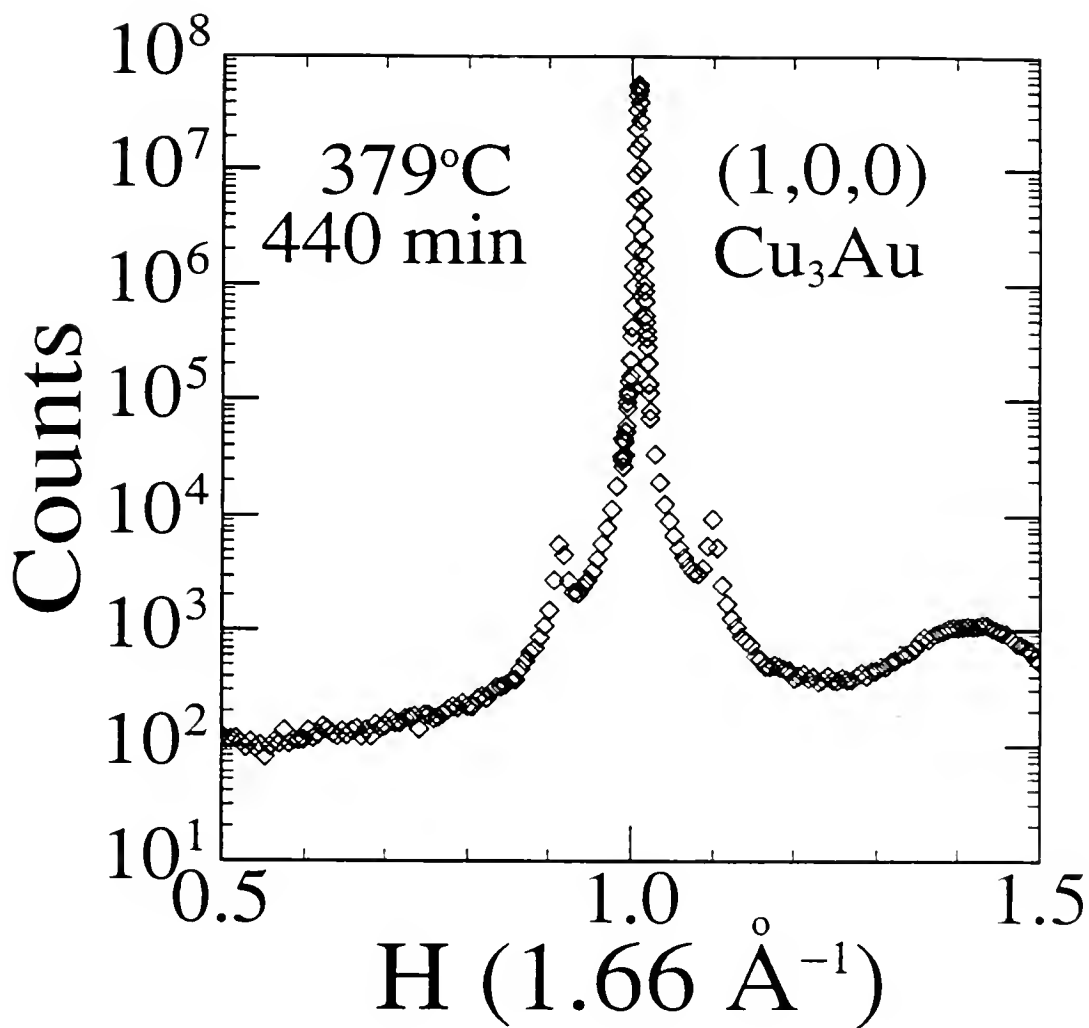


FIG 51. Radial scan of the bulk Cu_3Au sample showing the satellites found at $[0,0.9,0]$ and $[0,1.1,0]$.

peak (the $[1,0,0]$) saturates the satellites decay. The satellites do not appear in quenches to 20°C or more below T_c . The satellites in CuAu result from domain walls forming periodically every 5 lattice constants, creating a super domain of length 10 lattice constants.⁽¹¹⁰⁾ The satellites in Cu_3Au may be due to the same phenomena, arising from a AuCu type structure forming in type 2 walls or at the surface.^(112,113) Satellites have also been observed in alloys of composition near Cu_3Au ^(114,115,116) which are believed to arise from a modulation of the density inside each domain. Furthermore, the satellites seen in off-stoichiometric samples are found in a direction which would associate them with type 1 walls. The existence of satellites in off-stoichiometric Cu_3Au suggests that it is the offstoichiometric nature of type 2 walls that produces our satellites. Our satellites association with type 2 walls has interesting implications to the early time behavior for example, they strengthen the assertion that scaling is not valid between early and late times. A more detailed analysis of this synchrotron data is planed for the near future and is mentioned here in part as an indication of future directions, and in part for completeness.

CHAPTER 5 CONCLUSIONS

Current Results

The development of order in the bulk single crystal Cu_3Au sample after a thermal quench, from the disordered state exhibits three distinct regimes, nucleation, ordering, and coarsening. The first is characterized by a gaussian structure factor associated with short-range order. At the beginning of the ordering regime the shape is gaussian but quickly crosses over becoming rapidly more lorentzian-squared with time. At the onset of coarsening the structure factor is very well described by a lorentzian-squared function. During coarsening, domain growth is consistent with a curvature-driven growth law for both type-1 and type-2 walls. Moreover, the power "a" associated with this growth has been found to be 0.5 to a high degree of accuracy in the radial direction and to a lesser degree in the transverse direction, implying that scaling during coarsening is valid in an anisotropic system. However, the change in line shape clearly shows that $S(\mathbf{q},t)$ can only be scaled during coarsening and not during ordering. This fact is easily seen by viewing the disordered phase as a thick domain wall, in which case the size of the wall relative to the ordered domain size would be different for different times so that scaling would not exactly recreate the state of the system. Our data is qualitatively described by the theory recently put forth by Z. Lai based on a three component order parameter. This theory produces a slightly modified lorentzian-squared structure factor at late times and a gaussian shape at early times. Although a

change in the line shape exists in Lai's theory the history dependence of this change is not explained. However, the level of short-range order and its effect on nucleation is likely to play an essential role in explaining the history dependence. It is possible that a previously well ordered sample which has been disordered close to the transition temperature (within $\approx 30^{\circ}\text{C}$) has a more homogeneous nucleation. If nucleation takes place throughout the sample with a high density of nucleation sites, then the system would reach coarsening very rapidly and have a short ordering regime.

Ordering in an off-stoichiometric sample is slower than in a stoichiometric one. The extra atoms in an off-stoichiometric sample behave like diffusive impurities, giving rise to a logarithmic like time dependence.

It was hoped that the data on the M.B.E. films would show a clear crossover to two dimensional growth. However, it is unclear whether an effective two dimensional stage was reached or not. The physics involved in the M.B.E. films is probably dominated by the strain which gives rise to a slower type of growth at late times. This slower growth rate in the M.B.E. films has a temperature dependence such that at late times the power of the time dependence is lower for higher temperatures. In fact, the power of the time dependence at late times becomes almost zero for the 710\AA film as the temperature approaches T_c . This temperature dependence could be related to strain in the film being greater at higher temperatures. Another trend is that the thinner the film the lower the power of the time dependence for a given temperature, but this too is probably due to greater strain for thinner films.

Future Directions

As discussed at the end of chapter 6, the history dependence of the line shape crossover is not understood. Its likely connection with the nucleation process is an interesting problem that may broaden our understanding of how short range order effects the transition. In addition, there seems to be a void of information regarding the ordering stage. Nucleation in general has been studied in many systems, as well as domain coarsening, yet it is the ordering stage that does not obey scaling laws. Further investigation into this intermediate stage would be useful. An investigation of the satellites found in the radial direction about the $[0,1,0]$ may provide some insights. The effects of stoichiometry in a bulk single crystal on both types of walls could also have some useful information.

APPENDIX A THE EFFECT OF TYPE 1 WALLS ON SCATTERING

The width of a superlattice peak is of course greatly affected by the existence of domain walls. Assuming the half diagonal glide domain boundaries perpendicular to each of the axes are completely independent from each other the structure factor for the $m_1 m_2 m_3$ ordered cell is,⁽⁹⁰⁾

$$F(m_1 m_2 m_3) = F \exp[i\phi(m_1 m_2 m_3)] \quad (\text{A.1})$$

where F is from 3.25.

$$F = f_{Au} + f_{Cu} \{ \exp[\pi i(h+k)] + \exp[\pi i(k+l)] + \exp[\pi i(l+h)] \}$$

The phase $\phi(m_1 m_2 m_3)$ accounts for cells in different ground states. This phase factor has four possible values, $[0, \pi(h+k), \pi(k+l), \pi(l+h)]$, related to the four displacements $[0, (a_1+a_2)/2, (a_2+a_3)/2, (a_3+a_1)/2]$. For the structure factor F the intensity is given $F^* F$. After summing over all cells one finds,

$$I = F \sum_{m_1 m_2 m_3} \exp[i\phi(m_1 m_2 m_3)] \exp[i(k-k') \cdot (m_1 a_1 + m_2 a_2 + m_3 a_3)] \quad (\text{A.2})$$

$$\cdot F^* \sum_{m'_1 m'_2 m'_3} \exp[-i\phi(m'_1 m'_2 m'_3)] \exp[-i(k-k') \cdot (m'_1 a_1 + m'_2 a_2 + m'_3 a_3)]$$

Rewriting $(k-k')$ as $[(h+h_1)b_1 + (k+h_2)b_2 + (l+h_3)b_3]$ where $[h_1 b_1 + h_2 b_2 + h_3 b_3]$ is the departure of the tip of the diffraction vector from the point $[h, k, l]$. The intensity is now written,

$$I = F^* F \sum_{m_1 m_2 m_3} \sum_{m'_1 m'_2 m'_3} \exp\{i\phi[(m_1 m_2 m_3) - (m'_1 m'_2 m'_3)]\} \cdot \exp\{2\pi i[(m_1 - m'_1)h_1 + (m_2 - m'_2)h_2 + (m_3 - m'_3)h_3]\}. \quad (A.3)$$

Defining $n_i = m_i - m'_i$ and $\phi(n_1 n_2 n_3) = \phi(m_1 m_2 m_3) - \phi(m'_1 m'_2 m'_3)$ one of the sums may be eliminated by combining terms with the same value of $n_1 n_2 n_3$, along with introducing an average phase factor and multiplying by the number of terms, $N(n_1 n_2 n_3)$.

$$I(h_1 h_2 h_3) = F^2 \sum_{n_1} \sum_{n_2} \sum_{n_3} N(n_1 n_2 n_3) \langle \exp(i\phi(n_1 n_2 n_3)) \rangle \exp[2\pi i(n_1 h_1 + n_2 h_2 + n_3 h_3)] \quad (A.4)$$

The three sets of perpendicular anti-phase boundaries are independent, hence, $\langle \exp[i\phi(n_1 n_2 n_3)] \rangle = \langle \exp[i\phi(n_1)] \rangle \langle \exp[i\phi(n_2)] \rangle \langle \exp[i\phi(n_3)] \rangle$. The phase difference between distant cells is the sum of the phases between all the cells on a line connecting them. Mathematically,

$$\phi(n) = \phi(1-0) + \phi(2-1) + \dots + \phi[n-(n-1)] \quad (A.5)$$

Therefore, $\langle \exp[i\phi(n)] \rangle = \langle \exp[i\phi(1)] \rangle^{|n|}$. There are only two possible values for $\phi(1)$ along the a_1 direction, $\phi(1) = \pi(k+1)$ with probability a and $\phi(1) = 0$ with probability $1-a$. The probability a is that of crossing an anti-phase domain boundary in a distance $|a|$. Therefore, along the a_1 direction,

$$\begin{aligned} \langle \exp[i\phi(1)] \rangle &= (1-a) + a \cdot \exp[\pi i(k+1)] \\ &= 1 - 2a \sin^2[\pi(k+1)] \end{aligned} \quad (A.6)$$

Summing over n_1 the phase factor takes on two values, 1 if $k+1$ is even and $(1-2a)^{|n_1|}$ if $k+1$ is odd. The same logic applies to n_2 with $l+h$ and n_3 with $h+k$.

For fundamental reflections the sums $(h+k)$, $(k+l)$, and, $(l+h)$ are even and no effect is produced. For superlattice peaks, two of the indices $[h, k, l]$ are of the same parity and the other one is different. For convenience the convention that all superlattice peaks be written such that h and l have the same parity will be

adopted. The intensity with this convention simplifies to,

$$I(h_1 h_2 h_3) = F^2 \sum_{n_1} \sum_{n_2} \sum_{n_3} N(n_1 n_2 n_3) (1-2a)^{|n_1|} (1-2a)^{|n_3|} \exp[2\pi i(n_1 h_1 + n_2 h_2 + n_3 h_3)]. \quad (\text{A.7})$$

For very small $n_1 n_2 n_3$, $N(n_1 n_2 n_3) \cong N_1 N_2 N_3$. The factors $(1-2a)^{|n_1|}$ and $(1-2a)^{|n_3|}$ make only small values of $|n_1|$ and $|n_3|$ important. Consequently $N(n_1 n_2 n_3)$ can be approximated by $N_1(N_2 - |n_2|)N_3$.⁽⁹⁰⁾ Equation A.7 is now expressed as three independent products.

$$I(h_1 h_2 h_3) = F^2 \left[N_1 \sum_{n_1} (1-2a)^{|n_1|} \exp(2\pi i n_1 h_1) \sum_{n_2} (N_2 - |n_2|) \exp(2\pi i n_2 h_2) N_3 \sum_{n_3} (1-2a)^{|n_3|} \exp(2\pi i n_3 h_3) \right] \quad (\text{A.8})$$

Now consider the sum over n_2 . This sum is equivalent to a product of sums.

$$\begin{aligned} & \sum_{n_2 = -N_2}^{+N_2} (N_2 - |n_2|) \exp(2\pi i n_2 h_2) \\ &= \sum_{m_2=0}^{+N-1} \exp(2\pi i m_2 h_2) \sum_{m'_2=0}^{+N-1} \exp(-2\pi i m'_2 h_2) \end{aligned} \quad (\text{A.9})$$

The sums over m_2 and m'_2 have a geometric progression of the form,

$$a + ar + ar^2 + \dots + l = \frac{r l - a}{r - 1} \quad (\text{A.10})$$

Summing over m_2 and m'_2 in this way yields,

$$\begin{aligned} & \frac{\exp(2\pi i N_2 h_2) - 1}{\exp(2\pi i h_2) - 1} \cdot \frac{\exp(-2\pi i N_2 h_2) - 1}{\exp(-2\pi i h_2) - 1} \\ &= \frac{2 - 2\cos(2\pi N_2 h_2)}{2 - 2\cos(2\pi h_2)} = \frac{\sin^2(\pi N_2 h_2)}{\sin^2(\pi h_2)} \end{aligned} \quad (\text{A.11})$$

Returning to the sums over n_1 and n_3 , both of which are of the form,

$$\begin{aligned}
 & \sum_{n=-\infty}^{\infty} (1-2a)^{|n|} \exp(-2\pi n h) \\
 &= 1 + \sum_{n=1}^{\infty} [(1-2a)\exp(2\pi i h)]^n + \sum_{n=1}^{\infty} [(1-2a)\exp(-2\pi i h)]^n \\
 &= 1 + \frac{(1-2a)\exp(2\pi i h)}{1-(1-2a)\exp(2\pi i h)} + \frac{(1-2a)\exp(-2\pi i h)}{1-(1-2a)\exp(-2\pi i h)} \\
 &= \frac{a(1-a)}{a^2 + (1-2a)\sin^2(\pi h)}. \tag{A.12}
 \end{aligned}$$

Making the final approximation that h_1 , h_2 , and h_3 are small the intensity is given by,⁽⁹⁰⁾

$$I(h_1 h_2 h_3) = F^2 \frac{N_1 a}{a^2 + (\pi h_1)^2} \frac{\sin^2(\pi N_2 h_2)}{(\pi h_2)^2} \frac{N_3 a}{a^2 + (\pi h_3)^2}. \tag{A.13}$$

The intensity for a superlattice peak as given above is roughly a thin disk lying in the $h_1 h_3$ plane with a thickness determined by the crystal dimension $N_2 a_2$. Type 2 walls would, of course thicken the disk. Figure 8 shows the orientations of these disks for one plane of reciprocal space. Also this equation shows that the radius of the disk increases with the probability a of anti-phase boundaries.

Normally the condition $I(h_1 h_2 h_3)$ equal $(1/2)I(h_1 h_2 h_3)$ would be used to define the width of the peak in terms of a ($a \propto L$). However, the approximation of $h_1 h_2 h_3$ being small lead to problems. Therefore, one starts with a more general equation for the width.⁽⁹⁰⁾

$$\text{FWHM} \propto \frac{\int_{-\infty}^{\infty} I \, dt}{I_{\max}} \tag{A.14}$$

Although the integrated intensity is greatly affected by the amount of order vs. disorder it is not affected by the existence of sharp domain walls. Hence, the integrated intensity must be $F^2 N_1 N_2 N_3$. Considering $I(h_1 h_2 h_3)$ as defined in

equation A.8 with the same approximations for n_2 as before we have,

$$I(h_1 h_2 h_3) = F^2 \left[N_1 \sum_{n_1=0}^{\infty} (1-2a)^{|n_1|} \exp(2\pi i n_1 h_1) \cdot N_3 \sum_{n_3=0}^{\infty} (1-2a)^{|n_3|} \exp(2\pi i n_3 h_3) \cdot \frac{\sin^2(\pi N_2 h_2)}{(\pi h_2)^2} \right] \quad (A.15)$$

The intensity is a maximum at $h_1=h_2=h_3=0$. So that A.15 becomes,

$$I(h_1 h_2 h_3) = F^2 N_1 N_2 N_3 \sum_{n_1=0}^{\infty} (1-2a)^{|n_1|} \sum_{n_3=0}^{\infty} (1-2a)^{|n_3|} \quad (A.16)$$

where,

$$\lim_{h_2 \rightarrow 0} \frac{\sin^2(\pi N_2 h_2)}{(\pi h_2)^2} = N_2. \quad (A.17)$$

Expressing $n_1 a_1$ and $n_3 a_3$ in terms of a distance (s) along the disk,

$$\begin{aligned} n_1 a_1 &= 2\pi s h / \sqrt{h^2 + k^2 + l^2} \\ n_3 a_3 &= 2\pi s l / \sqrt{h^2 + k^2 + l^2} \end{aligned} \quad (5.18)$$

we can write,

$$|n_1| + |n_3| = \frac{2\pi |s| (|h| + |k|)}{a \sqrt{h^2 + k^2 + l^2}} \equiv \beta |s|. \quad (A.19)$$

Converting the sums over n_1 and n_3 into an integral over (s) gives,

$$I_{\max} = F^2 N_1 N_2 N_3 \int_{-\infty}^{\infty} (1-2a)^{\beta |s|} ds \quad (A.20)$$

Substitution of A.20 into A.14 shows,

$$\text{FWHM} \propto \left[\frac{F^2 N_1 N_2 N_3}{F^2 N_1 N_2 N_3} \right] \frac{1}{\int (1-2a)^{\beta |s|} ds} = \frac{-\beta \ln(1-2a)}{2} \quad (5.21)$$

For small a , $\ln(1-2a) \simeq -2a$. The final result with $(a/a) = L$, the size of a domain is,⁽⁹⁰⁾

$$\text{FWHM} \propto a\beta = (2\pi/L) \frac{(|h| + |k|)}{\sqrt{h^2 + k^2 + l^2}} \quad (A.22)$$

This result is for type 1 walls, however, type 2 walls also produce broadening with a $2\pi/L$ dependence. The dependence, β for the $[0,1,0]$ type peak is one, and for the $[1,0,1]$ β is $\sqrt{2}$. For a given functional form equation A.14 can be used to relate a the corresponding width to L . For a gaussian width σ we have,

$$\sigma = (\sqrt{2\pi}/L) \frac{(|h| + |k|)}{\sqrt{\Gamma h^2 + k^2 + 1^2}} \quad (\text{A.23})$$

where as for a lorentzian squared width Γ ,

$$\Gamma = (\sqrt{2}/L) \frac{(|h| + |k|)}{\sqrt{\Gamma h^2 + k^2 + 1^2}}. \quad (\text{A.24})$$

The reader should be aware of the above corrections to 2.21 for type 1 walls. However, throughout this work it is assumed that 2.21 is correct for both types of walls.

APPENDIX B FUNCTIONAL DEFINITIONS USED IN FITTING

In the following, x is the position coordinate, and x_0 is the position of the peak. Here and throughout the text σ is used to represent a gaussian width and Γ a width for a lorentzian to any power. The following definitions are such that the widths will approximately equal a HWHM. The amplitude is "A".

Gaussian,

$$F(x) = A \cdot \exp \left[-[(x-x_0)/2\sigma]^2 \right] \quad (B.1)$$

Lorentzian,

$$F(x) = \frac{1}{1 + \left[(x-x_0)/\Gamma \right]^2} \quad (B.2)$$

Lorentzian squared,

$$F(x) = \left[1 + \frac{1}{2} \left[(x-x_0)/\Gamma \right]^2 \right]^{-2} \quad (B.3)$$

HT Theory,⁽⁸⁾

$$I(k) = \frac{2}{3} (f_{Au} - f_{Cu}) \sum_{i \neq j \neq l=1}^3 \Gamma_{i2} \Gamma_{j2} \Gamma_{l3} \cdot [1 + \cos(\pi k_j) - 2\cos(\pi k_l)] \quad (B.4)$$

where,

$$\Gamma_{im} = (1 - x_m^2) / [1 + x_m^2 - 2x_m \cos(2\pi k_i)]$$

$$x_2 = (1 - 2\eta - 2\gamma), \quad x_3 = (1 - 4\eta)$$

γ is the probability of finding a type 1 wall between two unit cells.

2η is the probability of finding a type 2 wall between two unit cells.

At the [0,1,0] a transverse direction is $(x,0,0)$ and $k_1 = \frac{ax}{2\pi}$, $k_2=1$, $k_3=0$

Equation B.4 then reduces to,

$$\text{Amp}\{1+C[1-\cos(a(x-x_0))]\}^{-1} \quad (\text{B.5})$$

where,

$$C=[0.5-(\eta+\gamma)^2]/(\eta+\gamma)$$

$$\text{Amp}=\text{Amp}(\eta,\gamma,f_{\text{Au}}-f_{\text{Cu}})$$

are fit parameters.

In the radial direction $k_1=0$, $k_2=\frac{a(1+x)}{2\pi}$, $k_3=0$.

This leads to;

$$I(k_2)=\text{Amp} \frac{[\cos(\pi k_2)-1]}{\{1+D[1-\cos(2\pi k_2)]\}} \quad (\text{B.6})$$

where,

$$k_2=2.4878856 \cdot \sin(0.413643\text{rad}+(x-x_0) \cdot 2.1816616 \times 10^{-4} \text{rad/PSD-channel})$$

x is in PSD channels, 0.4136 is the position of the [0,1,0] in radians, and 2.48... is a/λ
O.J.K. theory,⁽³⁵⁾

$$I(x)=\frac{2}{\pi} \cdot \frac{(2\pi)^{1.5}}{x} \int_0^{\infty} \frac{dR \ R^3 J_{3/2}(x \cdot R)}{\{x \cdot R[\exp(R^2)-1]\}^{1/2}} \quad (\text{B.7})$$

where $J_{2/3}$ is a Bessel function. In the fitting routine $x=(x-x_0)/\Gamma$ is approximated as $10.47(1-x^2)$ if the absolute value of $x < 10^{-4}$.

Copies of the fitting and numerical integration routines used can be found in Numerical Recipes in Fortran The Art of Scientific Computing, Cambridge University Press (1985).

APPENDIX C
CALIBRATION OF BRAUN OED-50-M
POSITION SENSITIVE METAL WIRE DETECTOR

After making all the four wire and two gas line connections (if they fit they are correct), open p-10 gas bottle and set pressure at 6 bar. Next, slowly turn valve at fount of "gas control" to open and adjust flow rate to 0.8 Nl/hour (0.8 units on scale). The pressure should still read 6 bar at both the "gas control" and regulator. At this point one should always check for leaks, this is easily done with soapy water and a syringe. There are two connections at the back of the gas control as well as the ones at the detector.

After any leaks have been fixed, the detector and gas lines need to be purged. To purge the system simply open the valve at the back of the gas control and leave it open for at least 3 minutes (I recommend 5 minutes). If an expensive gas is being used in place of p-10 it is possible to connect a ruffing pump to the exhaust at the back of the gas control and evacuate the system before opening the valve at the front of the gas control. If this method is used one evacuates the system then closes the valve at the back before opening the valve at the front. After the system has been back filled the valve at the fount is closed and the system is evacuated and back filled a second time before turning the high voltage on.

After closing the valve at the back the power can safely be turned on (x-rays must not be impinging on the detector). If the high voltage has not been previously adjusted start with it at zero and slowly increase it to 3.0kV. Now, with four

0.002in. Ni foils or equivalent attenuators in the beam, open the shutter. If rate meter does not show counts, raise high voltage (HV), but do not exceed 3.8kV. After impulses have been seen on the rate meter connect the PSM energy output to the ADC input. Now the energy peak can be displayed. You should be using 1024 channels and have the ADC gain at 1k. Adjust the HV so that the peak of the energy spectrum is at channel 300. I have also been told to set it at channel 600, however I believe this contributed to the dead spots on the wire. The energy peak is really set with an oscilloscope, however, Innovative Technology assumed that no one would have one so they gave the approximate energy that corresponded to the correct settings. It is a good idea to ask Innovative Technology for directions on how one would use an oscilloscope to adjust the HV.

Now connect the PSM's SCA output to ADC's gain input and switch ADC to coinc. Leaving the windows on the ADC open, lower upper level and raise the lower level of the PSM's windows till approximately 20% of the energy spectrum, without the escape peak, is left. The escape peak builds up below the main peak. In practice I try to keep as much of the peak as possible but make what is left after removing the escape peak symmetric. To display the position spectrum disconnect both BNC cables, switch ADC from coinc. to anti. and connect the PSM's position output to the ADC's input.

The wider the windows the better the counting rate but the linearity is affected. The ends of the wire will not count as much as the middle with wider windows. I suggest that if the peak is to be in the center of the detector to keep the count rate up and if linearity becomes a problem assume a quadratic background.

APPENDIX D SPECTROMETER ALIGNMENT

In order to align the scope on the Huber one must first put the tip of the "pin" at the center of rotation. Then it is a simple matter of adjusting the scope so that the cross-hairs are on the tip of the pin. To put the tip of the pin at the center of rotation when the scope is not properly adjusted, first adjust all the goniometer translations and rotations to zero. Next adjust the scope so that the pin is somewhere in view. Now, separately for both translations rotate Phi 180 degrees noting the position through the scope that the pin is rotating about. In other words, note the middle of the two extremes. Put the pin at this location and again rotate Phi as before and re-adjust the pin. Continue to rotate and re-adjust until the tip of the pin does not move. The height adjustment is easier but is done the same way only Chi is rotated instead of Phi.

Having put the pin at the center of rotation the scope can now be aligned. By tightening and loosening the bolts that hold the mount for the scope to the Chi circle you can adjust the scope up and down. After the height is correct loosen the bolts on the bottom of the scope's mount and adjust the scope right and left. Of course you may need to continue adjusting the scope by the above method until one adjustment does not affect the other.

It is important to first calculate the scattering angle for the monochromator and wavelength being used, and carefully mount the monochromator in its housing at the approximate position. The closer your first guess is, the less time it will take

to line up the monochromator. Because it is easiest to judge 0 or 90 degrees one should set the monochromator at zero and adjust the translations while looking down with a ruler across the top of the housing, then rotate the monochromator to the calculated angle. The Huber should also be moved to the calculated value of 2θ . To do this loosen the set screw on the under side of the monochromator housing, and make sure the beam path from the monochromator housing is connected to the Huber so that the angle of the Huber can be read as it is moved.

Now put the detector up close to the monochromator housing with the window horizontal in order to cover as large a solid angle as possible. Next, with all the slits open, recursively adjust $\theta_{\text{mon.}}$, the translations, and arcs of the monochromator until it is tweaked up. If you do this inside the x-ray shielding the x-ray power should be at a minimum. Moreover this operation is best done with two people, one to adjust the monochromator and one to watch the rate meter.

Now that the monochromator is lined up it is time to adjust the fine position of the Huber. The easiest way to determine the correct position is to put a fluorescent pad behind a pin that is at the center of rotation and with out foils and the lights out look at the florence relative to the pin. After a ruff adjustment using the air pads to move the Huber, a scope is mounted outside of the shielding with a view of the pin. The scope allows more precise estimates of the position of the beam relative to the pin. Shining a flashlight near the pin will allow one to see the pin while still seeing the x-ray fluorescence. After the Huber is in place an arm zero is done to position the detector arm, then slitting. If an analyzer is to be used slitting should be done with the analyzer in place.

To line up the analyzer one once again start by carefully estimating the correct zeros. It is best to put the detector up close to the analyzer with the window horizontal to again get the widest solid angle as possible, as seen from the

analyzer. With the detector at the approximate position, adjust the analyzer angle, then move the detector back and put its window vertical so that the detector angle can be set. Be careful to line up on k_1^a and not k_2^a . The only adjustment of the goniometer holding the analyzer that is important is the forward and back arc because this adjusts the height of the beam at the detector. The other adjustments should be left alone, the adjustments change 2θ , and it is better to simply readjust 2θ .

To put a sample at the center of rotation of the Huber first translate the scattering surface such that the part of the sample one wishes to scatter from is on the cross-hairs of the scope. Next while looking at the side of the sample through the scope adjust the relevant arc. The other arc can be adjusted as desired. The translation that moves the scattering face in a direction normal to the scattering surface can be adjusted in two ways. The first is to alternately look at the two sides of the sample and adjust its position until rotating from one side to the other rotates Φ 180 degrees. The second method which will work on irregular surfaces is to watch the face of the sample while rocking Φ back and forth and adjusting the translation till a spot on the sample stays at the cross-hairs. If the spot one finds is not the one desired adjust the other translation and then re-adjust the second. After one has gained some experience with this method it becomes easier. The direction of apparent movement relative to the cross-hairs is related to the direction the sample must be moved. However once the position is close, the change in magnitude of the apparent displacement can be used to zero in on the center of rotation. In practice the first method is usually a good start and the second method is a good check and or is used to fine tune the alignment.

APPENDIX E DETECTOR DEAD TIME CORRECTION

To correct for the non-linearity of the detector at high counting rates the detector dead time must be known. The detector dead time correction is then⁽¹⁰⁰⁾,

$$n_{\text{true}} = n_{\text{observed}} / (1 - \tau_{\text{eff}} n_{\text{observed}}) \quad (\text{E.1})$$

where n_{true} is the corrected value of n_{observed} and τ_{eff} is the effective detector dead time. The detector dead time can be measured with an oscilloscope or by a multiple-foil method. In the multiple-foil method n_{true} is estimated from the attenuation factor of a foil placed in the beam path multiplied by the number of attenuated counts. τ_{eff} is then calculated from n_{true} and n_{observed} by equation E.1. Here a similar method was used only the power of the x-ray source was lowered instead of placing a foil in the beam. The value of n_{true} was estimated from the count rate at low power, n_{low} , the monitor counts at low power, m_{low} , and the monitor counts at high power, m_{observed} .

$$n_{\text{true}} = n_{\text{low}} \cdot (m_{\text{observed}} / m_{\text{low}}) \quad (\text{E.2})$$

The effective dead time was then calculated by the relation described in equation E.1 and found to be 5.562×10^{-6} sec/count.

REFERENCES

- ¹J.D. Gunton, M. San Miguel, and P.S. Sahni in Phase Transitions and Critical Phenomena, ed. C. Domb and J.L. Lebowitz (Academic, London, 1983) Vol. 8.
- ²J.D. Gunton, in Magnetic Phase Transitions, ed. M. Ausloos and R.J. Elliott (Springer, Berlin, 1983).
- ³K. Kawasaki, in Phase Transitions and Critical Phenomena, ed. C. Domb and M.S. Green (Academic Press, New York, 1972), Vol. 2.
- ⁴J.W. Christian, in The Theory of Transformations in Metals and Alloys, Part 1, ed. D.W. Hopkins, (Pergamon Press, New York, 1975).
- ⁵M.F. Colluis, in Magnetic Critical Scattering, ed. S.W. Lovesey and E.W.J. Mitchell, (Oxford University Press, New York, 1989).
- ⁶H.E. Stanley, in Introduction to Phase Transitions and Critical Phenomena, ed. W. Marshall and D.H. Wilkinson, (Oxford University Press, New York, 1971).
- ⁷T. Hashimoto, K. Nishimura, and Y. Takeuchi, J. Phys. Soc. Jpn. **45**, 1127 (1978).
- ⁸K.F. Ludwig, Jr., G.B. Stephenson, J.L. Jordan-Sweet, J. Mainville, Y.S. Yang, and M. Sutton, Phys. Rev. Lett. **61**, 1859 (1988).
- ⁹N. Kurnakow, S. Zemczuzny and Zasedatalev, J. Inst. Metals **15**, 305 (1916).
- ¹⁰F.C. Nix and W. Shockely, Rev. Mod. Phys. **10**, 1 (1938).
- ¹¹C. Sykes and H. Evans, J. Inst. Metals **58**, 255 (1936).
- ¹²C. Sykes and F.W. Jones, Proc. Roy. Soc. London **157A**, 213 (1936).
- ¹³F.W. Jones and C. Sykes, Proc. Roy. Soc. London, **166A**, 376 (1938).
- ¹⁴W.L. Bragg and E.J. Williams, Proc. Roy. Soc. London, **145A**, 699 (1934).

- ¹⁵W.L. Bragg and E.J. Williams, Proc. Roy. Soc. London, **151A**, 540 (1935).
- ¹⁶E.J. Williams, Proc. Roy. Soc. London, **152A**, 231 (1935).
- ¹⁷H.A. Bethe, Proc. Roy. Soc. London, **150A**, 552 (1935).
- ¹⁸R. Peierls, Proc. Roy. Soc. London, **154A**, 207 (1936).
- ¹⁹G. Vineyard, Phys. Rev. **102**, 981 (1956).
- ²⁰S.M. Allen and J.W. Cahn, Acta. Meta. **27**, 1085 (1979).
- ²¹R. Kikuchi and J.W. Cahn, Acta. Meta. **27**, 1337 (1979).
- ²²I.M. Lifshitz, JETP **15**, 939 (1962).
- ²³J.D. Gunton, J. Stat. Phys. **34**, 1019 (1984).
- ²⁴G.F. Mazenko, Phys. Rev. B**26**, 5103 (1983).
- ²⁵G.F. Mazenko and O.T. Valls, Phys. Rev. B**27**, 6811 (1983).
- ²⁶G.F. Mazenko and O.T. Valls, Phys. Rev. Lett. **51**, 2044 (1983).
- ²⁷G.F. Mazenko and O.T. Valls, Phys. Rev. B**30**, 6732 (1984).
- ²⁸F.C. Zhang, O.T. Valls, G.F. Mazenko, Phys. Rev. B**31**, 1579 (1985).
- ²⁹G.F. Mazenko and O.T. Valls, F.C. Zhang, Phys. Rev. B**31**, 4453 (1985).
- ³⁰Z.W. Zai, O.T. Valls, G.F. Mazenko, Phys. Rev. B**37**, 9481 (1988).
- ³¹I.M. Lifshitz and V.V. Slyozov, J. Phys. Chem. Solids **19**, 35 (1961).
- ³²J.W. Cahn and J.E. Hilliard, J. Chem. Phys. **28**, 258 (1958).
- ³³J.S. Langer, M. Bar-On, and H.D. Miller, Phys. Rev. A**11**, 1417 (1975).
- ³⁴K. Kawasaki, M. Yalabik and J.D. Gunton, Phys. Rev. A**17**, 445 (1978).
- ³⁵T. Ohta, D. Jasnow and K. Kawasaki, Phys. Rev. Lett. **49**, 1223 (1982).

- ³⁶M. Grant And J.D. Gunton, *Phy. Rev. B* **29**, 1521 (1984).
- ³⁷G.T. Gawlinski, M. Grant, J.D. Gunton, K. Kaski, *Phys. Rev. B* **31**, 281 (1985).
- ³⁸A. Milchev, K. Binder, and D.W. Heerman, *Z. Phys. B* **63**, 521 (1986).
- ³⁹G. Mazenko, O.T. Valls, and M. Zannetti, *B* **40**, 379 (1989).
- ⁴⁰H.L. Snyder and P. Meakin, *J. Chem. Phys.* **79**, 5588 (1983).
- ⁴¹T. Hashimoto, K. Nishimura, and Y. Takeuchi, *Phys. Lett* **65A**, 250 (1978).
- ⁴²S. Nishihara, Y. Noda and Y. Yamada, *Sol. Stat. Comm.* **44**, 1487 (1982).
- ⁴³Y. Noda, S. Nishihara, and Y. Yamada, *J. Phys. Soc. Jpn.* **53**, 4241 (1983).
- ⁴⁴Y. Yamada, N. Hayama, J.D. Axe and S.M. Shapiro, *Phys. Rev. Lett.* **27**, 1655 (1984).
- ⁴⁵O. Blaschko, P. Fratzl, G. Grest, M. Bernole, and G. Fuyara, *Phys. Rev. B* **30**, 6498 (1984).
- ⁴⁶F. Furusaka, Y. Ishikawa, M. Mera, *Phys. Rev. Lett.* **54**, 2611 (1985).
- ⁴⁷M. Hennion, D. Ronzaud, and P. Guyot, *Acta Met.* **30**, 599 (1982).
- ⁴⁸P.K. Wu, J.H. Perepezko, J.T. McKinney, and M.G. Lagally, *Phys. Rev. Lett.* **51**, 1577 (1983).
- ⁴⁹G.C. Wang and T.M. Lu, *Phys. Rev.* **50**, 2014 (1983).
- ⁵⁰S. Katano and M. Iizumi, *Phys. Rev. Lett.* **52**, 835 (1984).
- ⁵¹H. Homma and R. Clarke, *Phys. Rev. Lett.* **52**, 629 (1984).
- ⁵²M. Furusaka, Y. Ishikawa, S. Yamaguchi and Y. Fusino, *Physica* **120C**, 383 (1983).
- ⁵³G. Kostnz, *Physica* **120C**, 387 (1983).
- ⁵⁴S. Katano and M. Iizumi, *Physica* **120C**, 392 (1983).
- ⁵⁵S. Komura, K. Osamura, H. Gujii, and T. Takeda, *Physica* **120C**, 397 (1983).

- ⁵⁶R. Clarke, Bull. Am. Phys. Soc. **30**, 346 (1985).
- ⁵⁷D.B. McWhan, G. Aeppli, J.P. Remeika and S. Nelson, J. Phys. C**18**, 2307 (1985).
- ⁵⁸A. Bortz, M.H. Kalos, J.L. Lebowitz and M.A. Zengdegas, Phys. Rev. **B10**, 535 (1974).
- ⁵⁹J. Marro, A. Bortz, M.H. Kalos, and J.L. Lebowitz, Phys. Rev. **B12**, 2000 (1975).
- ⁶⁰A. Sur, J.L. Lebowitz, J. Marro, and M.H. Kalos, Phys. Rev. **B15**, 3014 (1977).
- ⁶¹J. Marro, J.L. Lebowitz, M.H. Kalos, Phys. Rev. Lett. **43**, 282 (1979).
- ⁶²M.K. Phani, J.L. Lebowitz, M.H. Kalos, Phys. Rev. Lett. **43**, 368 (1980).
- ⁶³P.S. Sahni, J.D. Gunton, Phys. Rev. Lett. **45**, 368 (1980).
- ⁶⁴P.S. Sahni, G. Dee, J.D. Gunton, M.K. Phani, J.L. Lebowitz, and M.H. Kalos, Phys. Rev. **B24**, 410 (1981).
- ⁶⁵J.L. Lebowitz, J. Marro, and M.H. Kalos, Acta Met. **30**, 297 (1982).
- ⁶⁶P.S. Sahni, G.S. Grest, and S.A. Safran, Phys. Rev. Lett. **50**, 60 (1983).
- ⁶⁷A. Sadiq and K. Binder, Phys. Rev. Lett. **51**, 674 (1983).
- ⁶⁸K. Kaski, M.C. Yalabik, D.J. Gunton, and P.S. Sahni, Phys. Rev. **B28**, 5263 (1983).
- ⁶⁹G.S. Grest, D.S. Srolovitz, and M.P. Anderson, Phys. Rev. Lett. **51**, 634 (1983).
- ⁷⁰A. Sadiq and K. Binder, J. Stat. Phys. **35**, 517 (1984).
- ⁷¹G.S. Grest and P.S. Sahni, Phys. Rev. **B30**, 226 (1984).
- ⁷²G.S. Grest, and D.S. Srolovitz, Phys. Rev. **B30**, 5150 (1984).
- ⁷³P.S. Sahni, G.S. Grest, M.P. Anderson, and D.S. Srolovitz, Phys. Rev. Lett. **50**, 263 (1983).
- ⁷⁴S.A. Safran, P.S. Sahni, and G.S. Grest, Phys. Rev. **B26**, 466 (1982).

- ⁷⁵G.S. Grest, S.A. Safran, And P.S. Sahni, J. Mag. Mug. Mat. **31–34**, 1011 (1983).
- ⁷⁶S.A. Safran, P.S. Sahni, and G.S. Grest, Phys. Rev. **B28**, 2693 (1983).
- ⁷⁷P.S. Sahni, D.S. Srolovitz, and G.S. Grest, M.P. Anderson, and S. a. Safran, Phys. Rev. **B28**, 2705 (1983).
- ⁷⁸K. Huang, Statistical Mechanics, (J. Wiley, New York, 1963).
- ⁷⁹R.S. Glauber, J. Math. Phys. **4**, 294 (1963).
- ⁸⁰D.A. Huse and C.L. Heniey, Phys. Rev.Lett. **54**, 2708 (1985).
- ⁸¹G.S. Grest and D.J. Srolovitz, Phys. Rev. **B32**, 3014 (1985).
- ⁸²D.J. Srolovitz and G.S. Grest, Phys. Rev. **B32**, 3021 (1985).
- ⁸³D. Chowdhury, M. Grant, and J.D. Gunton, Phys. Rev. **B35**, 6792 (1987).
- ⁸⁴D.J. Srolovitz and G.N. Hassold, Phys. Rev. **B35**, 6902 (1987).
- ⁸⁵D.G. Morris, Phys. Status Solidi (a) **82**, 145 (1975).
- ⁸⁶K.N. Tu, J. Appl. Phys. **48**, 3400 (1979).
- ⁸⁷G.S. Grest and D.S. Srolovitz, Phys. Rev. **B30**, 6535 (1984).
- ⁸⁸K. Kaski and J.D. Gunton, Phys. Rev. **B28**, 5731 (1983).
- ⁸⁹K. Binder, in Statistical Physics, ed. H.E. Stanley (North–Holland, New York, 1986).
- ⁹⁰B. Warren, X–Ray Diffraction, (Addison–Wesley, Reading, MA, 1969).
- ⁹¹S.C. Moss, in Local Atomic Arrangements Studied by X–Ray Diffraction, ed. J.B. Cohen and S.E. Hilliard (Gordon and Breach, New York, 1966), p. 95.
- ⁹²Z.W. Lai, Phys. Rev **B13**, 9239 (1990).
- ⁹³N Wakabayashi, Phys. Rev. **B33**, 6441 (1986).

- ⁹⁴H. Chen and J.B. Cohen, J. Phys. (Paris) C7, 314 (1977).
- ⁹⁵F.P. Burns and S.L. Quimby, Phys. Rev. 97, 1567 (1955).
- ⁹⁶P. Debye, H.R. Anderson, Jr., and H. Brumberger, J. Appl. Phys. 28,679 (1957).
- ⁹⁷T. Castan, P. A. Lindgard, Phy. Rev. B41, 2534 (1990).
- ⁹⁸C. Kittel in Introduction to Solid State Physics, sixth edition, (John Wiley and Sons, Inc. New York 1986).
- ⁹⁹L. Van Hove, Phys. Rev. 95, 249 (1954)
- ¹⁰⁰International Tables For X-ray Crystallography, ed. C. H. Macgillavry, G. D. Rieck, and K. Lonsdale. (D. Reidel Publishing Co. Dordrecht, Holland 1983) Vol III.
- ¹⁰¹P. Kumar private communications.
- ¹⁰²R. A. Cowley, Acta Cryst. A43, 825 (1987).
- ¹⁰³C. A. Lucas, E. Gartstein, R. A. Cowley, Acta Cryst. A45, 416 (1989).
- ¹⁰⁴S.E. Nagler, R.F. Shannon, Jr., C.R. Harkless, M.A. Singh, and R.M. Nicklow, Phys. Rev. Lett. 61, 718 (1988).
- ¹⁰⁵S. Hendrichs and E. Teller, J. Chem. Phys. 10, 147 (1942).
- ¹⁰⁶H. Konishi and Y. Noda, in "Dynamics of Ordering Processes," edited by S. Komura (Plenum, New York, 1988)
- ¹⁰⁷N. Wakabayashi, private communications.
- ¹⁰⁸R.F. Shannon, Jr., C.R. Harkless, and S.E. Nagler, Phys. Rev. B38, 9327 (1988).
- ¹⁰⁹P. J. Shah O. G. Mouritsen, Phys. Rev. B10, 7003 (1990).
- ¹¹⁰X-M. Zhu, H. Zabel, I. K. Robinson, E. Vlieg, J. A. Dura, and C. P. Flynn, Bull. Am. Phys. Soc. 35, 369 (1990).
- ¹¹¹K. Okamura, H. Iwasaki, and S. Ogawa, J. Phy. Soc. Japan 24,569 (1968).
- ¹¹²H. dosch, L. Mailander, A. Lied, and J. Peisl, Phys. Rev. Lett. 60, 2382 (1988).

¹¹³X—M. Zhu, R. Feidenhans'l, H. Zabel, J. Als—Nielsen, R. Du, C. P. Flynn, and F. Grey, *Phys. Rev.* **B37**, 7157 (1988).

¹¹⁴P. H. Okuzumi, P. Perio, and M. Tournarie, *Acta Cryst.* **12**, 1039 (1959).

¹¹⁵P. Perio, and M. Tournarie, *Acta Cryst.* **12**, 1032 (1959).

¹¹⁶M. J. Marcinkowski and L. Zwell, *Acta Metall.* **11**, 373 (1963).

BIOGRAPHICAL SKETCH

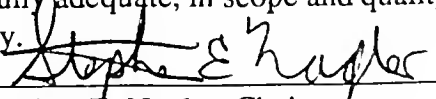
I was born on April 17, 1961. By the age of five I had lived in three states and had just moved to Tampa, Florida, where I grew up. I have always enjoyed sports and the outdoors and spent much of my adolescence horseback riding in the boondocks of Tampa. However, I must admit that it is my sister who is the expert rider and it was her encouragement that got me started on horse back riding. I also have an interest in building and fixing almost anything. Many times when something broke my brother and/or I would take it apart and put it back together, most of the time not finding anything wrong with it, but it usually would work again anyway. My tinkering has not only been useful in that many things were repaired or constructed, but also in some ways it prepared me for installing/constructing the x-ray scattering lab that I used to collect the data reported here.

My parents, both being teachers, always stressed schooling and had a large influence in my decision to go to graduate school. But, more importantly, somehow through their encouragement and support I never gave up on learning despite the fact that all through grade school (private, which probably helped a lot) I had difficulty in everything but math and science. I entered Tampa Preparatory High School with a spelling level of a third grader and to this day I read relatively slowly. It was halfway through my freshman year of high school that I was diagnosed as dyslexic. That summer I went to St George's in Rhode Island where I improved among other things my spelling (up to a seventh grade level, 4 years in one

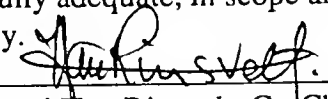
summer). After high school I went to The College of the Holy Cross where any Irish Catholic would fit right in. In college I received a solid liberal arts education. The smallness of the school was important in that allowances were sometimes made for my particular problems and my professors were very accessible. Here at the University of Florida some allowances have been made as well, the typical allowance is extra time on exams, which is what is allowed on most standardized tests such as the GRE.

As a graduate student I have given three APS March Meeting presentations, and two undergraduate level talks, one at The College of the Holy Cross and the second at Stockton State College. My work has produced three publications to date. It is hoped that several more will soon be finished, including a more detailed look at the early time and the M.B.E. data.

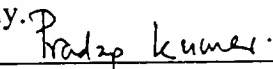
I certify that I have read this study and that in my opinion it conforms to acceptable standards of scholarly presentation and is fully adequate, in scope and quality, as a dissertation for the degree of Doctor of Philosophy.


Stephen E. Nagler, Chairman
Associate Professor of Physics


I certify that I have read this study and that in my opinion it conforms to acceptable standards of scholarly presentation and is fully adequate, in scope and quality, as a dissertation for the degree of Doctor of Philosophy.


Henri Van Rinsvelt, Co-Chairman
Professor of Physics

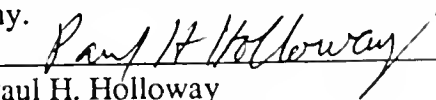
I certify that I have read this study and that in my opinion it conforms to acceptable standards of scholarly presentation and is fully adequate, in scope and quality, as a dissertation for the degree of Doctor of Philosophy.


Pradeep Kumar
Associate Professor of Physics

I certify that I have read this study and that in my opinion it conforms to acceptable standards of scholarly presentation and is fully adequate, in scope and quality, as a dissertation for the degree of Doctor of Philosophy.



Neil S. Sullivan
Professor of Physics

I certify that I have read this study and that in my opinion it conforms to acceptable standards of scholarly presentation and is fully adequate, in scope and quality, as a dissertation for the degree of Doctor of Philosophy.


Paul H. Holloway
Professor of Materials Science
and Engineering

This dissertation was submitted to the Graduate Faculty of the Department of Physics in the College of Liberal Arts and Sciences and to the Graduate School and was accepted as partial fulfillment of the requirements for the degree of Doctor of Philosophy.

August, 1990


Dean, Graduate School

UNIVERSITY OF FLORIDA



3 1262 08553 8436